The Thesis Committee for Gary F. Simpson Jr.

Certifies that this is the approved version of the following thesis:

A Combined Experimental and Modeling Study of Low Velocity Perforation of Thin Aluminum Plates

APPROVED BY

SUPERVISING COMMITTEE:

Supervisor:

K. Ravi-Chandar

Chad Landis

A Combined Experimental and Modeling Study of Low Velocity Perforation of Thin Aluminum Plates

By

Gary F. Simpson Jr., B.S.M.E, B.S.Phy.

Thesis

Presented to the Faculty of the Graduate School of

The University of Texas at Austin

in Partial Fulfillment

of the Requirements

for the Degree of

Master of Science in Engineering

The University of Texas at Austin

December 2015

Abstract

A Combined Experimental and Modeling Study of Low Velocity Perforation of Thin Aluminum Plates

Gary F. Simpson Jr., M. S. E

The University of Texas at Austin, 2015

Supervisor: K. Ravi-Chandar

This work conducts a combined experimental and modeling study of low velocity projectile perforation of thin AA5083-H116 aluminum plates. Experiments were performed in order to characterize the candidate material and calibrate simple and easy to implement empirical models for both the material response and ductile failure behavior. Quasi-static tensile tests were performed in order to investigate the Portevin-Le Chatelier effect common to 5xxx series aluminum as well as to calibrate a Ramberg-Osgood representation for the material stress-strain curve. The material response at strain rates up to and exceeding 10^4 s^{-1} was investigated by means of an electromagnetically driven ring expansion test, characterizing the potential strain rate sensitivity of the material. Additionally, the failure behavior and potential damage accumulation of the material were evaluated using an interrupted, multiple loading path strain-to-failure test, validating a Johnson-Cook failure model for use in numerical simulation. Low velocity ballistic impact and perforation experiments, investigating several specific mechanisms of deformation and failure, were conducted and modeled by implementing the developed material and failure model in 3D finite element simulations.

Table of Contents

Chapter 1. Material Properties and Quasi-static Calibration……...1

1.1 Quasi-static Uniaxial Material Response……..3

1.2 Material Calibration and Constitutive Model……...9

Chapter 2. Expanding Ring Experiments and Evaluation of Material Strain Rate Dependence……..13

2.1 Experimental Setup and Procedure…….16

2.2 Experimental Results……...21

2.3 Simulation Results and Analysis…….34

Chapter 3. Interrupted Strain-to-Failure Experiments and Material Failure Model Validation…….46

3.1 Experimental Setup and Procedure……50

3.2 Experimental Results……...53

3.3 Simulation Results and Analysis……63

Chapter 4. Ballistic Impact and Perforation of Thin Plates……...76

4.1 Experimental Setup and Procedure…….….83

4.2 Experimental Results……...86

4.3 Simulation Results and Analysis……...……104

Chapter 5. Conclusions and Recommendations……..……..129

Bibliography……...132

Chapter 1: Material Properties and Quasi-static Calibration

The material selected for this study is AA5083 aluminum, a non-heat-treatable Al-3Mg alloy. This alloy contains 4-4.9% Mg as the primary alloying element (ASTM B928, ASTM B209). The specific test material was a rolled sheet of the H116 strain-hardened temper, conforming to ASTM B928 for marine grade aluminum plate. This material was chosen, in the spirit of this study, because 5083 aluminum was one of the first aluminum alloys to see common use as lightweight structural armor in vehicles on both land and sea.

While a rather venerable alloy by modern standards, 5083 is known for its exceptional corrosion resistance and performance at low temperatures, as well as its high weldability and superior strength to contemporary aluminum alloys and non-heat-treatable aluminum alloys in general.

Its notable performance in marine environments as well as its relatively low cost and high availability, has led to its acceptance as the material of choice for the construction of lightweight, high utility marine vessels. Its good weldability (and as-welded strength) has also made 5083 a desirable material for the construction of larger vessels, and the U.S. Navy has adopted 5xxx series alloys for several vessels such as variants of the Littoral Combat Ship (LCS) and Joint High Speed Vehicle (JHSV), a military adaptation of the all-aluminum high speed jet ferries in use around the world (Alcoa Defense, 2010).

Although primarily utilized in marine applications today, 5083 was very quickly adopted for use as lightweight vehicle armor. The M113 armored personnel carrier, the predecessor to the Bradley fighting vehicle, made almost total structural use of 5083 for its lightweight and high strength. While modern alloys and armor structures have replaced 5083 in the role ballistic protection on the front lines, M113 variants are still employed today in support roles (Global Security, 2012).

The historical and continued use of 5083 in armor and military applications makes it a good candidate material for the study of ductile failure in aluminum alloys and metallic plates under dynamic loading and ballistic impact. This work seeks to evaluate the material response of AA5083, ultimately attempting to calibrate and implement a relatively simple mechanical material model—including plasticity and ductile failure—for use in simulation of ballistic impact, penetration and perforation. This effort is intended to evaluate the potential of conventional, easy-to-calibrate material models to accurately capture the complex behavior of projectile impact beyond the ballistic limit of a target or simple armor system, when implemented in a realistic model geometry. This thesis is organized into four chapters. Chapters 1 through 3 each discuss a different aspect of the integrated material modeling and experimental program undertaken for this project. Chapter 4 describes the final experimental and modeling effort, combining the previous results into a useful framework for the simulation of ballistic penetration and perforation under the conditions tested.

1.1 Quasi-static Uniaxial Material Response

The quasi-static stress strain behavior of the material was obtained by performing a pair of uniaxial tension tests. Rectangular cross-section tensile dogbone specimens, shown in Fig. 1.1, were cut via electrical discharge machining (EDM) from a 1.6 mm thick sheet of 5083-H116 aluminum. The first specimen was loaded under a displacement control at a constant strain rate of approximately $3x10^{-4}$ s^{-1} using an Instron electromechanical load frame, and is utilized to calibrate the uniaxial stress-strain response of the material. The second specimen was specifically used to observe the full-field strain pattern to failure and was loaded at variable displacement rate to facilitate efficient high resolution image capture.

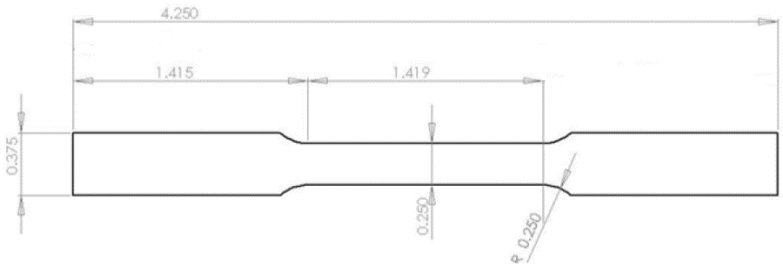

Figure 1.1: Quasi-static Tension Specimen Geometry (Inches)

Strain data was collected via digital image correlation (DIC). Acquired test images were analyzed using ARAMIS™ DIC software to obtain strain data as a function of time.

Using the acquired load and strain data, the stress-strain behavior shown in Fig. 1.2 was generated prior to the onset of necking.

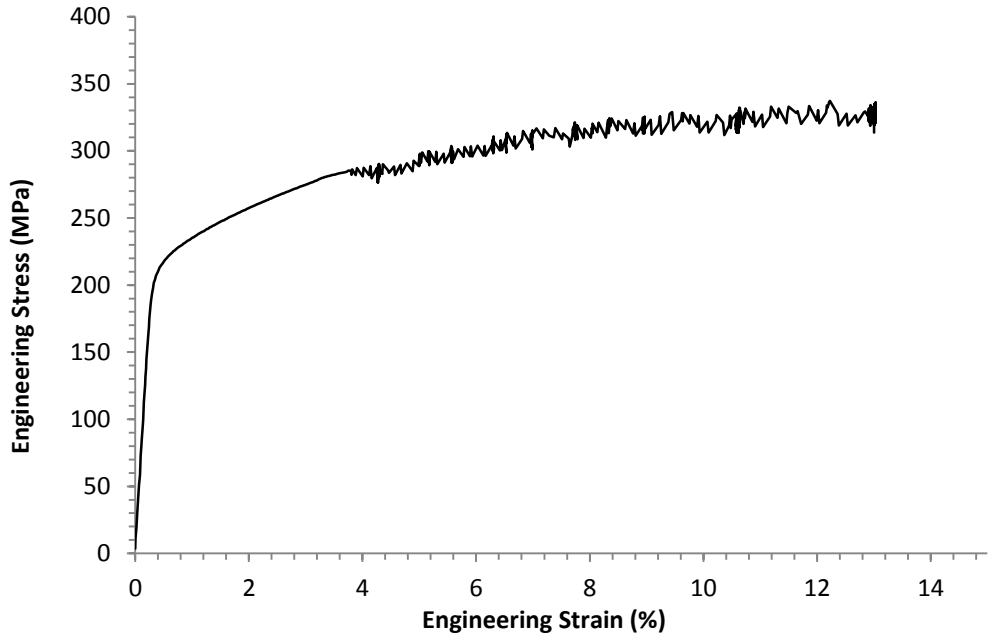

Figure 1.2: Quasi-static Tensile Experimental Stress-Strain Curve

The uniaxial engineering stress-strain response shows significant strain hardening for a relatively strong aluminum alloy. The onset of diffuse necking begins at approximately 12% strain, and the maximum or ultimate stress, at this strain value, is approximately 325 MPa. As commonly seen in Al-3Mg alloys, the material shows a serrated stress response, associated with the Portevin-Le Chatelier (PLC) effect, for much of the hardening region. The PLC effect begins at a critical strain of 3.6% on the stress-strain curve, and examination of ARAMIS images shows the development of type C PLC bands at this strain level. In contrast to the propagating type A and B bands—which

appear to travel the length of the specimen—commonly seen in other alloys, type C PLC bands result in stationary bands of accumulating local strain that do not fully propagate longitudinally throughout the specimen, but nucleate at multiple discrete locations on the sample (Cassarotto, 2009).

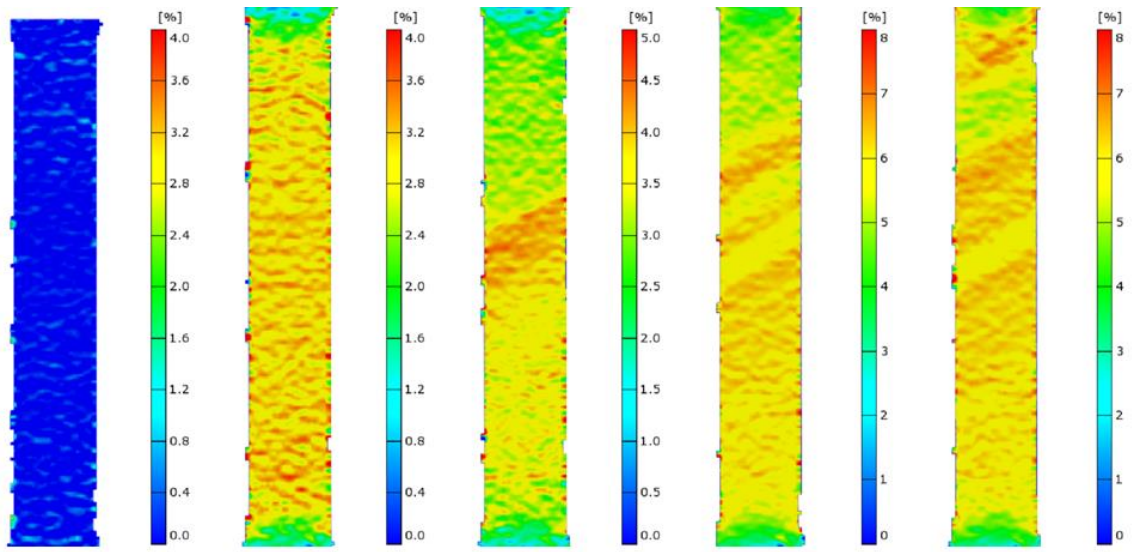

~0 % 3.1 % 3.5% 5.9% 6.0%

Figure 1.3: Initial PLC Band Formation

Figure 1.3 shows the development of the initial band structure nucleated at a critical strain of ~3.5%. Note, Figures 1.3, 1.4 and 1.6 are labeled by average strain in the specimen, reflecting the cumulative effective strain across the non-uniform axial distribution. As average straining of the specimen continues, new bands activate along the length of the specimen contributing to the global average strain response and bringing the rest of the material "up" to the current strain level (see Fig. 1.4). While initial bands develop parallel to one another, intersecting bands develop at a strain level of 9-10%.

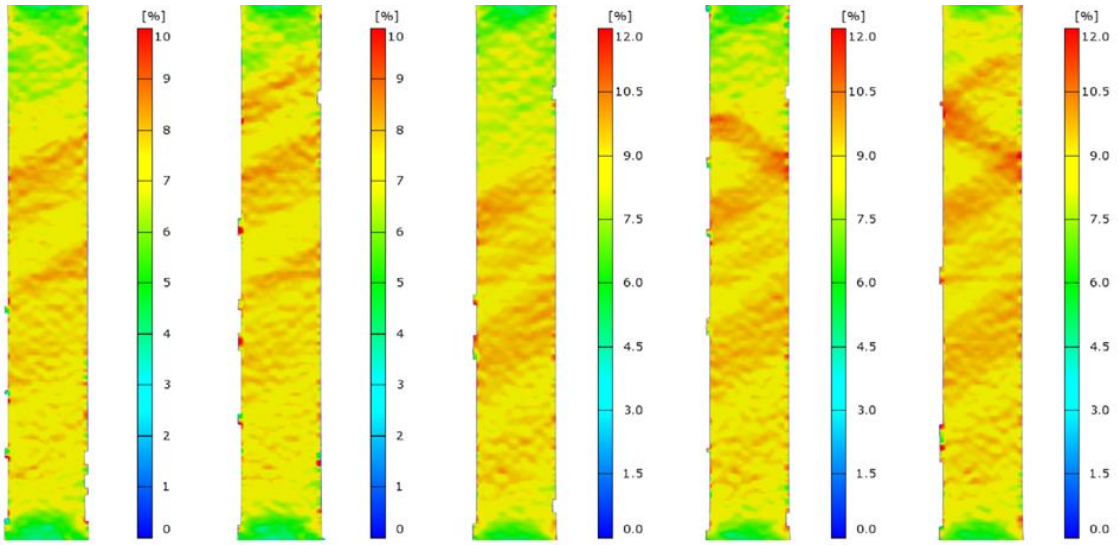

7.4 % 7.5 % 8.9 % 9.1% 9.3%

Figure 1.4: Band Development During Hardening

Depending upon the development of the band structure in the material, two individual points may experience strains differing by a couple of percent. The actively straining portions of the sample may vary, alternate and change based upon the nucleation and the growth of bands until the full onset of necking and instability. While the minor strain variations within the structure do not significantly affect the global material response and the stability strain limit, the pattern of band development and activation around the necking strain may influence the location of the neck and determine which material point sees the ultimate development of a neck exhibiting both diffuse and sheet mode character. Several locations on the specimen actually experience significant strain prior to necking, possessing a much higher strain level at the onset of instability

than the location at which the neck actually develops. Figure 1.5 shows the axial variation in strain at a number of increasing average strain levels.

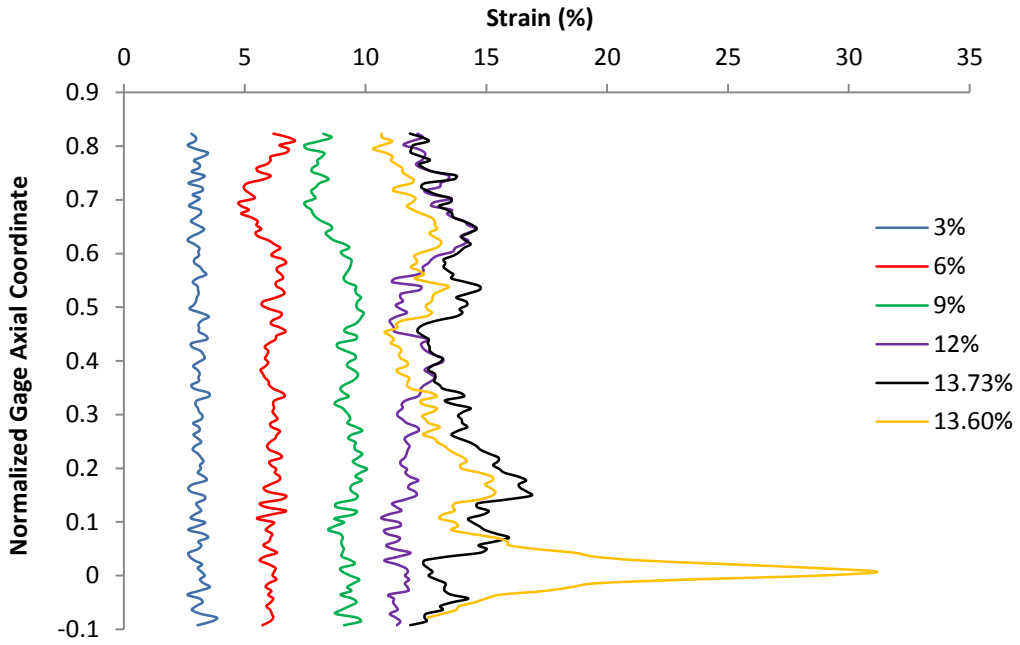

Figure 1.5: Axial Strain Profile at Multiple Average Strain Levels

The location of the neck ($y = 0$) is at a minimum strain level seen in the gage section prior to activation. As instability is reached, this actively straining location continues to strain locally, developing the neck. Note that no additional strain is accumulated outside of the neck region post-instability.

Under these quasi-static uniaxial conditions, the necking or specimen Considère strain is approximately 12%. The development of the specimen neck prior to failure is shown in Fig. 1.6 (the location of the fracture is marked for reference).

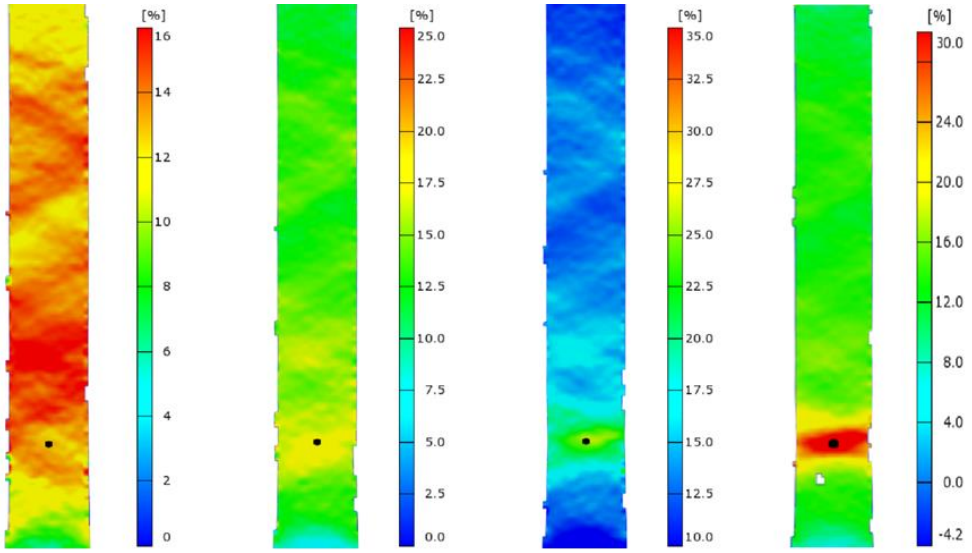

Figure 1.6: Specimen Necking Prior to Failure

While diffuse necking character is visible, the necking process is dominated by the through-the-thickness sheet mode, resulting in a slant fracture through the thickness of the specimen (see Fig. 1.7). The axial failure strain at the surface corresponding to the last image recorded was ~35%.

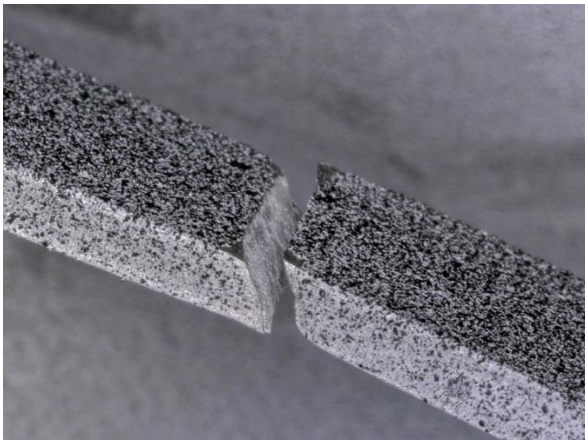

Figure 1.7: Tension Specimen Fracture

1.2 Material Calibration and Constitutive Model

To characterize the material stress-strain response, a Ramberg-Osgood representation was fit to the uniaxial stress-strain response up to the onset of necking. A Ramberg-Osgood (R-O) fit, represents the addition of linear and power-law strain over the entire material response:

$$\varepsilon = \frac{\sigma}{E} + \alpha\frac{\sigma}{E}\left(\frac{\sigma}{\sigma_0}\right)^{n-1} \tag{1.1}$$

This equation, a function of stress, requires only four constants: the elastic modulus E, the yield stress σ_0, the hardening exponent n, and a scalar α such that $(1+\alpha)\frac{\sigma_0}{E}$ is the total strain at yield. This representation gives dominant elastic behavior at low strains and

dominant plastic or hardening behavior at higher strains post-yielding. This behavior allows the R-O fit to closely represent many common metallic stress-strain curves using only four fitting parameters without the need for piecewise or discontinuous functions.

Applied to the true stress curve vs logarithmic strain of the test material, the R-O fit closely approximates the average hardening behavior of the material (see Fig. 1.8).

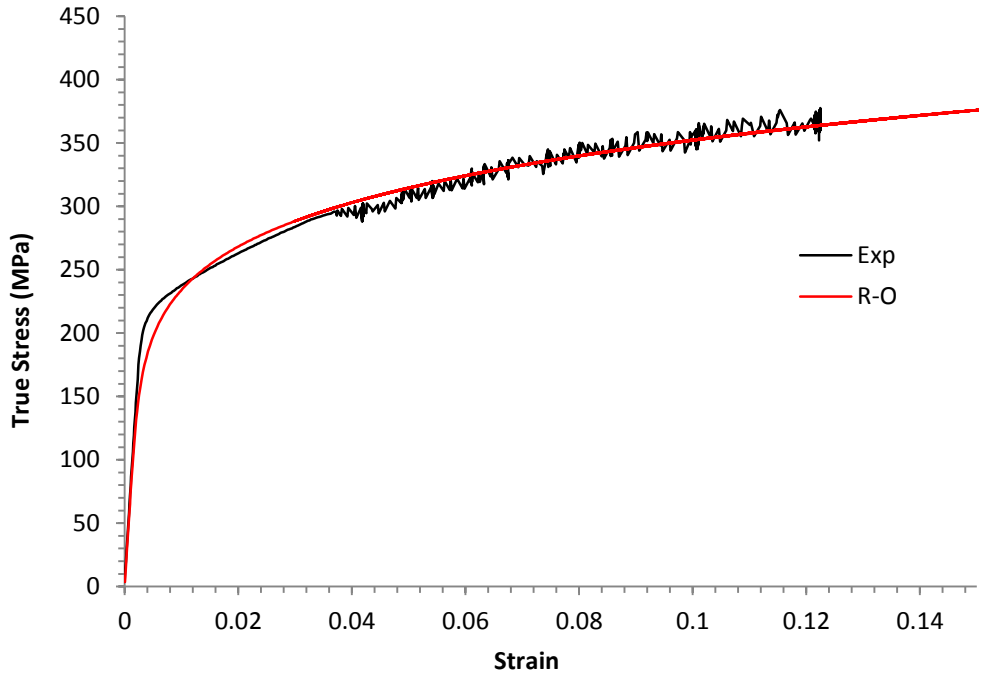

Figure 1.8: Ramberg-Osgood Model and Experimental True Stress-Strain Curve

While R-O clearly cannot represent the serrated region of the curve (due to PLC effect) the overall hardening behavior of the material is sufficient to capture the plastic properties of the material necessary to utilize continuum plasticity modeling methods. In addition, the R-O fit fails to capture the behavior of the material near yielding. The true

material response shows a much sharper transition from elastic to hardening behavior which cannot be captured by the continuous linear/power-law shape of the R-O representation. However, the accuracy of Ramberg-Osgood for hardening materials at high plastic strains makes it an attractively simple material representation for the analysis of high deformation events and structural behavior assuming sufficient real hardening exists in the material in question. The R-O representation of the candidate material (given in Fig. 1.8) will be extrapolated to significantly higher levels of plastic strain (than seen under uniaxial test conditions) for use in numerical models developed in subsequent chapters.

Under quasi-static loading, the R-O material representation is capable of capturing the general plastic behavior of most metals; however, dynamic loading posits a set of potential complications in a material model. Under dynamic loading at elevated strain rates, the potential for strain rate dependence and non-equilibrium heating of the material under deformation may require a material response of significantly increased complexity in order to sufficiently capture structural behavior. A commonly implemented empirical plasticity model for use under dynamic conditions is the Johnson-Cook (1983) plasticity model:

$$\bar{\sigma} = [A + B(\bar{\varepsilon}^p)^k]\left[1 + C\ln\left(\frac{\dot{\bar{\varepsilon}}^p}{\dot{\varepsilon}^0}\right)\right]\left(1 - \hat{T}^m\right) \qquad \text{where, } \hat{T} = \frac{T - T_0}{T_m - T_0} \qquad (1.2)$$

Johnson-Cook plasticity allows for the effect of strain rate and thermal softening, both of which may be necessary under high speed deformation events experiencing near-adiabatic heating.

However, if under appropriate conditions, a material can be shown to experience negligible strain rate dependence or thermal softening then the Johnson-Cook plasticity model reduces to standard J_2 plasticity with isotropic hardening of equivalent form to the R-O material representation. The following chapter evaluates the strain rate dependence of 5083 aluminum and makes an argument for the use of standard, strain-rate independent J_2 plasticity with isotropic hardening in the modeling of low-speed ballistic impact.

Chapter 2: Expanding Ring Experiments and Evaluation of Material Strain Rate Dependence

The testing and characterization of materials at high strain rates has been and continues to be a challenging area of study. The difficulties in attaining accurate quantitative data at high strain rates have left a rather sparse body of knowledge regarding material behavior in these regimes. The Hopkinsons began investigation into material behavior at high strain rates in late 19^{th} and early 20^{th} century by performing impact experiments on long wires and rods, evaluating the stress waves generated by the high speed loading (Hopkinson, 1914). By the middle of the 20^{th} century, Kolsky (1949) had introduced his modified split Hopkinson bar, now considered a standard method for the dynamic evaluation of materials in torsion, tension and compression. However, the use of a Kolsky bar may place inconvenient limitations on an experiment such as specimen geometry and fabrication, or practicality of loading mechanism.

To impose high strain rate loading to significant plastic strains or failure, a more useful and versatile mechanism may be that of an electromagnetically driven expanding ring test. Niordson (1965) first utilized this loading mechanism in the mid 1960's to demonstrate the capability of an electromagnetic coil to drive radial expansion of a conductive sample at strain rates of $10^4\ s^{-1}$. While only qualitative and demonstrative, Niordson did succeed in capturing an image of the ring showing seemingly simultaneous arc discharges at fracture points on the ring. Nearly twenty years later, Grady and Benson (1983) performed the first systematic experimental analysis of an expanding ring test at a

variety of strain rates, capturing the expansion and fracture of the ring using a streak camera and analyzing the remaining fragments to gain quantitative values of failure strain for both OFHC copper and 1100-O aluminum. Their setup achieved ring radial velocities from around 10 m/s to 200 m/s, covering a significant range of strain rates. Grady and Benson (1983) observed several significant results: 1) the presence of arrested necks or localizations that did not strain to failure, 2) a nearly linear increase in the number of fragments with increasing expansion velocity, and 3) an increase in the average strain at fracture with increasing velocity. Specifically, they showed an increase in strain to failure from 0.22-0.45 for 1100-O aluminum and 0.47-0.65 for OFHC copper. Unfortunately, the last observation, which was achieved by measuring the total length of all ring fragments, was interpreted as an increase in material ductility in proportion to strain rate (Zhang and Ravi-Chandar, 2006).

In the late 1980's, Gourdin (1989) developed a full electromagnetic model for the expanding ring setup, allowing the calculation of the ring loading based upon current measurements and the measurement of stress-strain response using the test. Gourdin also reproduced the experimental results of Grady and Benson, seemingly confirming the strain rate dependence they had found.

Zhang and Ravi-Chandar (2006, 2008, 2009) developed the expanding ring setup further in the mid 2000's by implementing a high speed film camera with combined framing and streak capability, using a pulsed laser to illuminate and expose the film. The unique camera system enabled both high temporal and spatial resolution images to be captured during the expansion process, allowing the identification of localizations during

the test. In contrast to Grady and Benson, Zhang and Ravi-Chandar found that material outside of localized regions did not strain to levels measurably beyond the Considère or quasi-static necking strain and that the prior measured increase in ductility was attributable to the addition of plastic strain accumulated within an increasing number of necks, and not to any significant material strain rate dependence.

In such a way, they found that the results of the experiment supported an extension of Mott's conception of fragmentation, where in the number and development of localizations and fragments in a material with a certain statistical variation in its properties are dependent upon the competition of the background material strain rate and the stress-release waves propagating away from a localization or fracture.

A higher strain rate enables more localizations and localized strain to occur before the stress-release waves generated by such an event can unload the surrounding region, ceasing continued straining within any material having seen the passage of the release wave. At the other extreme, a quasi-static test experiences only a single localization because the release wave unloads the entire specimen before any additional strain is generated in the specimen (Zhang and Ravi-Chandar, 2006). The significance of this observation is that the trends seen in prior expanding ring and high strain rate experiments can be attributed to a structural response governed by natural statistical material variation and dynamic processes, such as Mott's fragmentation model, and not to any significant material strain rate dependence as had been previously reported.

Zhang and Ravi-Chandar (2008) expanded upon this analysis by evaluating the effect of specimen size and cross-sectional aspect ratio under high strain rate expansion,

Specimens of various absolute cross-sectional sizes and various cross-sectional shapes from square to highly rectangular were tested using the same experimental setup. Size and aspect ratio were found to strongly affect the strain reached in the un-necked region of the ring fragments. However, the variation in strain was hypothesized to arise from inertial effects associated with difference in time required for propagation of a nucleated localization across the specimen cross-section, prior to full neck formation and the subsequent unloading of the region around the neck. Once the localization propagates across the entire cross section, a neck forms and unloads the adjacent material, ceasing continued straining outside of the neck. Simulations designed in this manner successfully demonstrated the high variation in homogeneous uniform strain (outside of the necked region) in different size and shape specimens could be explained by this propagation mechanism, eliminating the need for any material strain rate dependence in this case as well (Zhang and Ravi-Chandar, 2008). It is in the spirit of this work that the candidate material (AA5083) was tested in order to evaluate the necessity of strain rate dependence being included in the material model.

2.1 Experimental Setup and Procedure

A variant of Zhang and Ravi-Chandar's experimental apparatus was used to conduct expanding ring tests on 5083 aluminum ring specimens with a 1.6 mm x 1.6 mm square cross-section and a 30 mm inner diameter (see Fig. 2.1).

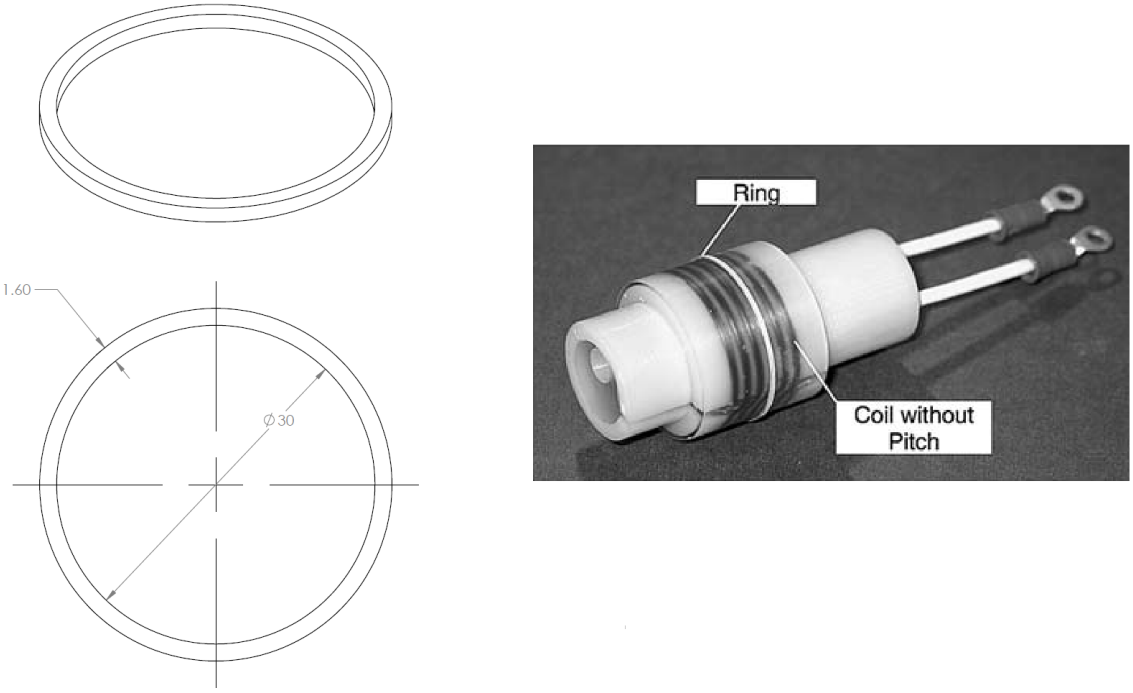

Figure 2.1: Expanding Ring Specimen and Induction Coil (Zhang and Ravi-Chandar, 2006)

The electromagnetic driving device fundamentally consists of a pitch-less solenoid coil, around which the rings are placed, connected to 25μf capacitor (see Fig. 2.2). The capacitor is discharged through the coil by means of an ignitron switch, which is triggered by a pulse generator. Rogowski probes can be placed around the capacitor bank connector and the coil itself to deduce the current provided by the capacitor and the current induced in the ring.

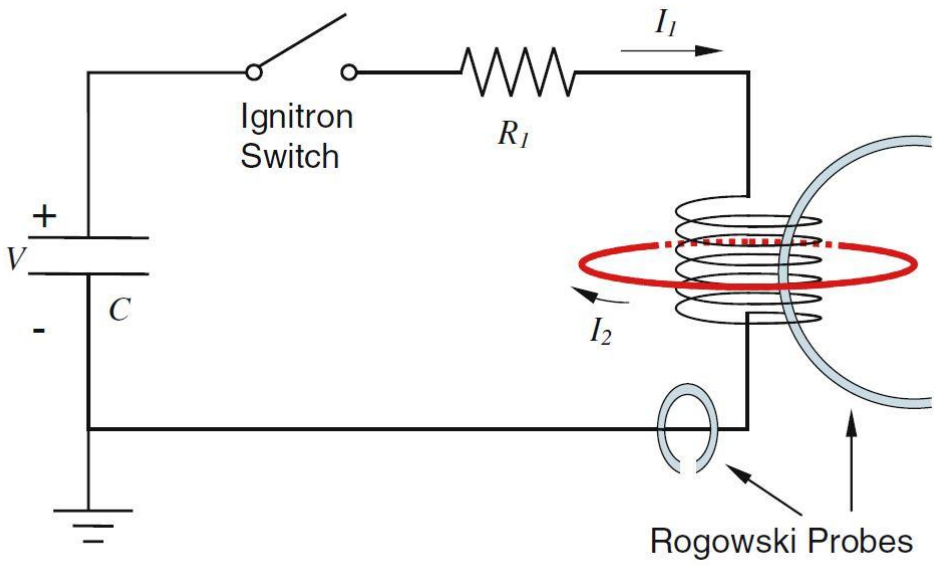

Figure 2.2: Circuit Diagram of Electromagnetic Loading Device (Zhang and Ravi-Chandar, 2006)

The massive and time-varying current discharged through the solenoid generates an intense time-varying magnetic field which in turn induces a current in the ring. By Lenz's law, the induced current in the ring opposes the change in magnetic flux generated by the driving current. The result is counter-rotating currents, causing both the ring and coil to experience mutually opposing radial Lorentz forces. The coil is mounted on a glass epoxy mandrel and covered by a glass epoxy sleeve and is, for all intents and purposes, fixed and rigid resulting in a net expansion force acting upon the ring. In turn, Lenz's law requires the expansion of the ring in order to oppose the net change in magnetic flux caused by the driving current in the solenoid. This interaction creates an outward radial body force on the ring material, placing the ring specimen in hoop tension. A detailed analysis of the electromagnetic model developed for the loading device can be

found in Zhang and Ravi-Chandar (2006). The coil is suspended in a transparent test chamber which is secured by a bench mounted clamp fixture. The glass face of the test chamber provides a clear view of the ring specimen plane for imaging during the test. The circumference of the outer chamber wall is lined with clay to catch and contain ring fragments created during the test.

Images of the ring specimen are recorded using a Cordin 550 high speed camera that is aligned with the axis of the coil and ring specimen. Utilizing an electrically driven rotating mirror and an array of CCD's, the camera is capable of capturing 30 images with 1000x1000 pixel resolution at up to 400,000 images per second. The multiple detectors allow the camera to capture and store high resolution images at very high frame rates, and eliminate the need to read detectors during the event itself. Two Cordin xenon flashlamps provide high intensity illumination for the experiment. The camera and flashlamps, as well as the capacitor bank's ignitron switch, are triggered in proper succession by a Berkeley Nucleonics pulse generator.

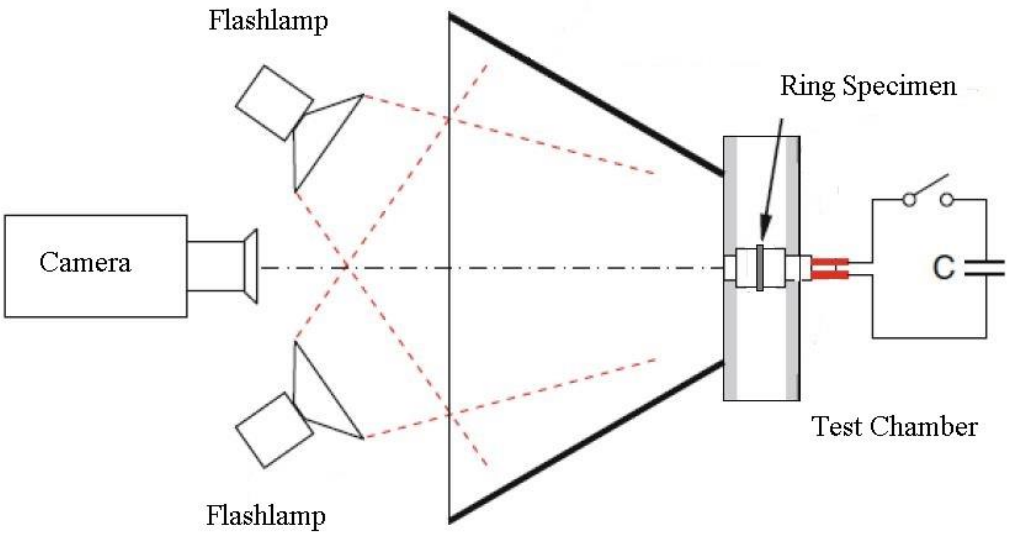

Figure 2.3: Expanding Ring Experimental Setup

Prior work with this apparatus has determined the optimum sequencing of these components, utilizing delayed TTL pulse triggering to provide maximum steady illumination and the most efficient use of the limited number of available frames. All of the presented tests were illuminated using a 1.0 ms flash at a charge level of 7 kV and imaged at 100,000 frames per second. In order to provide as even illumination as possible, a reflective cone was placed in front of the sample chamber as illustrated in Fig. 2.3.

2.2 Results and Analysis

Ten specimens were tested, eight of which were loaded with sufficient energy to generate clear localizations and to fracture the sample. These eight tests are summarized in Table 2.1, and only these are considered in the following analysis.

Table 2.1: Expanding Ring Test Summary

Spec #	Charge Voltage (kV)	Strain Rate (1/s)	# of Fragments	# of Arrested Necks	# Total Necks	Increase in Ring Length (%)	Uniform Plastic Strain
5	9	2800	2	2	4	14	0.115
7	9.5	4900	3	2	5	19	0.120
3	10	5600	4	3	7	25	0.128
8	10.5	5900	5	4	9	31	0.152
6	11	7100	6	2	8	27	0.170
9	11.5	8000	5	4	9	32	0.202
4	12	9700	7	8	15	37	0.206
10	12.5	11300	7	11	18	43	0.211

These specimens were tested at capacitor bank charge voltages ranging from 9.0 kV to 12.5 kV in 0.5 kV increments. A typical series of experimental images (Specimen 3) as captured are given in Fig. 2.4. Images 1-5 (Fig. 2.4) show the expanding ring prior to failure. While ring thinning at necking locations may be directly visible in some images, the images collected by the Cordin camera are not of sufficient resolution to reliably identify the development of localizations during the test.

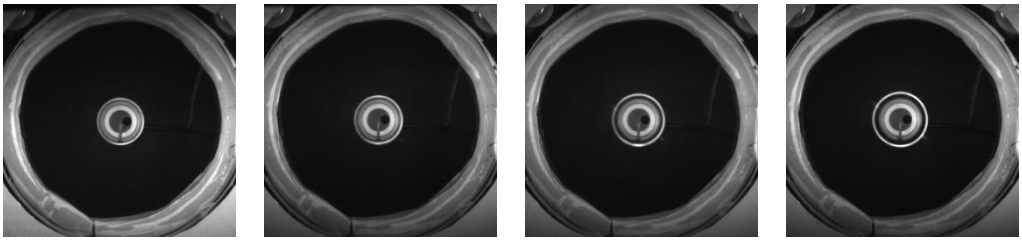
1

2

3

4

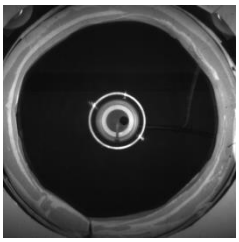
5

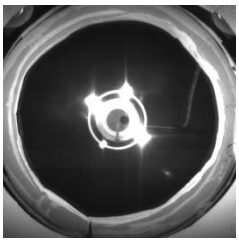
6

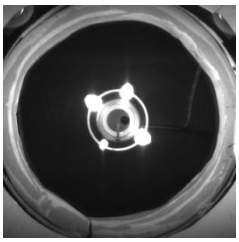
7

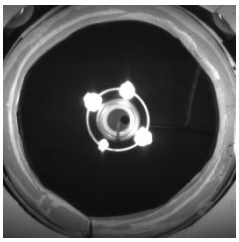
8

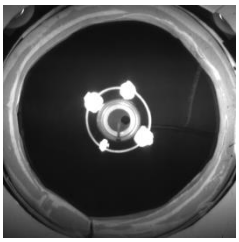
9

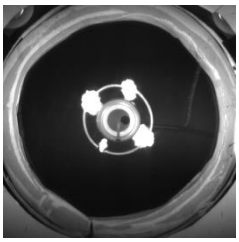
10

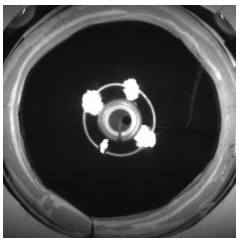
11

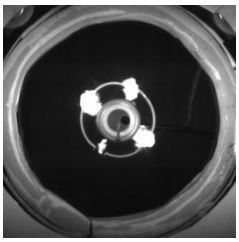
12

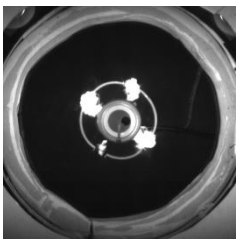
13

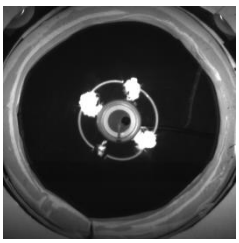
14

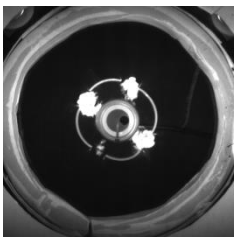
15

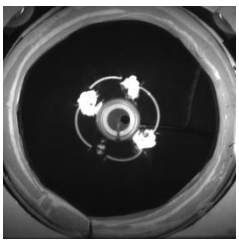
16

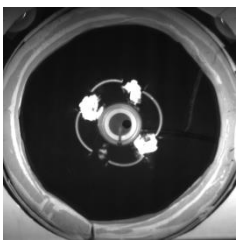
17

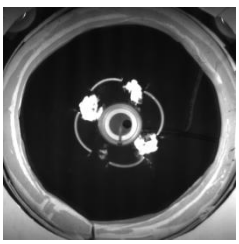
18

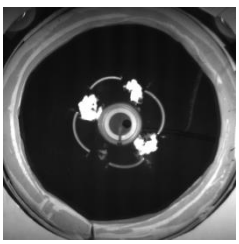
19

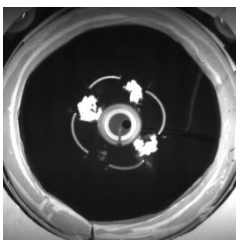
20

(Figure 2.4: Continued next page)

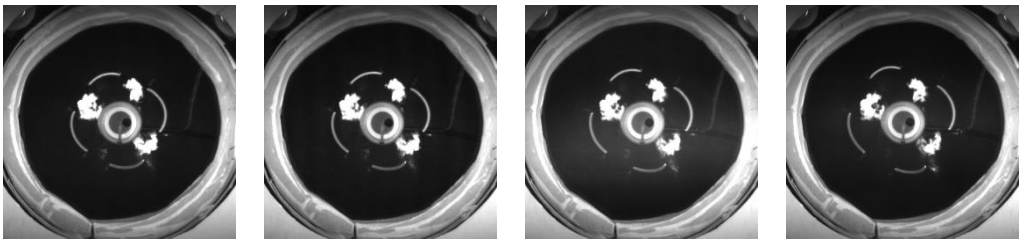

21 22 23 24

Figure 2.4: Experimental Images – Spec 3

However, bright spots in the ring can be seen, indicating surface rotations reflecting additional light. In addition, the points of eventual failure may be brightened by spillover from the collection of images later in the capture and detection cycle of the camera. At the center of the image sits the coil through which the capacitor current flows.

Upon fracture (seen in image 6), the massive induced current in the ring will arc between the fracture surfaces of the new ring fragments, causing highly intense plasma discharges and the vaporization of some of the material.

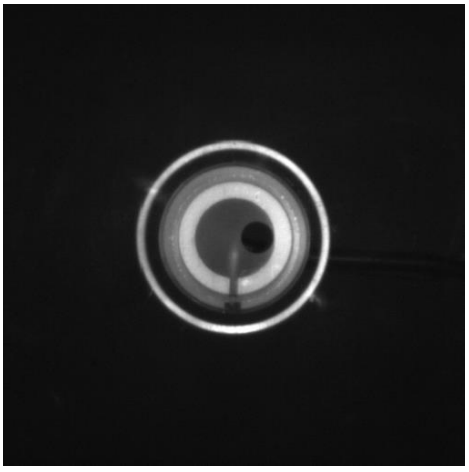

(a) Expansion - Specimen 3

(Figure 2.5: Continued next page)

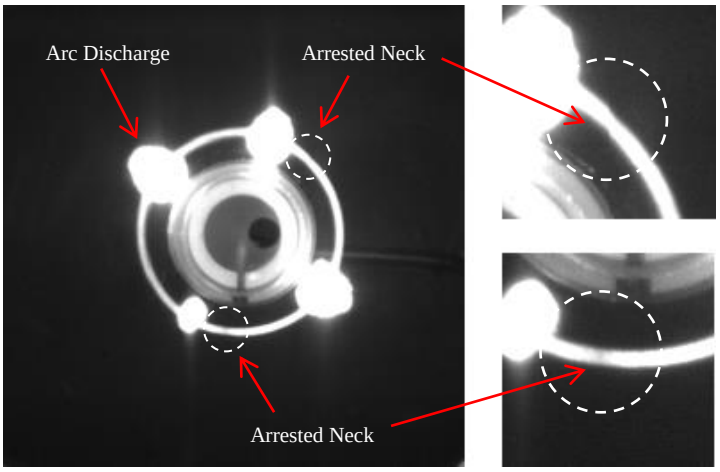

(b) Fracture - Specimen 3

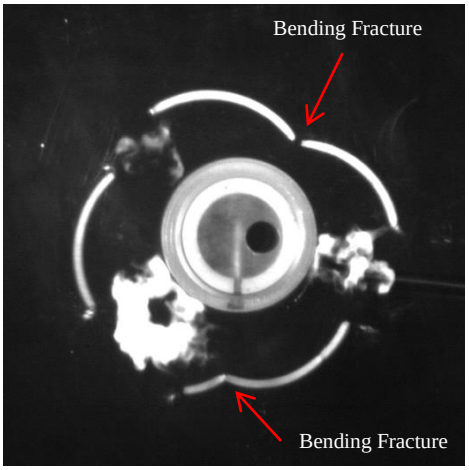

(c) Fragmentation - Specimen 8

Figure 2.5: Selected Experimental Images

Figure 2.5 shows a selection of experimental images displaying relevant experimental phenomena. Figure 2.5b shows the generation of arc discharges at four points of localization and failure (indicated by bright spots) around the same ring shown in Fig. 2.5a. In addition, two necks can be seen near the right top and left bottom discharges (see Fig. 2.5b). It should be noted that the material vaporization and melting associated with the arc discharge at a fracture point will likely destroy the fracture surface and prevent

post-mortem examination of these surfaces. Following failure, the generated ring fragments continue to move under their existing inertia only, as the disruption of the ring circuit removes any electromagnetically induced forcing upon the specimen. Figure 2.5c shows a specimen in which fragment inertia generated bending fractures at two localization points in the ring. At these points, the fracture surface will not correspond to a uniaxial failure. Images after ring fracture are shown in Fig. 2.6 for several capacitor voltages levels.

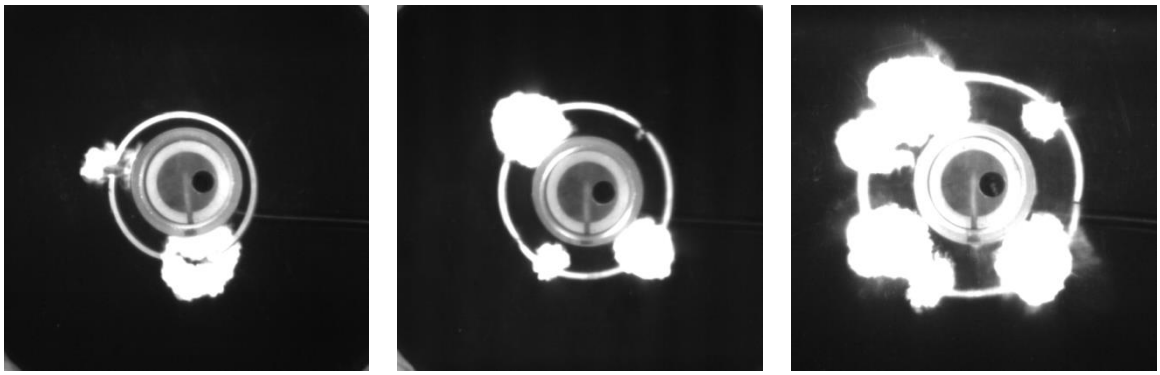

a) 9 kV b) 11 kV c) 12.5 kV

Figure 2.6: Ring Fragmentation at Increasing Capacitor Voltages

For each series, the ring radius as a function of time was measured using a MATLAB image measurement tool to fit an average circle to the image of the ring under expansion. The measured pixel radii were calibrated to a static image of the undeformed ring in the test chamber. The radial expansion velocity of the ring was then calculated by linear regression of the radius history prior to failure. In the case of the higher energy tests, the radius of the ring is a nearly linear function of time (see Fig. 2.7). Note that the fracture

of the ring is indicated by a change in the plot marker, after which the apparent expansion of the ring is due only to fragment inertia.

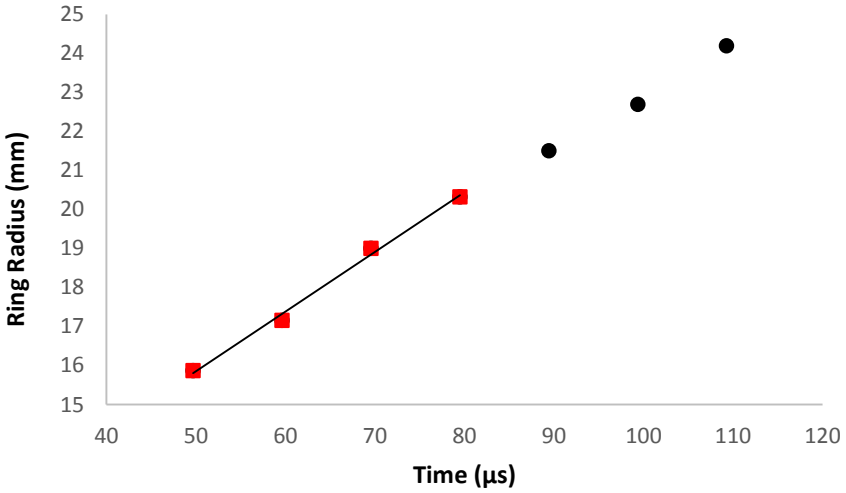

Figure 2.7: Ring Radius vs. Time – 12 kV

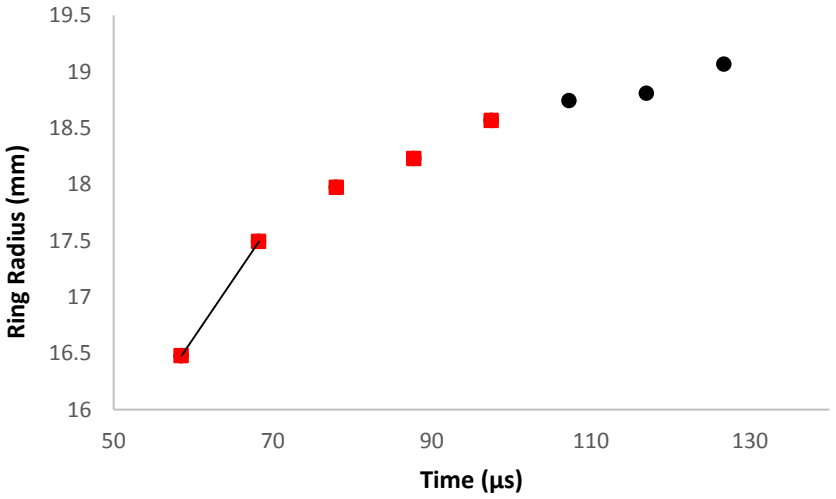

Figure 2.8: Ring Radius vs. Time – 9.5 kV

After localization and failure, the ring fragments retain a large amount of kinetic energy. In the case of a lower energy test, the radius history may not be linear, as very little of the developed energy was retained in fragment inertia (see Fig. 2.7, Fig. 2.8). The radius data for all the measured specimens is given in Fig. 2.9. Note, for comparison the measured values have been adjusted so that Δt represents the measured time relative to the beginning of visible ring expansion.

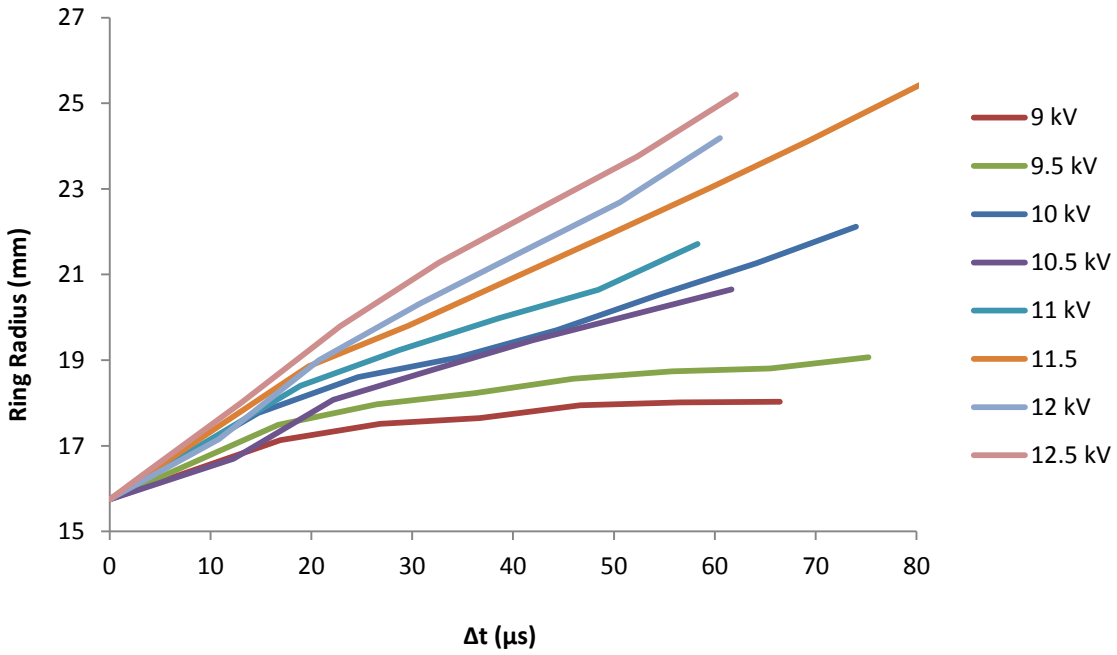

Figure 2.9: Ring Radius vs. Time for all Specimens

In all these cases, the ring expansion velocity was measured over only the images estimated to have occurred prior to localization or taken as the initial velocity observed (see Fig. 2.8). The average hoop strain in the ring is determined by Eq. (2.1), where r is the radius and r_0 is the undeformed radius (15.75 mm):

$$\epsilon = \ln \frac{r}{r_0} \tag{2.1}$$

The average strain rate over the period can then be calculated. After each test, the ring fragments were recovered and inspected post-mortem to determine the uniform strain in the unnecked region of the fragments; these values are shown in Table 2.1. Note that, as established in quasi-static tests, the quasi-static uniaxial necking strain for the material is approximately 12%.

A cursory glance at the estimate total ring strain at failure may seem to indicate at strong strain rate dependence of the material. Indeed results such as these have been misinterpreted as indication of strain rate dependence in the past, but using the original version of this exact expanding ring apparatus, Zhang and Ravi-Chandar (2006,2008) found strong evidence to reject material strain rate dependence in several common metals including 6061 aluminum. Zhang and Ravi-Chandar (2008) found that the increase in total strain was due only to an increase in the number of localizations at higher strain rates, and that the necking strain or the maximum homogeneous strain reached prior to necking instability and localization was constant. This evidence supports the concept of Mott (1947) style fragmentation as the primary determinant of the increase in developed necks and therefore total strain seen in specimens tested at elevated strain rates.

When an initial necking localization forms, it generates a stress release that propagates away from the neck, elastically unloading the material is passes. The finite speed of this wave creates a window of time in which a still loaded material point may continue straining by some increment. At a low strain rate, this increment will be small and unlikely to generate a new localization prior to arrival of the release wave. At high

strain rates, this increment will likely be large enough to allow a new localization to develop. Note that this mechanism assumes some statistical variation in the properties of the material throughout the sample, leading to slight variation in the necking strain at any particular point in the specimen. The cumulative effect of this mechanism is the generation of multiple necks that each unload the regions immediately surrounding it, preventing the material outside of the necked regions from straining much beyond the point of necking instability. As such, the constant necking strain observed by Zhang and Ravi-Chandar (2008) eliminates the need for strain rate dependence in the material constitutive behavior, allowing all the necking phenomena observed to be generated only by the dynamic stress field and its propagation throughout the specimen. Figure 2.10 displays the number and type of necking localizations identified in post-mortem observations of the collected ring fragments.

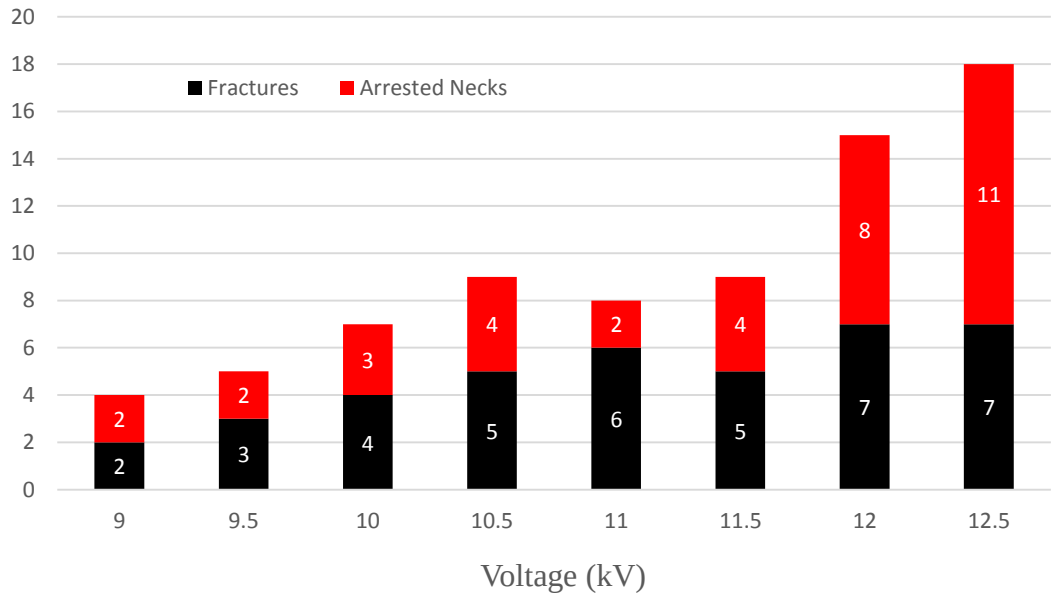

Figure 2.10: Post-Mortem Analysis of Fragment Necks

The increase in both necks arrested by unloading of the specimen and necks resulting in fractures is consistent with the concept of Mott fragmentation and the results found by Zhang and Ravi-Chandar (2006) in Al6061, a generally similar material to 5083.

So, to evaluate the potential strain rate dependence of the candidate material, the homogeneous strain in the un-necked region was evaluated by making post-mortem measurements of the specimen cross-sectional dimensions and associated transverse plastic strains. Assuming conservation of volume and the dominance of incompressible plastic strains, the axial plastic strain at the measurement location was calculated from the measured transverse strains. Dimension measurements of the post-mortem fragment widths and thicknesses were made using a Keyence digital microscope and its built-in image measurement tools. Some examples of ring width measurements are shown in Fig. 2.11. Calculated values for uniform axial strains at several un-necked locations around each ring were averaged to produce an estimate of the uniaxial necking strain for each specimen.

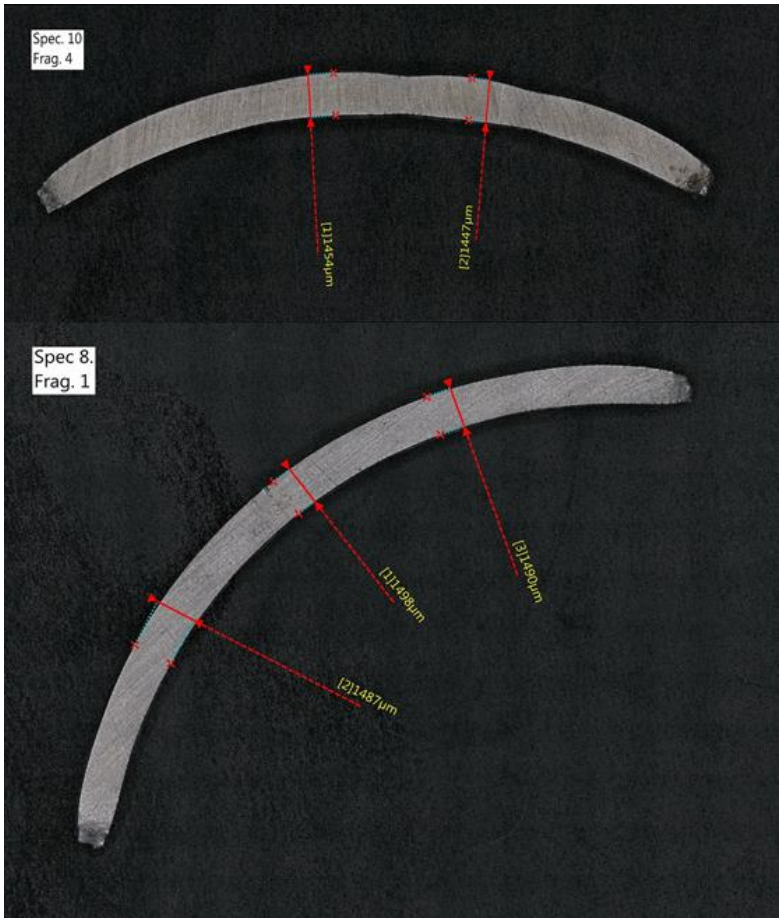

Figure 2.11: Fragment Width Measurements using Depth Composition Images

Similar measurements were made in selected arrested necks adjacent to ring fracture locations, later referred to as secondary neck locations. Figure 2.12 shows this average uniform axial strain as a function of strain rate, where a sharp increase in uniform strain can be seen from 5000 to 8000 1/s.

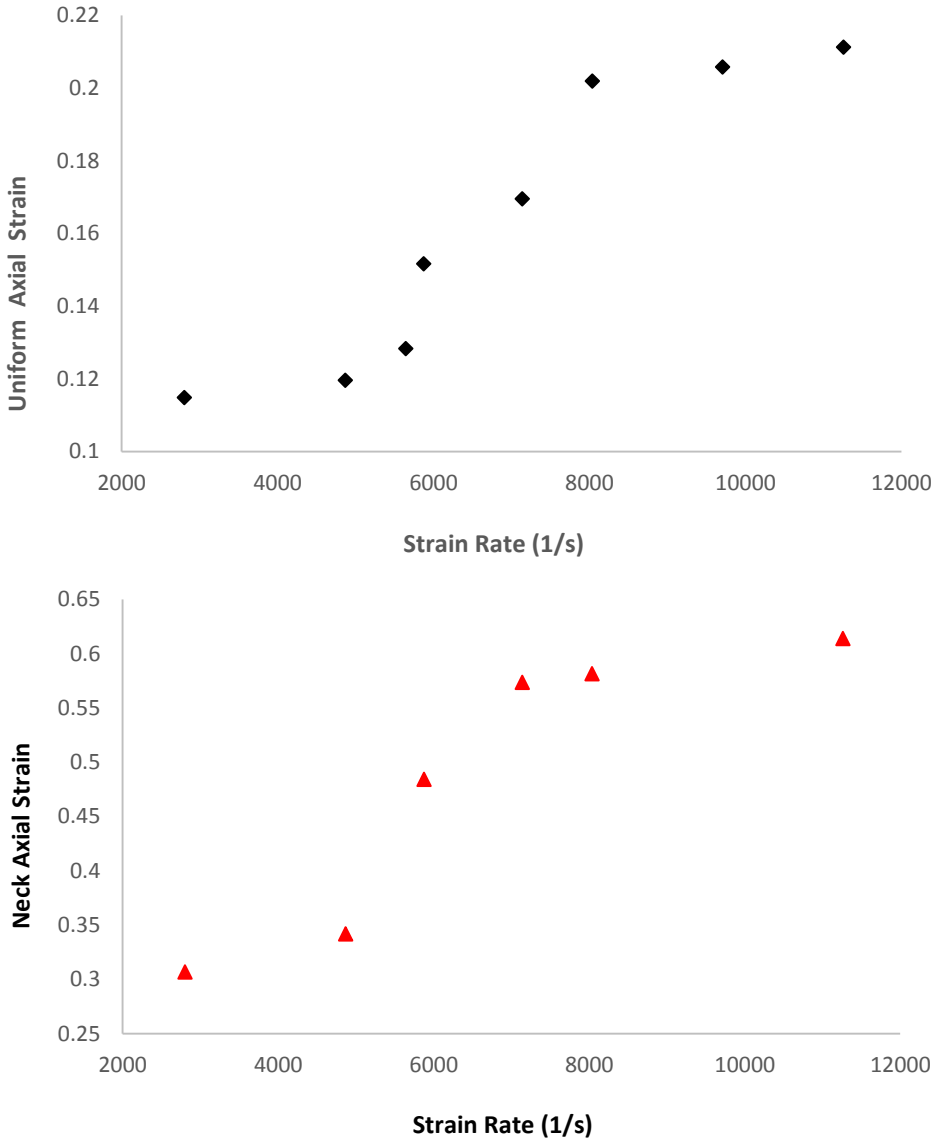

Figure 2.12: Uniform Axial Strains in Un-necked Regions and Maximum Axial Strains within Arrested Necks

While this pattern may seem to require material strain rate dependence, it is believed that the observed step increase in necking strain seen in Fig. 2.12 is due not to material

properties but to inertial effects associated with the physical size and shape of the specimen cross-section itself. Zhang and Ravi-Chandar (2008) observed a similar increase in specimen necking strain in rings with larger physical size (approximately 1-2 mm in largest dimension) and square cross sections.

The proposed mechanism for this dependence relied upon the initiation of localization as some specific point in the cross-section of the ring, requiring the propagation of the localization across the dimension of the cross-section before the specimen scale formation of an actual neck can proceed. As the physical size of the specimen or the maximum distance across the cross-section increases, the time period between the initiation of instability and the specimen scale formation of a neck and the associated release wave increases. While this cross-sectional propagation occurs, the ring material continues to strain under loading. This creates a timescale over which straining may continue beyond localization, prior to release. Once the neck is fully formed, the stress release wave begins to propagate outwards from the site of localization, unloading material as discussed previously. In similar fashion to the standard Mott fragmentation, the increase in uniform strain with strain rate seen in the un-necked regions is due to increased strain increment seen by the material in the time period required for the propagation of localization across the cross-section prior to full neck formation and stress release wave generation.

Supporting this argument is the observation of necking strains approximately the same as the quasi-static uniaxial necking strain (~12 %) at strain rates up to 5000 1/s. Beyond this point, significant additional straining can occur in material near a necked

region before the initiation and propagation of a stress release wave ceases any continued straining at the point. Beyond 8000 1/s, the observed post-mortem distance between developed localizations becomes small (approximately 3-6 ring widths), providing almost instantaneous unloading of any region between necks. It is suspected that the significantly decreased distance between necking locations disrupts the increasing strain seen in Fig 2.12 and leads to the plateau of uniform strain seen at higher strain rates. If valid, this mechanism for the propagation of localization and subsequent development of necks eliminates the need for material strain rate dependence as the increase in uniform axial strain with strain rate is simply a result of inertial effects, finite propagation speed, and therefore absolute specimen size.

2.3 Simulation and Numerical Results

To confirm the role of inertial effects for the increase in necking strain observed experimentally, a series of finite element simulations modeling the fundamental behavior of the expanding ring tests were conducted. A uniaxial model with the same rectangular cross-section geometry as the ring (1.6 mm x 1.6 mm) was created in ABAQUS. The model was reduced to an eighth of a specimen by enforcing symmetry conditions across three planes cutting the origin including the cross-section ($z = 0$) and the longitudinal specimen mid-planes ($x = 0$, $y = 0$) such that the origin of the model is located at the center of the specimen cross-section. The eighth specimen model was meshed using 62,500 linear 3D hexahedral elements (C3D8R) with reduced integration, using a 10 x 10

element cross-section with 625 elements along the 50 mm length of the axis; a perspective view of this model is shown in Fig. 2.13. Standard isotropic Mises plasticity was implemented in ABAQUS, utilizing the Ramberg-Osgood material fit described in Chapter 1. Additional material properties utilized in the simulation can be found in Table 4.2.

The expanding ring test loads the specimen by supplying an outward radial body force on the material, generated by the electromagnetic interaction between the driving capacitor current in the coil and the induced current in the ring specimen. The loading force takes the form of a pulse determined by the electrical properties of the effective capacitor discharge circuit and the interaction between that circuit and the ring specimen. However, as shown in the previous section, given sufficient energy the ring experiences a nearly constant radial velocity and hoop strain rate up to the point of localization and necking in the ring. After necking, the localization generates a release wave that unloads the areas adjacent to the neck, leaving the material under its own inertia.

In order to simulate these conditions on the uniaxial model, a two step analysis was conducted.

1) A velocity field is imposed on the entire specimen such that a uniform axial strain rate is achieved throughout the material. The velocity field varies with the z axis coordinate such that it increases linearly with the axial distance from the origin. This velocity condition is imposed until the axial strain in the specimen is approximately equal to the quasi-static uniaxial necking strain (~12%). Beyond

this point, instability allows for the development of localization along the entire length of the uniformly strained specimen. In order to force the location of the neck, a material flaw was simulated at the center of the specimen by assigning a perfectly plastic material model to the element at the origin of the model.

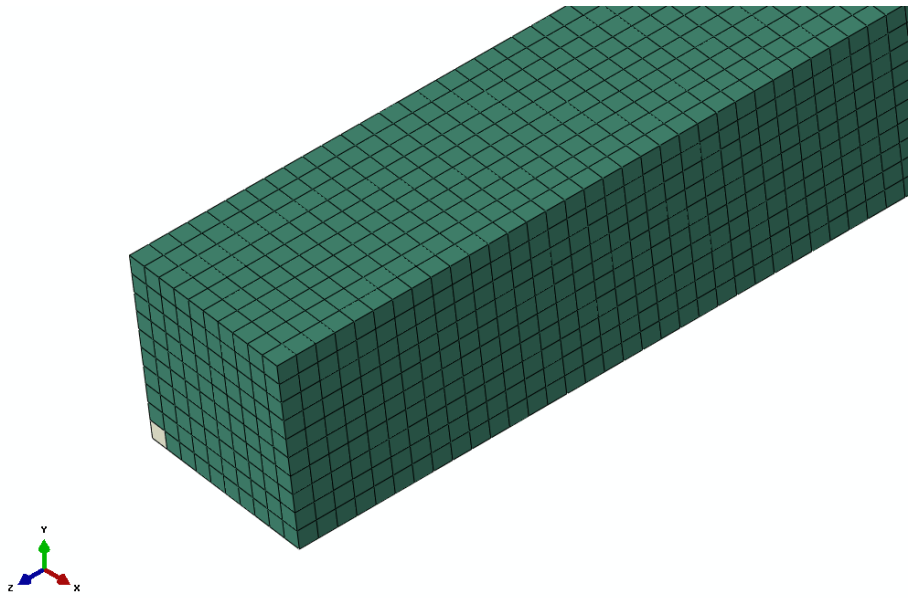

Figure 2.13: Mesh and Material Flaw at Origin and Center of Specimen

The flawed material yields at 100 Mpa and exhibits perfectly plasticity after yielding, inducing the subsequent localization to occur at the $z = 0$ plane of the specimen.

2) Once the specimen uniaxial strain reaches the quasi-static necking strain, the imposed velocity field is removed, allowing the specimen to continue under only its own inertia. Under only inertia, the material begins to unload at the free and

unconstrained end of the specimen. At the constrained surface ($z = 0$), the region at the material flaw localizes and the localization begins to propagate across the cross section as the specimen continues to strain under its own motion (see Fig. 2.13).

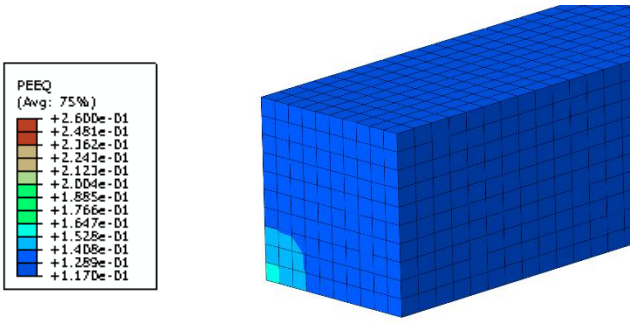

(a) Initialization of Strain Localization at Material Flaw

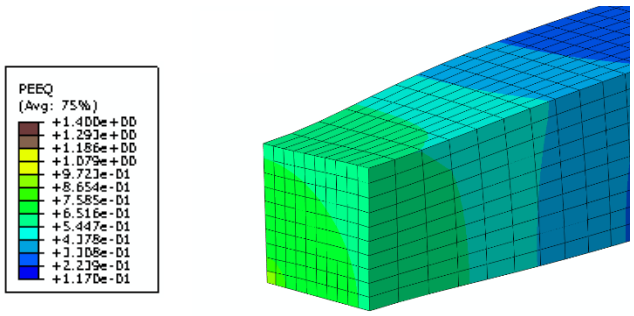

(b) Developing Primary Neck at Origin Plane

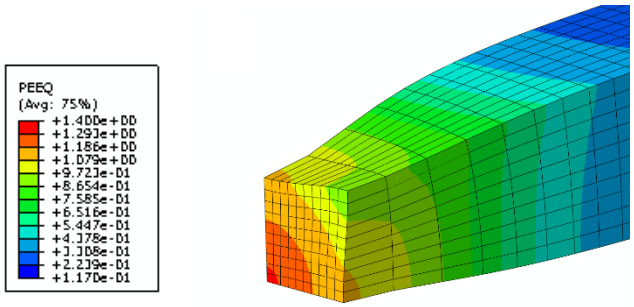

(c) Fully Developed Neck

Figure 2.14: Localization of Strain Initiates at Material Flaw

As the localization reaches the free surfaces of the specimen, a diffuse neck—hereafter referred to as the primary neck, at which location fracture is considered to occur—begins to form at the origin cross-sectional plane. The formation of the diffuse neck leads to the generation of a stress release wave that propagates axially from the site of necking, unloading material points in the process, consequently halting the continued inertia driven straining at the point. Note, while this process occurs at the constrained end of the specimen, the unloading wave created by the removal of the velocity condition at the free end of the specimen is propagating toward the origin. The length of the specimen is chosen to ensure the process at the constrained end (in which we are interested) can occur completely and free of interference from the previously mentioned wave originating from the free end of the model.

The time it takes for the localization to reach the free surfaces of the specimen and development a full neck and release wave allows the adjacent regions to strain beyond the quasi-static necking strain, under its own inertia prior to being unloaded. The inertia given to the specimen under the imposed strain rate then determines the amount of additional strain experienced by a point during this time period. In the actual specimen, fracture would occur at the primary neck as strains become higher. Failure is not implemented in this model, therefore plastic strains in the adjacent un-necked region are measured after full development of the neck.

If the fundamental concept of Mott fragmentation can be applied to the necking process under this basic model of localization propagation, the maximum uniform strain or the strain experienced in the adjacent un-necked region should plateau as the stress in the region is relieved by the neck development. However, under these conditions, the maximum uniform strain will vary with strain rate and the physical size of the specimen cross-section, as observed by Zhang et al. (2008). The simulation result at an imposed strain rate of 10,000 s^{-1} is shown in Fig. 2.15.

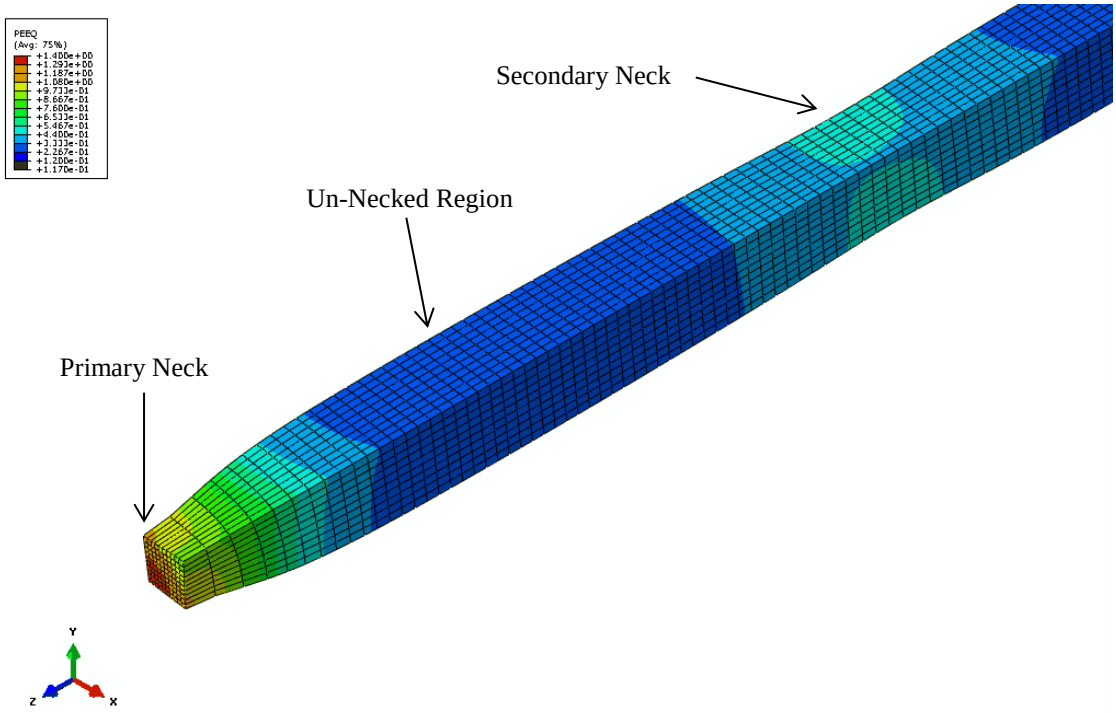

Figure 2.15: Simulation Result at Constrained End (10,000 s^{-1})

Adjacent to the primary neck is an un-necked region where the maximum uniform strain measurement is taken. Note, plastic strains only are considered in this analysis. This region strained until it was unloaded by the neck and would under quasi-static loading conditions represent the quasi-static uniaxial necking strain of the material, 12%. In addition, a secondary neck—defined as an arrested neck adjacent to a fracture location—can be seen developing beyond the adjacent uniform region. Note that no other flaws were generated in the model and the development of this secondary neck is due entirely to the dynamic nature of this simulation and the progression of the material strain beyond the point of geometric stability under inertial forces only. The development of this secondary neck can only occur under dynamic conditions in which the process of stress release is not effectively simultaneous for every material point with respect to the timescale over which strain is occurring, the very fundamental process originally described by Mott (1947).

In order to measure the maximum uniform strain in the model, the plastic equivalent strain along a path on the centerline of the specimen surface was measured after full neck development. This path measured strain is given in Fig. 2.16. The minimum strain in the un-necked region, or the uniform strain, occurs at the local minimum at 2.8 mm.

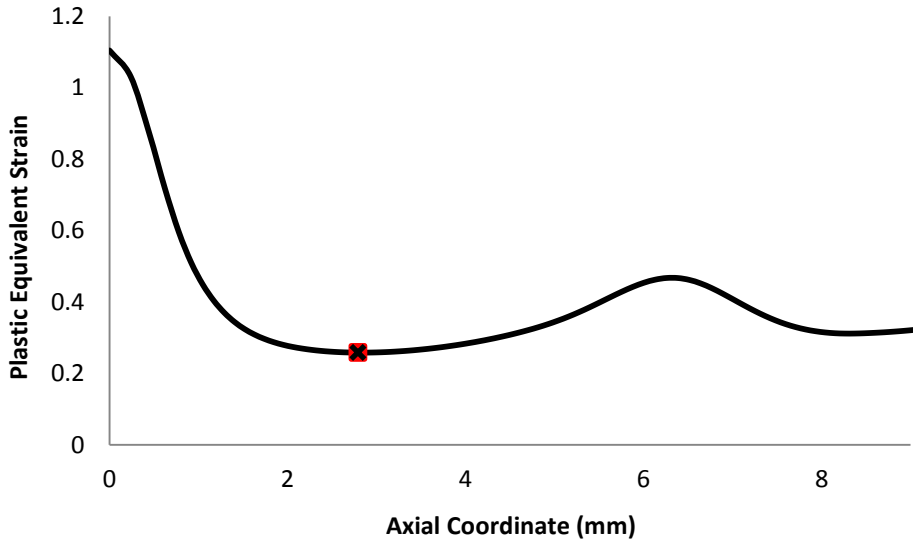

Figure 2.16: Axial Strain vs. Position at 10,000 1/s

The plastic equivalent strain history at the element occupying this position as well as the primary and secondary necks is plotted in Fig. 2.17.

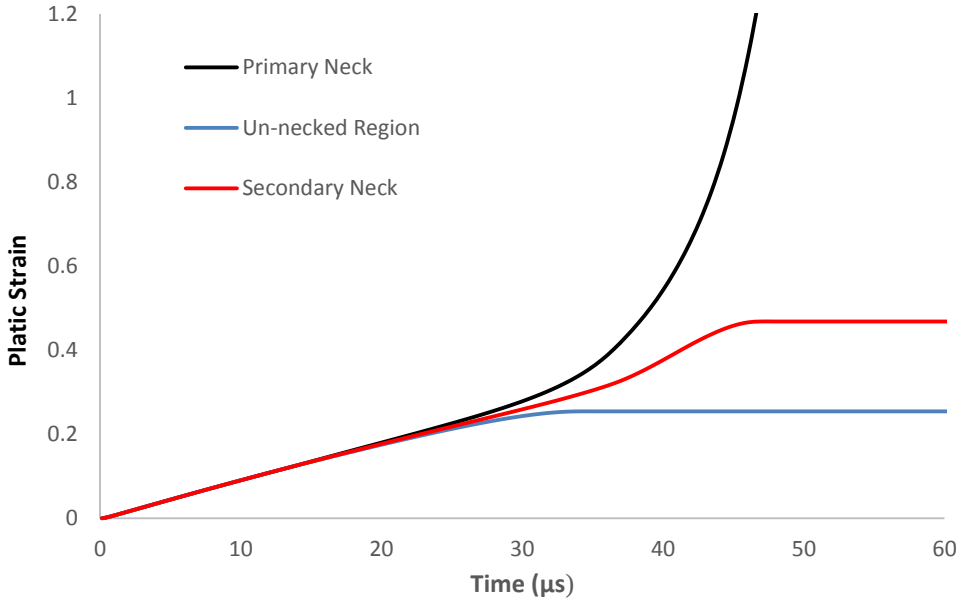

Figure 2.17: Plastic Strain History at Three Locations.

The imposed target strain rate of 10,000 1/s is maintained for approximately 13 μs, beyond which the material point continues to strain under specimen inertia until is unloaded at approximately 32 μs. Beyond this point, no additional local strain is accumulated and the strain level is constant in time. Not long after 13 μs, the strain paths bifurcate, localizing heavily at the primary necks, unloading the un-necked region and the secondary neck in sequence, arresting the secondary neck at 45 μs.

The distance between primary and secondary arrested neck, 6.25 mm, can also be observed along the specimen path. The secondary neck is arrested by stress release, preventing further local strain. The plastic strain path curves for each simulated strain rate are compared in Fig. 2.18.

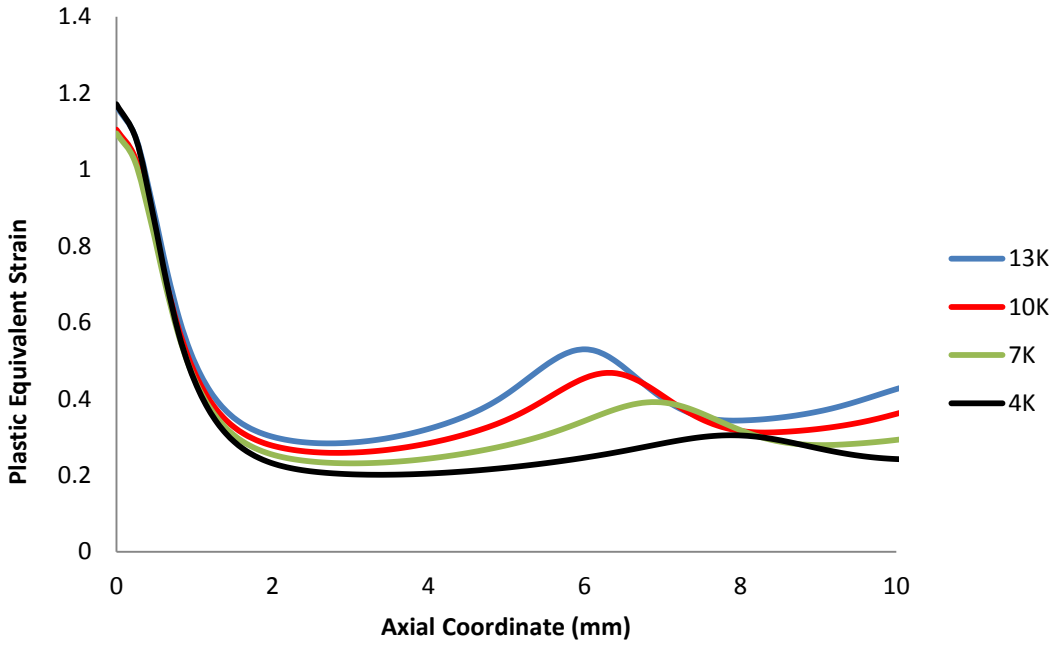

Figure 2.18: Axial Strain Along Surface For Multiple Strain Rates

Several important trends can be seen. First, the minimum strain in the un-necked region, representing the measured uniform strain, increases with strain rate. Zhang et al. (2008) observed the same pattern in specimens of larger physical size and cross-section even though uniform region strains were constant for physically smaller, thinner specimens. Second, the location of both the minimum strain and the secondary neck moves towards the origin with increasing strain rate, reducing the neck-to-neck distance as seen in the experimental results. This equates to an increase in the number of localizations, as seen in the post-mortem analysis of ring fragments, and if allowed to proceed to failure, an increase in the number of fragments. Lastly, the magnitude of the secondary neck relative to the induced neck increases with strain rate. This would be expected under Mott conditions as additional strain can accumulate prior to release under elevated background strain rates. The presence of these trends in this simple simulation lends credence to the assertion that the experimental results are attributable only to the proposed dynamic mechanisms and not to any material strain-rate sensitivity.

Finally, the minimum uniform strain found in the primary un-necked region as a function of imposed strain rate is shown in Fig. 2.19. A substantial increase in uniform strain and an increase in secondary neck strains of similar to that observed experimentally can be seen over the simulated range of strain rates. The increase and level of strains over the range of rates may not match the experimental results quantitatively, but these simulations are far from a perfect analogue to the expanding ring experiment.

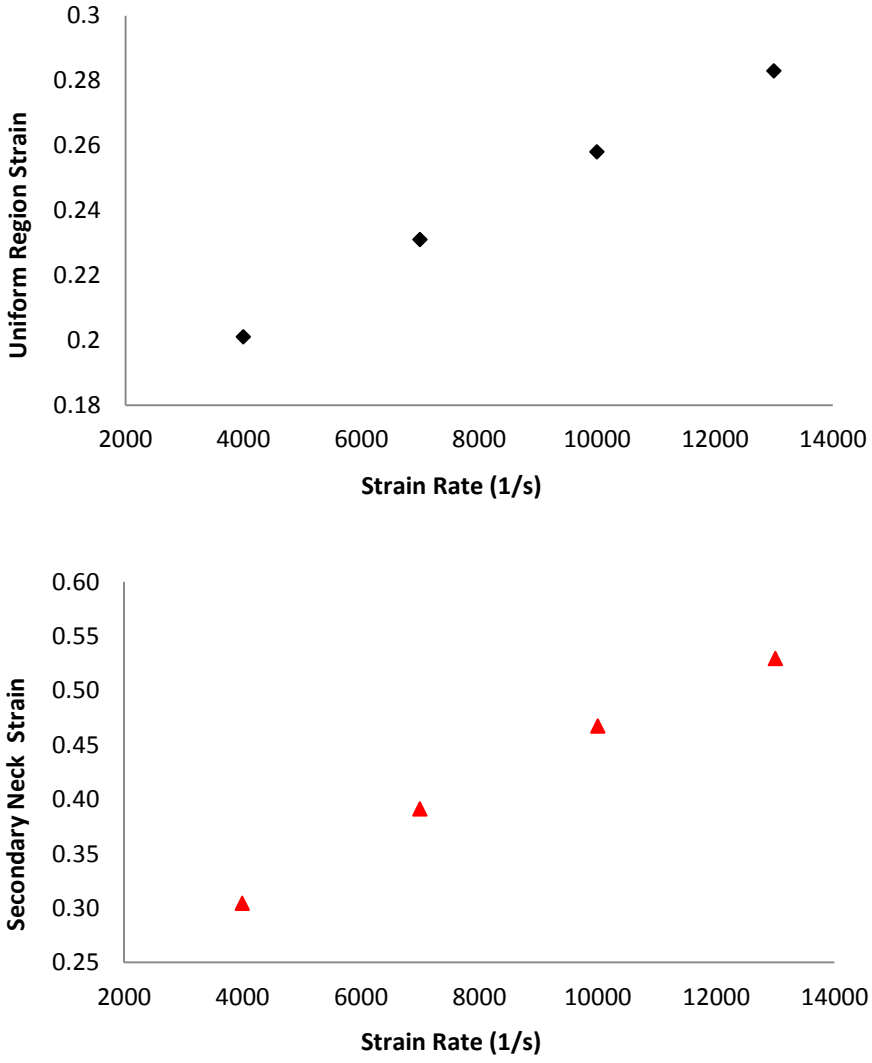

Figure 2.19: Simulated Uniform and Secondary Neck Strains from 4000-13000 s^{-1}

The model described seeks only to evaluate the inertial mechanisms proposed in absence of material complication. The increase in uniform strain is of sufficient magnitude to attribute the increase in the observed experimental data to a mechanism in a similar vein as that simulated, where specimen size and inertia is culpable for the response of uniform

strain to strain rate, rendering a strain-rate sensitive plasticity material model unnecessary. It is therefore asserted that the phenomena observed in the experiment can be generated without any special modifications of the material constitutive behavior, requiring only the unique conditions found under dynamic loading to show the otherwise unexpected strain responses and localization patterns found.

The more complex impact loadings evaluated later in this document show similar patterns to the expanding ring experiment, but depend not only on the stress-strain response and localization mechanisms evaluated here but on the specific nature of the failure mechanisms shown by the material. The next section will evaluate the material failure of the candidate material and how it affects the combined processes of continuing strain and failure seen under impact conditions.

Chapter 3: Interrupted Strain-to-Failure Tests and Material Failure Model Validation

In order to capture the full behavior of a structural response such as ballistic impact, not only must the plastic material response be modeled to high values of strain but the ultimate fracture or rupture of the material must be characterized. The failure of a material can be a very complex process, especially when failure occurs in a volume of material that has experienced significant global plastic strain. This condition is often seen in structures lacking clear pre-existing flaws or cracks, in which substantial permanent deformation is achieved prior to failure. This condition cannot be easily modeled using conventional fracture mechanics and must be addressed at a material level.

Fracture at material scale is often modeled as the cumulative and ultimate effect of damage mechanisms present in a material volume undergoing deformation. Under ductile conditions, in which significant plastic strain occurs within the material volume, the dominant damage mechanism is that of void nucleation, growth and coalescence. As the material deforms, cavities may form at favorable sites including the interface between matrix material and inclusions or second-phase particles. Mechanically, void growth was first analyzed by McClintock (1968) and later incorporated into the plastic response by Gurson (1977) as a means of modeling ductile failure. Analysis of the micromechanics of void growth revealed a strong dependence upon stress triaxiality. Based upon experimental data collected for three metals under various loading conditions, Johnson and Cook (1985) proposed an empirical material fracture locus, expressing the equivalent

strain at fracture in terms of the stress triaxiality T, normalized plastic strain rate and homologous material temperature:

$$\bar{\varepsilon}^f = [D_1 + D_2 \exp(D_3 T)]\left[1 + D_4 \ln\left(\frac{\dot{\bar{\varepsilon}}^p}{\dot{\varepsilon}^0}\right)\right]\left(1 + D_5 \hat{T}\right) \tag{3.1}$$

$$\text{where, } \hat{T} = \frac{T - T_0}{T_m - T_0}$$

Due to its simple nature and relatively easy calibration, the Johnson-Cook (J-C) failure curve is often utilized in numerical computation. Similar to the related Johnson-Cook plasticity model, its provisions for strain rate dependence and thermal effects makes it an attractive empirical failure model for use in dynamic analyses, in which both effects may be present. As developed in Chapter 2, the candidate material shows material strain rate independence with respect to plastic behavior in the expanding ring tests conducted. This observed strain rate independence will be extended to the failure model as well.

In order to model the material damage present at any given state of stress achieved after a given loading history, J-C damage is usually implemented using a cumulative damage variable D, which follows a fractional or incremental summation rule similar to Miner's Rule:

$$D = \sum \frac{\Delta \bar{\varepsilon}}{\bar{\varepsilon}^f} \tag{3.3}$$

Where $\Delta\bar{\varepsilon}$ is the increment of plastic strain at the current triaxiality level and $\bar{\varepsilon}^f$ is the failure strain level at the same triaxiality. This rule reflects a linear accumulation of damage at any given stress triaxiality. However, a damage model of this type may be implemented in several ways. A damage initiation specification is often used such that no damage is accumulated below a threshold value of effective strain at a given stress triaxiality. The evolution of the damage variable may also be coupled or uncoupled to material properties and response. A coupled analysis may be used to degrade the macroscale material properties such as elastic modulus, E, (or the effective flow stress):

$$\tilde{E} = E\,(1 - D) \tag{3.3}$$

In this case, the stiffness of the material is degraded linearly with increasing damage parameter. An uncoupled analysis, on the other hand, preserves the initial material response until critical damage is reached (D=1), and the material fails. In the uncoupled case, no material degradation may be applied to the material response, but the damage parameter is still calculated in a linearly cumulative fashion (LeMaitre, 1996). An alternative formulation with $D = \bar{\varepsilon}/\bar{\varepsilon}^f$ at the current value of triaxiality as the damage parameter has no accumulation, but is not commonly used.

A potential problem arising from this commonly utilized approach is that while the failure strain itself varies with triaxiality, the nature of damage accumulation is the same at both high triaxialities, where the dominant growth of voids have been frequently observed throughout the loading history, and at low triaxialities, where the mechanisms

of material damage are less understood and void growth is more difficult to measure. At low triaxiality, matrix material flow may effectively prevent the nucleation and growth of voids during the majority of the strain history. In this case, the accumulation of damage leading to fracture must be non-linear, creating a condition where no material degradation takes place until levels of strain close to the failure strain are experienced. A uncoupled model loading history at a single value of triaxiality may not be significantly affected by this discrepancy but a loading history experiencing an evolution of triaxiality will suffer as a cumulative model will predict more damage accumulation at low triaxiality than is actually experienced.

In the case of a fundamentally non-linear mechanism for the accumulation of material damage in a real material, an uncoupled strain-to-failure model (where failure initiation occurs upon reaching the fracture locus) is a realistic empirical model of material failure. However, the presence of a Miner's style, linear cumulative rule for the determination of failure initiation retains the previously discussed issue under a variable triaxiality loading path, which is present in almost all manifestations of structural failure. Under ductile conditions, a material fracture model such as Johnson-Cook is usually implemented by means of numerical simulation. Indeed most conventional finite element programs, such as ABAQUS, implement linear accumulation of incremental damage.

In order to accurately implement a failure model of this type in a numerical finite element simulation, an appropriate fracture locus must be determined, and the method of damage initiation and damage evolution must be validated. The remainder of this chapter

attempts to investigate the validity of damage accumulation as commonly modeled and the validity of a Johnson-Cook strain to failure calibrated to this material.

3.1 Experimental Setup and Procedure

To evaluate the both the failure locus of the candidate material (AA5083) and the effect of loading path upon the failure strain, a series of tests were conducted upon specimens, sequentially loading the material under different states of triaxiality. For the purpose of this investigation, the strain-to-failure curve given in Fig. 3.1 will be considered a benchmark model for this material. This failure curve was previously calibrated for AA5083 at the University of Texas by Xavier Poulain. Specifically, it was generated by means of local grain-based strain measurements, ensuring the smallest meaningful gage length of measurement possible and the most physically realistic measurement of material scale strain-to-failure.

The testing procedure consisted of two effective loading schemes. The first test loaded a previously underformed material specimen at a triaxiality of zero by means of an Arcan shear test. The material was then loaded under significantly higher triaxiality by means of a notched tension test. The initially applied shear represents an effective distribution of plastic pre-strain, which was generated at low triaxiality. Any ductile damage generated by this loading process exists in proportion to this distribution of pre-strain. Applying subsequent loading to the material volume at a higher triaxiality should

induce an appropriately modified rate of damage generation. An example of this process is shown in Fig. 3.1.

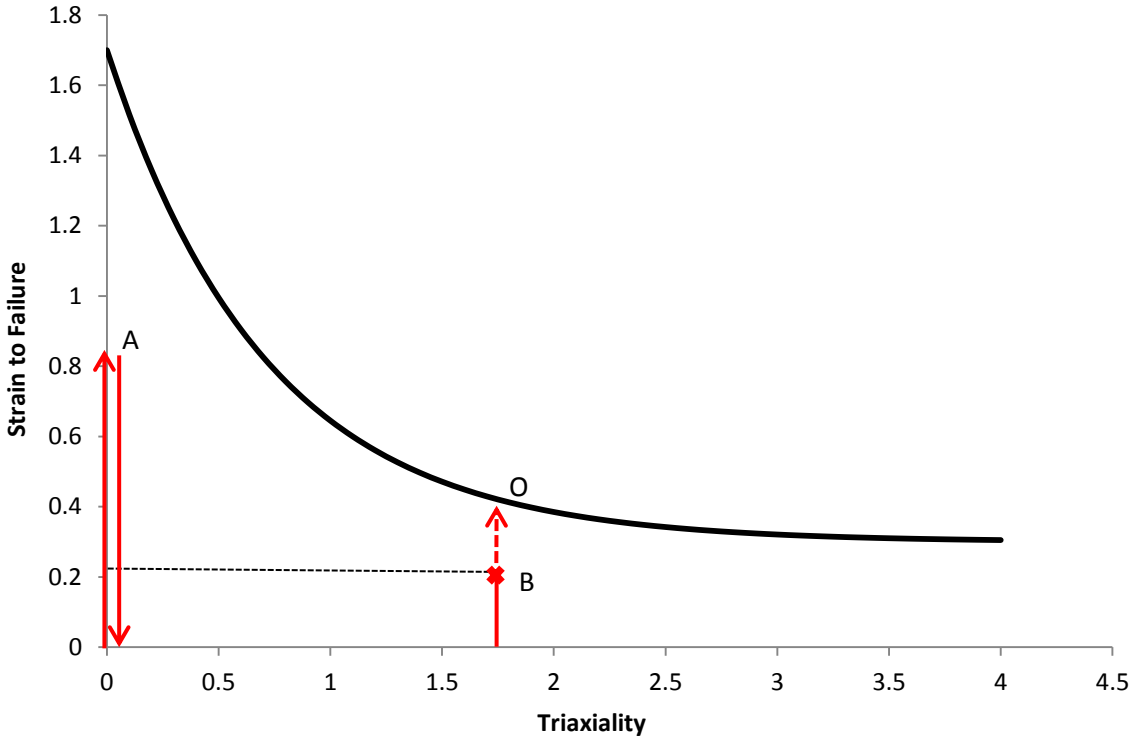

Fig. 3.1: Example of Multi-Stage Loading Process with Johnson Cook Curve

Initially, the material is loaded at low triaxiality to point A. The strain at point A represents 50% of the strain-to-failure at zero triaxiality. If linear damage accumulation is experienced, then 50% of the damage lifetime of the material has been depleted. The specimen is then unloaded, reconfigured and reloaded at higher triaxiality. The strain-to-failure has been reduced at this higher triaxiality, so again assuming that 50% of the damage life has been previously expended according to Miner's rule, the specimen is

expected to fail at point B, only 50% of the way to the original failure curve. However, if the material strains beyond point B, it would be evidence that the linear damage accumulation in theory cannot hold at low triaxiality. Additionally, if the material strains to the original failure curve (point O), then no effect upon the material strain-to-failure has been induced by the shear loading, indicating no previous damage accumulation at all. By means of this process, the presence of real damage accumulation in the material a low triaxiality can be evaluated. Additionally, the failure strain seen the undeformed material may be used to verify the benchmark curve, validating its use in both the experimental analysis and modeling effort.

In order to accomplish this loading scheme in practice, two specific test geometries are utilized. First, Arcan shear specimens (see Fig. 3.2) were loaded under pure shear to varying levels of shear strain, and unloaded prior to failure, after accumulation of plastic strains to different levels.

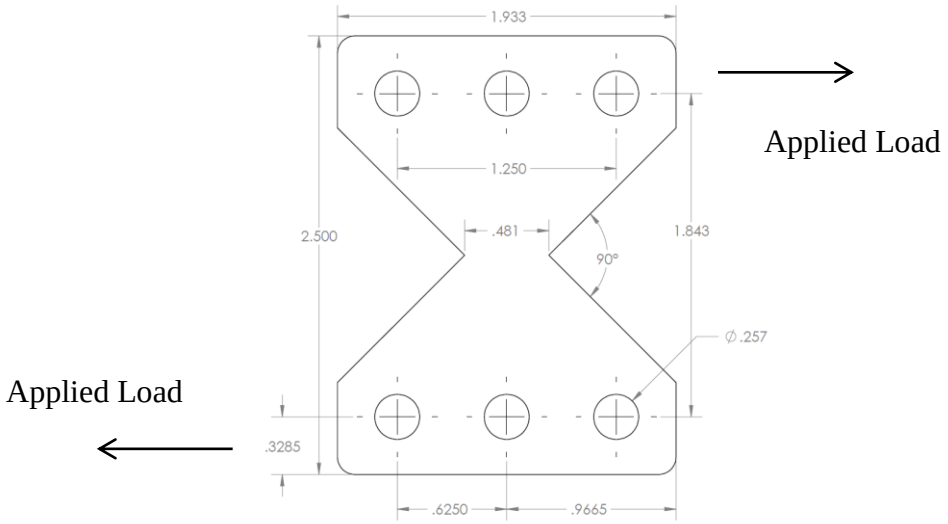

Figure 3.2: Arcan Shear Specimen (dimensions are in inches)

The failure of the specimen is determined not by the bulk material state of strain, but by cracks nucleated at the notches defining the gage section of the specimen. The site of initial cracking (the 45° notch tips) experiences a higher triaxiality than the center of the specimen gage section (which is at zero triaxiality). The cracks nucleated at these sites propagate inwards in a stable manner, causing structural failure of the specimen. In this way, the Arcan test cannot be used to directly measure the strain-to-failure of the material under shear. For the purposes of this experiment, it was used to place the center volume of the specimen in a state of shear. The specimens were unloaded at various levels of global deformation, providing a varied set of equivalent plastic strain distributions across center volumes of the set of specimens, all achieved under shear loading at zero triaxiality.

3.2 Experimental Results

Images of the gage section of the deformed Arcan specimens are given in Fig. 3.3. The maximum surface shear angle (γ) observable in the center gage section of the deformed specimens was used to estimate the equivalent plastic strain. The distribution of shear strain varies only in the vertical direction in the center region of the gage section. In the outer regions, cracks propagating inward from the notches (visible in all three images of Fig. 3.3) interfere with the nominal shear strain distribution generated by the loading.

S1 ($\gamma = 39°$) S2 ($\gamma = 51°$) S3 ($\gamma = 60°$)

Figure 3.3: Deformed Arcan Specimens. The vertically aligned surface marks due to the rolling process allow the clear observation of shear angle.

Note, that the specimens were cut (by electrical discharge machining or EDM) so as to be vertically aligned with the rolling direction of the AA5083 sheet material, providing the visible surface lines with which all optical measurements were made. For comparison, digital image correlation was performed upon a specimen loaded to the maximum displacement achieved (see Fig. 3.4).

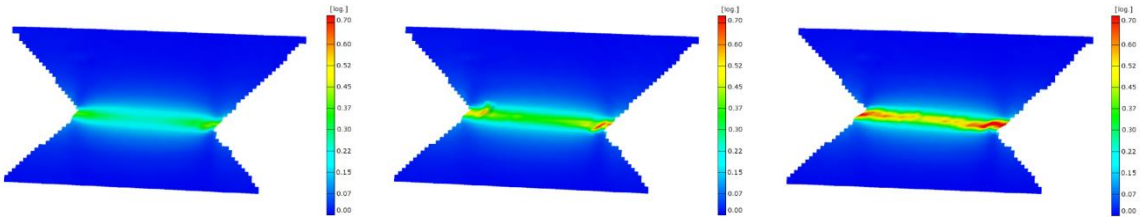

S1 ($\epsilon = 0.23$) S2 ($\epsilon = 0.36$) S3 ($\epsilon = 0.5$)

Figure 3.4: DIC of Arcan specimen with contours of equivalent plastic strain. Specimen structural failure ultimately occurs due to propagation of cracks generated at the notches. The very high indicated strains seen in S3 at the notches are results of this cracking.

As indicated by Fig. 3.4, the shear strain distribution is concentrated across the gage section of the specimen, defined by the line of minimum width between notches.

Second, to accomplish the next loading stage, notched tension specimens featuring a 0.2 mm notch radius and a 1 mm gage width (minimum distance between notches) were cut (by EDM) from the deformed Arcan specimens (see Fig. 3.5).

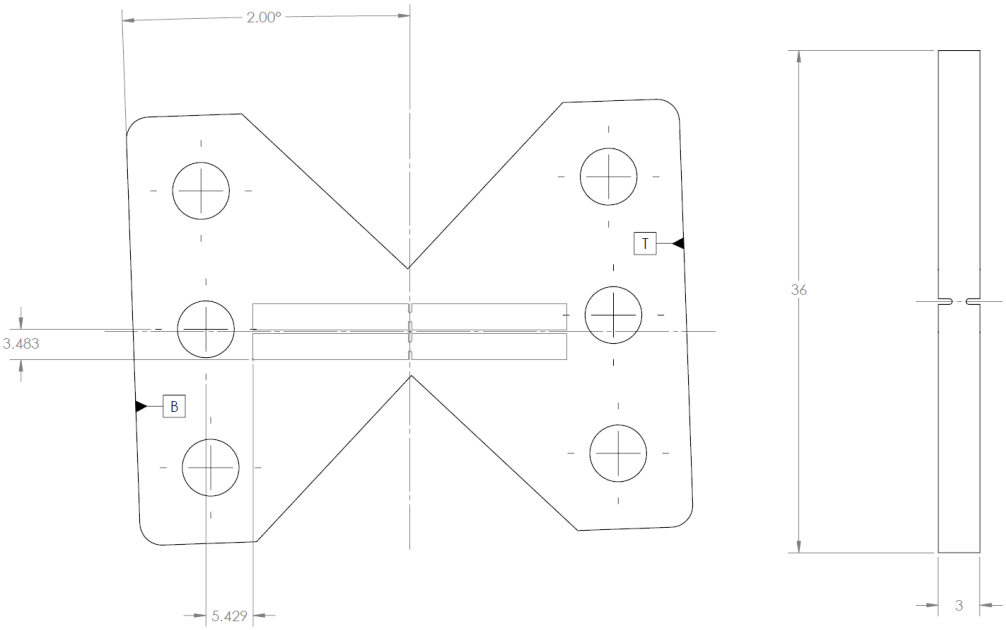

Figure 3.5: Notch Tension Specimens From Arcan Specimen (mm)

Two notched tension specimens were cut from each previously deformed Arcan specimen. Note, they were cut at a 2° angle relative to vertical in order to compensate for the slight tilt of the shear band induced by the slight migration of the Arcan notches

during the deformation process, and to most successfully center the gage section of the notch tension specimen with respect to the shear distribution in the Arcan stock.

The newly machined notched tension specimens, each having a different distribution of shear and maximum equivalent plastic strain occurring at the location of the notch (± 100 μm uncertainty in the location of the machining pattern corresponding to approximately half the notch radius), were then loaded under uniaxial tension using a 1000lb compact load frame (MTII Fullam SEM Tester). The compact load frame was placed directly on a microscope stage allowing the specimen surface to be imaged directly at 150X using a VHX 5000 Keyence Digital Microscope. The native surface texture at this magnification provided a pattern sufficient for the use of DIC. The specimens were loaded in displacement control at a speed of 0.02 mm/min and imaged at a rate of 4 images/min until failure. A representative load-displacement curve is shown in Fig. 3.6. Note, that the serated portion of the curve post-yield indicates the presence of PLC effect within the actively straining regions of the specimen. All specimens tested showed a flat region prior to loading indicating a period over which slack, backlash and slippage in the load frame was taken up.

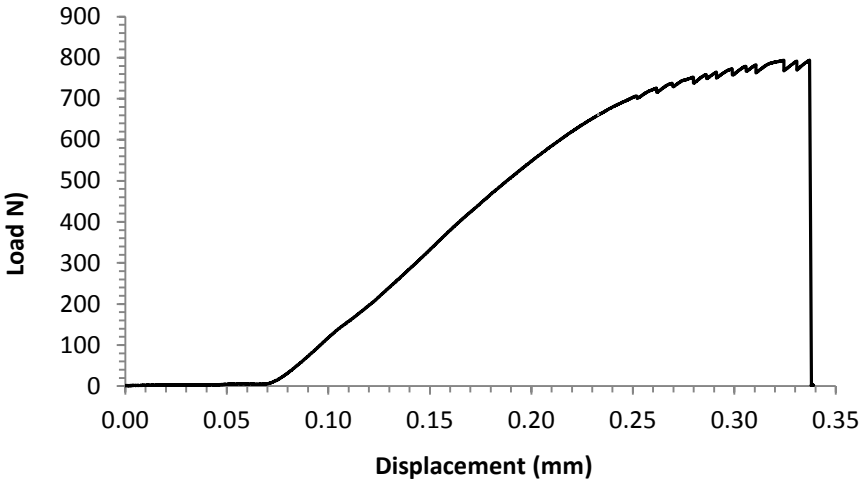

Figure 3.6: Load vs. Displacement for Specimen S2. Slippage and Backlash of the Load Frame Mechansim Occur Unitl Approximately 0.07 mm.

Video analysis of samples near failure showed total failure to occur between frames at maximum acquisition rate, so strains at failure are only approximated by inspection of the last available image prior to fracture. Because true failure occurs after our measurement point, the results are considered a lower bound on the true failure strain. Note that, only successful correlation of the notch region itself is needed to accomplish the relevant strain measurements; so the last image prior to failure that achieved useable correlation was utilized for the measurement of strain regardless of degraded correlation outside of the region of interest. DIC analysis of these images are given in Fig. 3.7 for the pre-strained specimens S1-S3 and a notch tension specimen without pre-strain, cut from undeformed material, U1. The reference locations for representative strain measurements at the center and edge of the notch are also given in Fig. 3.7.

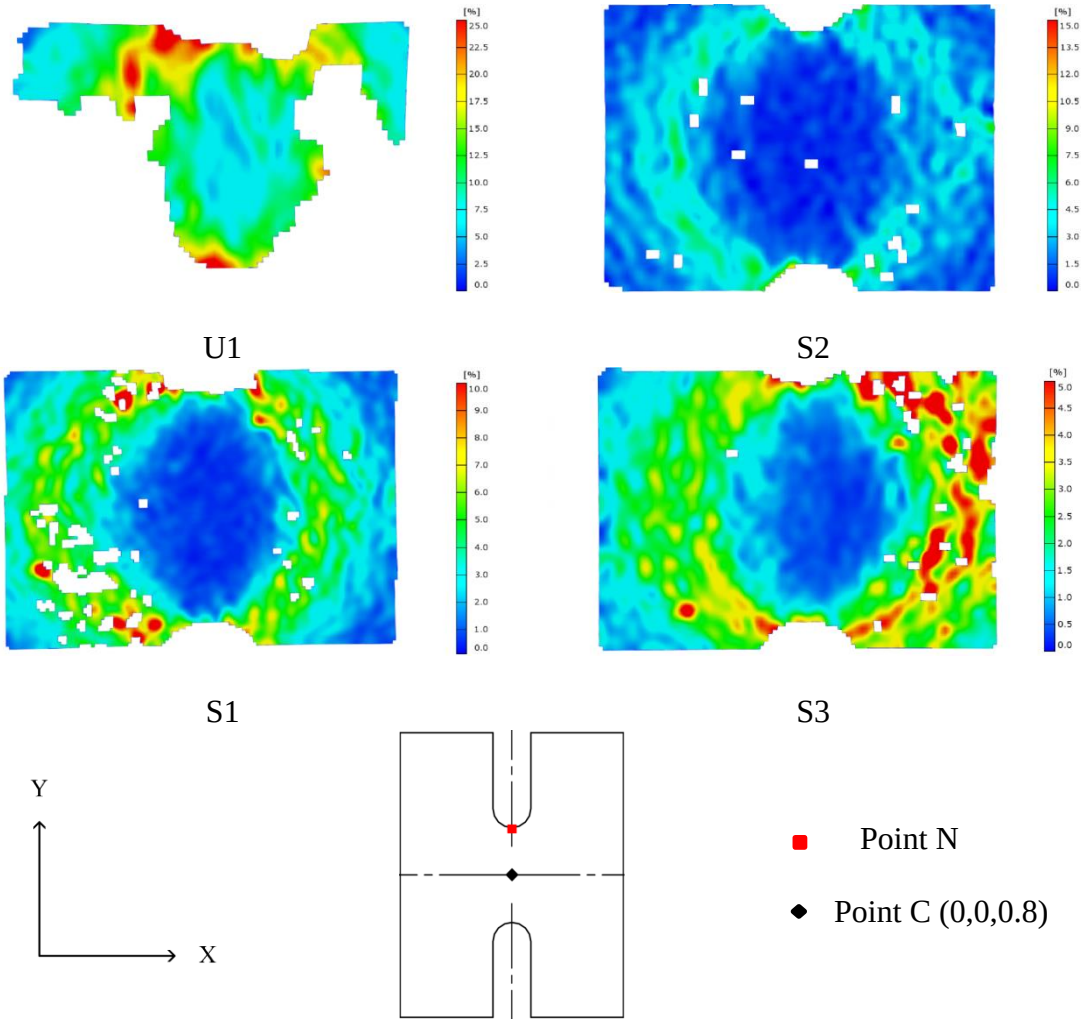

Figure 3.7: Notch Tension DIC Results and Specimen Map at the Last Frame Prior to Failure of the Specimen

A summary of the measured equivalent strains at the center of the specimen surface (Point C) and the edge of the notch (Point N) along with the experimentally measured pre-strains is given in Table 3.1.

Table 3.1 – Notch Tension Test Measurements

Specimen	Pre-strain	ϵ @ C (%)	ϵ @ N (%)
U1	0	6	24
S1	0.23	1.2	5
S2	0.36	0.25	5.7
S3	0.5	0.54	3.8

Note, that the reported strain values for the notched tension specimen tests represent the additional strain measured over this second loading process or the net change in total equivalent surface strain induced by only the notch tension deformation. The total equivalent strain experienced by the original stock material at a reported specimen point is found by the addition of the given pre-strain and the reported notch tension test strain. The approximate surface strains at failure as a function of pre-strain are given in Fig. 3.8.

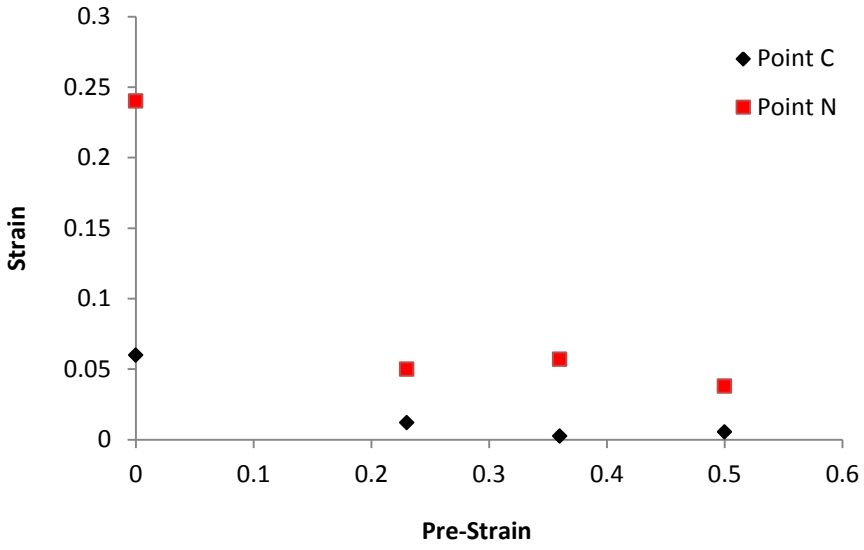

Figure 3.8: DIC surface strains at center (Point C) and notch (Point N). Due to nature of DIC, results at the exact edge of the notch cannot be evaluated, but are measured at a location approximately 25 μm in from the edge. All simulation measurements are adjusted to compensate for this discrepancy.

The surface strains generated in the pre-strained specimens are small in comparison to the virgin material. Indeed, the highest surface strains are seen outside of the notch center in two arcs or strain bands bridging the notch boundaries. However, the thick cross-section of the specimen (1.6 mm sheet thickness) generates a strong plane strain condition in the interior of the specimen. It was hypothesized that the visible bands represented the surface appearance of two intersecting strain bands stretching through the thickness of the material. The internal structure of the deformed specimen is investigated via finite element simulation later in the chapter.

Despite the low surface strains observed in the notch region for all of the tests, fracture ultimately occurs within the notch region, suggesting crack origination within the thickness of the specimen, in a location not visible by experiment. The fracture surface of S1 obtained using depth composition of images performed using the Keyence digital microscope is shown in Fig. 3.9.

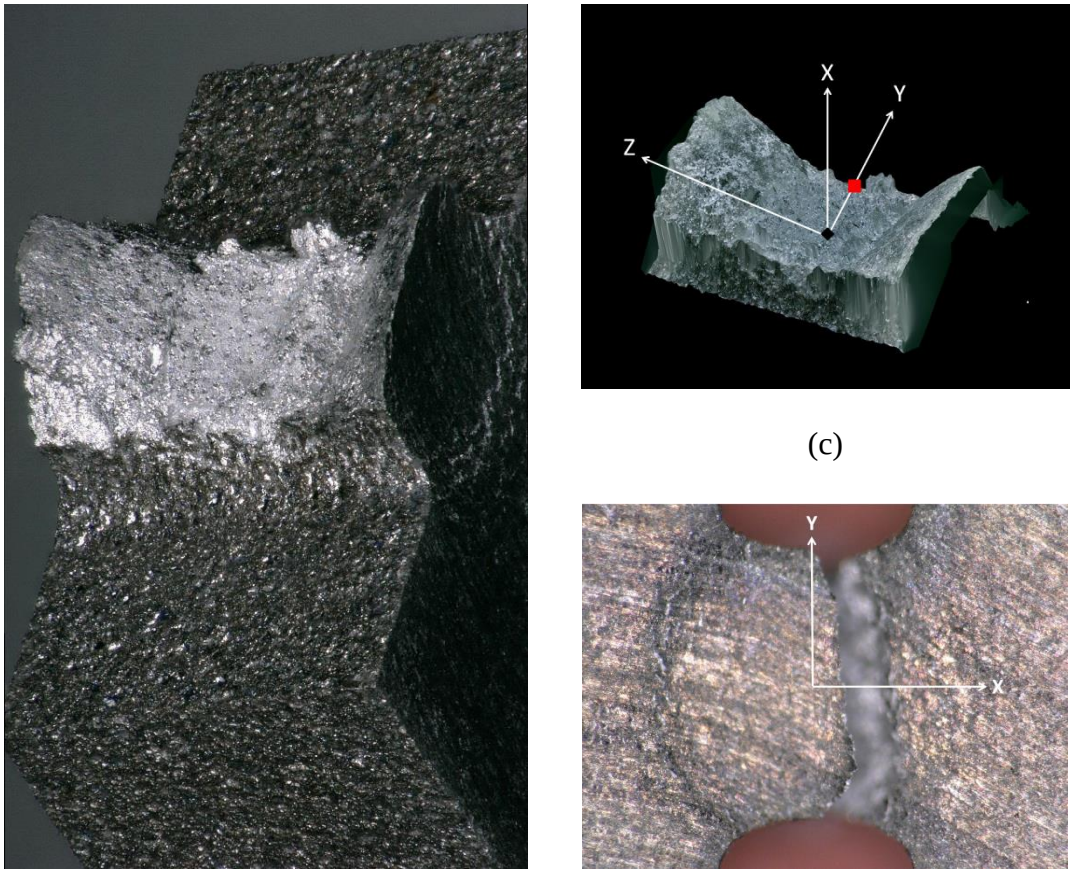

(a) (b) (c)

Figure 3.9: Fracture Surface of Specimen S1: (a) oblique angle view of fracture at notch (b) specimen X-Y axes on surface view (c) X-Y-Z axes at fracture surface midplane with measurement Point C_0 (♦) and Point N_0 (■).

The fracture surface of S1 shows a set of well-developed 45° lips with a relatively flat fracture surface at the center of the volume. Additionally, significant thinning of the notch region is directly visible. The high strain band at the periphery is also visible. Since low surface strains were directly measured via DIC, it becomes immediately apparent that significant plastic strain must occur within the interior of the notch volume. A profile of the fracture surface through the thickness along the z-axis is shown in Fig. 3.10.

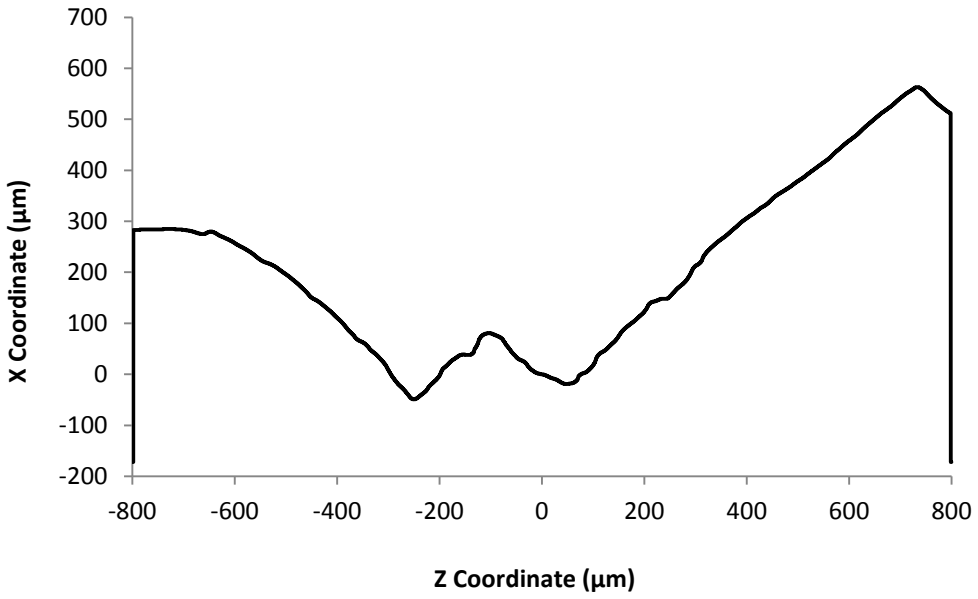

Figure 3.10: Depth Composition Profile of Fracture Surface along Z-axis (see Fig. 3.9)

The shape of the fracture surface indicates that fracture likely developed at the mid-plane ($z = 0$) of the specimen with respect to thickness, either in the interior of the bulk or at the mid-plane notch surface, propagating outward on alternating planes to create the 45° fracture surfaces observed. This pattern of fracture was generally observed in all the

specimens tested, including U1, demanding more in depth investigation to evaluate the variation in strain through the thickness of the section. In order to investigate the interior state of the specimen prior to failure, a series of finite element simulations in ABAQUS were performed.

3.3 Simulation and Model Results

The central 4 mm region of the notch tension specimen was meshed using 311,040 3D linear hexahedral elements with reduced integration (C3D8R) and 7,872 3D linear wedge elements (C3D6). The maximum element size at the periphery was 0.1 mm and the minimum element size at the notch was 25 μm, giving 64 elements through the thickness (see Fig. 3.11). The R-O material model developed in Chapter 1 was implemented, but in order to represent the Arcan shear deformation applied in the first loading stage, a predefined equivalent plastic hardening field was applied to the model simulating the pre-strain distribution for specimens S1, S2 and S3.

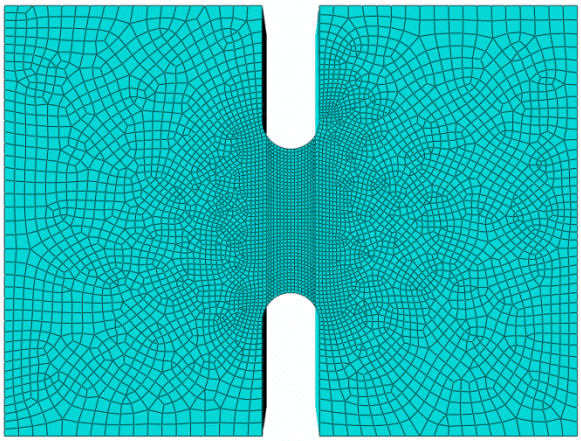

Figure 3.11: Notch Tension Mesh

A 1D pre-strain field varying along the axis of the specimen was applied to the model section by means of a Pearson VII peak shape function, which was fit to experimental Arcan strain distribution data obtained by DIC. At each desired pre-strain level, the strain distribution across the Arcan specimen was measured and utilized to manually fit the Pearson VII function given in Eq. (3.4), where ϵ_{max} is the maximum equivalent strain and x is the distance from the center of the notch.

$$\bar{\epsilon} = \epsilon_{max} \frac{w^{2m}}{\left[w^2 + \left(2^{1/m} - 1\right)(2x)^2\right]^m} \tag{3.3}$$

Fit to experimental data at selected levels of pre-strain, Eq. (3.3) generates the distributions shown in Fig. 3.12. The fit values at selected pre-strains are given in Table 3.2.

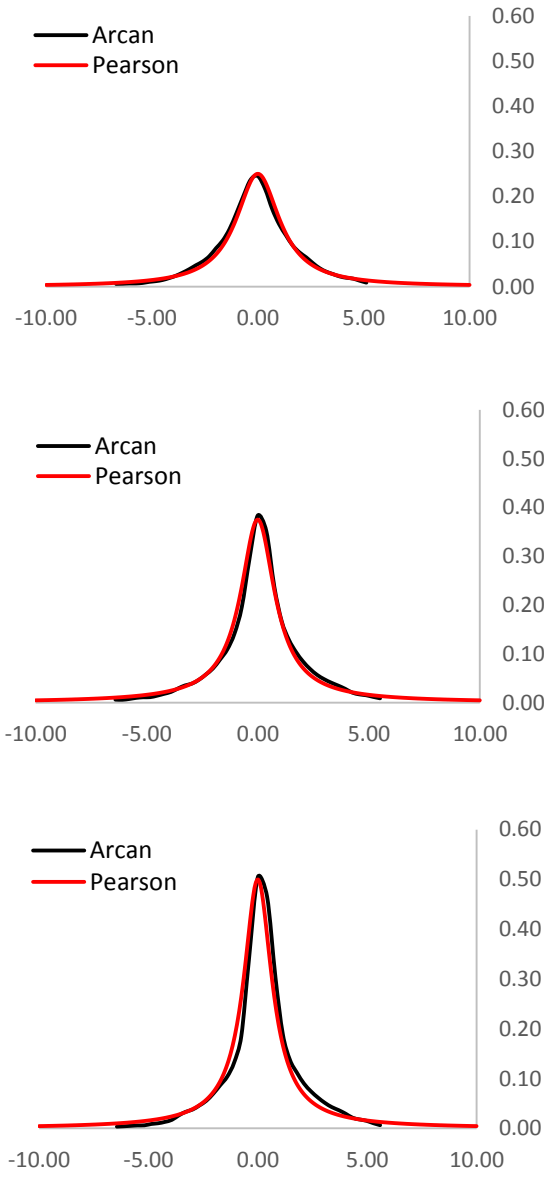

Figure 3.12: Pearson VII approximations of pre-strain distribution. The analytical peak shapes describe a 1-D distribution of plastic pre-strain along the axial dimension of the specimen. X-axis units are given in mm

Table 3.2: Peak Shape Function Fit Parameters

	S1	S2	S3
ϵ_{max}	0.25	0.375	0.5
w	2.5	1.9	1.6
m	1	0.9	0.9

When applied to the finite element model, an initial distribution of equivalent plastic strain (PEEQ) is generated across the mesh. An example of this initial field is shown in Fig.3.13 for a max pre-strain of 0.25.

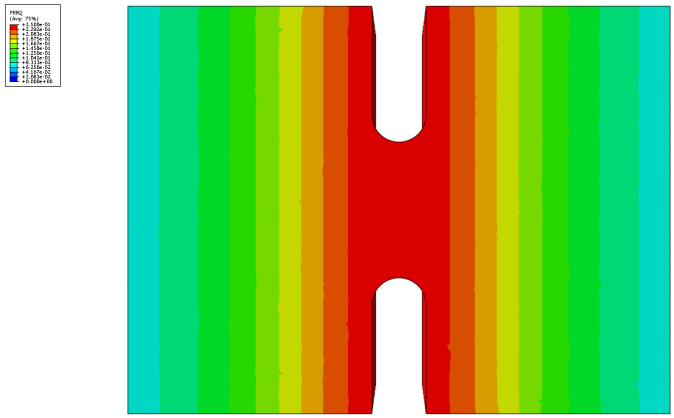

Figure 3.13: Initial Strain Distribution – S1

Simulations at pre-strain levels of 0.25, 0.375 and 0.5 were conducted, corresponding to S1, S2 and S3 respectively. Experimental surface strain measurements were used to find the stage in each simulation most nearly corresponding to the last correlated experimental

image prior to specimen failure. Once the surface simulation strains were matched to the experiment, the interior mid-plane (parallel to x-y surface plane) in the middle of the specimen thickness was viewed in order to observe the strain distribution at the center of the body. The simulation results at both the surface and mid-plane are shown in Fig. 3.14.

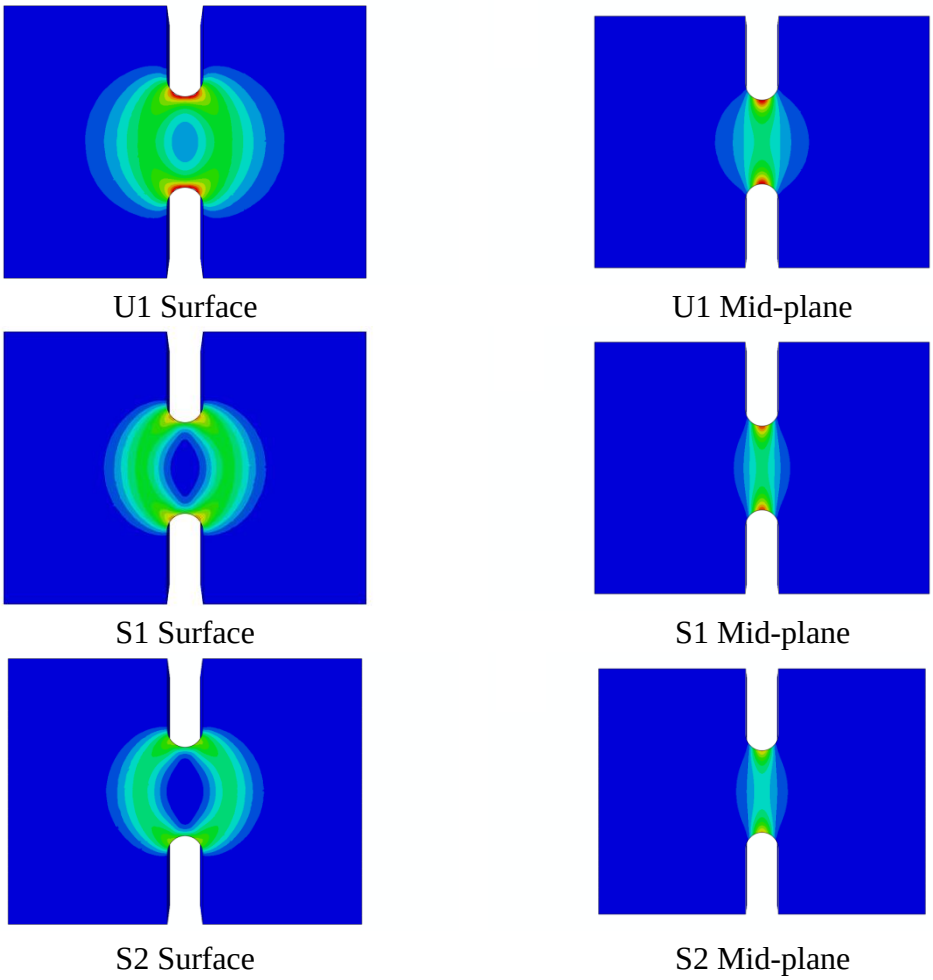

(Figure 3.14: Continued on next page)

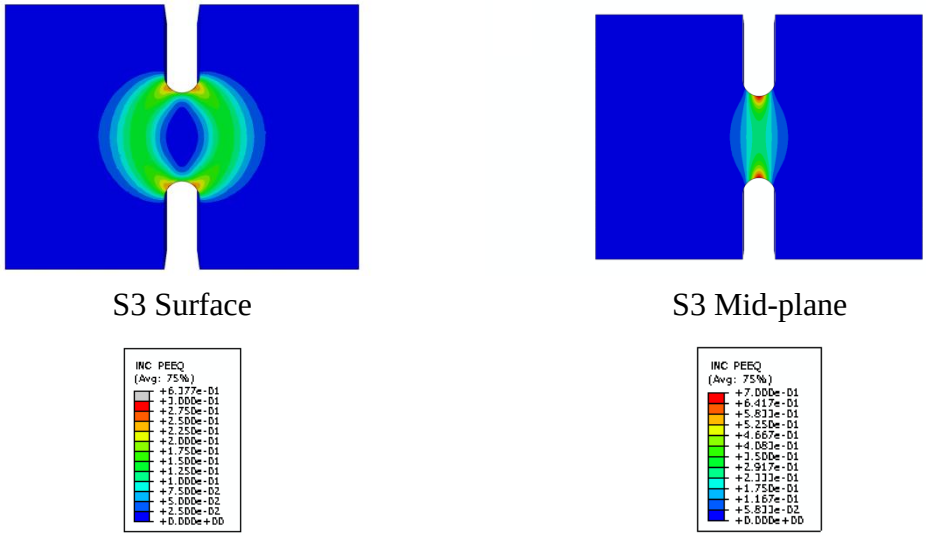

Figure 3.14: Notch Tension Simulation Results Immediately Prior to Failure

Note that in order to subtract the pre-strain field and display only the incremental plastic strain due to the notched tension loading a custom output parameter was generated. The incremental plastic strain is plotted on the undeformed mesh. Additionally, Fig. 3.15 shows a top-down sectional view of the $x - z$ plane at the interior mid-plane ($y = 0$), showing the band structure producing the arcs of plastic strain surrounding the surface of the notch (see Fig. 3.14). The bands intersect at the center of the section, where a central strain concentration at a maximum value of triaxiality is observed.

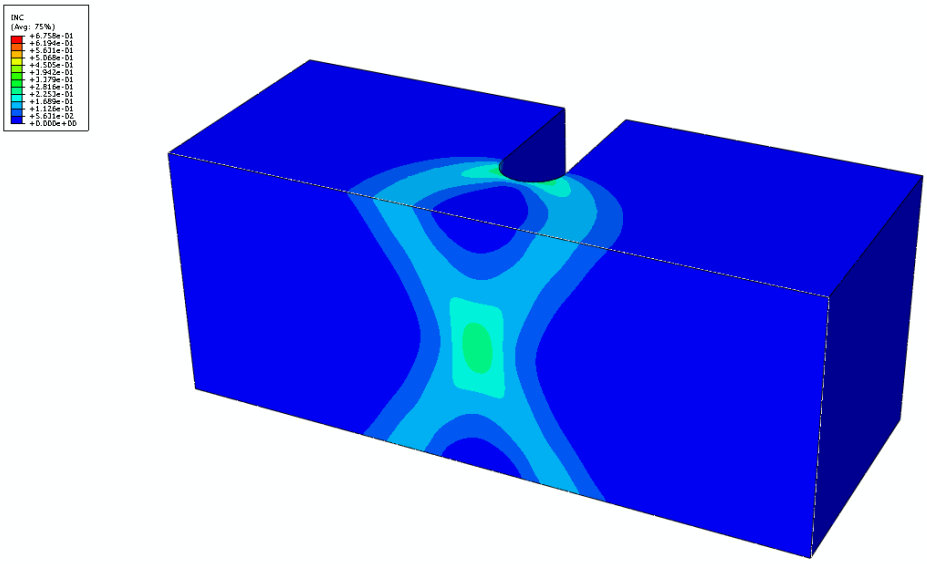

Figure 3.14: Slice View of $x - z$ Plane at $y = 0$. The X-shaped band structure allows high strain in the interior while maintaining low surface strains at the center of the notch.

The experimental surface strains are compared with the corresponding simulation surface strains in Fig. 3.16. The simulated strains at center (Point C_0) and the notch edge (Point N_0) at the interior mid-plane are given in Figure 3.17. While the failure stage in the simulation was determined by attempting to match simulation to experimental surface strain data, some variation at notch values is seen.

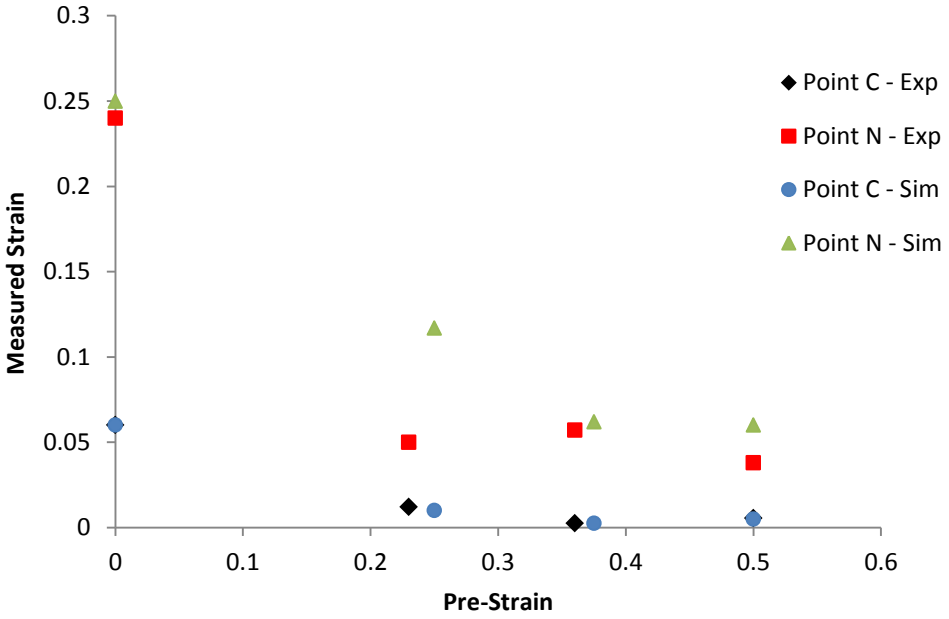

Figure 3.16: Experimental and Simulation Surface Strains

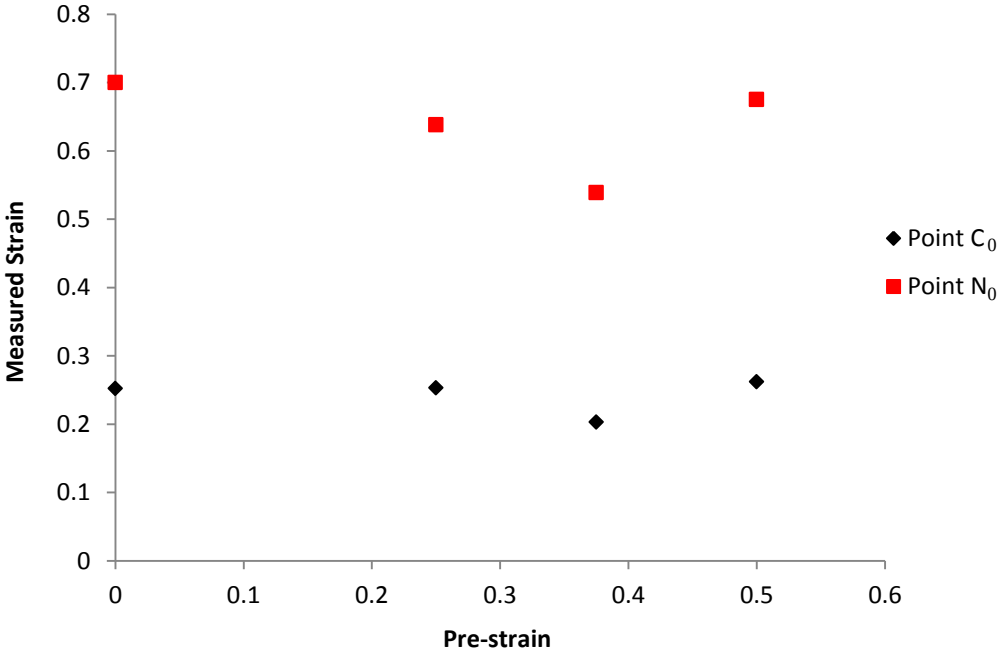

Figure 3.17: Strains at Mid-Plane Interior of Model from Simulations

Figures 3.16 shows generally good agreement between experiment and simulation for the surface strain values at the center and the notch surface, yielding confidence in the accuracy of the simulation in the interior. Figure 3.17 shows that the strains in the interior of the specimen are much higher than the surface strains observed. Strains at both point N_0 and point C_0 do not change significantly over the range of specimens, indicating that ***the pre-strain has no effect upon the strain-to-failure experienced by the material point in question***. The site of initial fracture cannot be directly determined unambiguously, but this insensitivity applies to both locations in question. All of the specimens successfully strained to values commensurate with those experienced by the virgin material, implying no material degradation by means of material damage.

Utilizing the previously calibrated Johnson-Cook material failure model for AA5083 (see Fig. 3.18), the effective theoretical damage, D_0, induced by the pre-strain, ϵ_0, (at zero triaxiality) can be evaluated. The simulation results provided the stress triaxiality, T, at point C and point N of the notch tension test, and are also given in Table 3.3. Note, that this calculation assumes the linear accumulation rule given in Eq. (3.3). The failure strains, ϵ_f, are plotted along with the model J-C failure curve in Fig. 3.18. Both sets of strain measurements fail to reach to the model curve. However, this is expected for two reasons. First, strain measurements were taken using the last available image acquired at some finite time prior to actual failure.

Table 3.3: Triaxiality and Pre-strain Damage

	ϵ_0	D_0	T	ϵ_f
Center (C_0)	0	0.00	1	0.252
	0.25	0.15	1.2	0.253
	0.375	0.22	1.2	0.203
	0.5	0.29	1.2	0.262
Notch (N_0)	0	0.00	0.5	0.7
	0.25	0.15	0.5	0.638
	0.375	0.22	0.5	0.539
	0.5	0.29	0.5	0.675

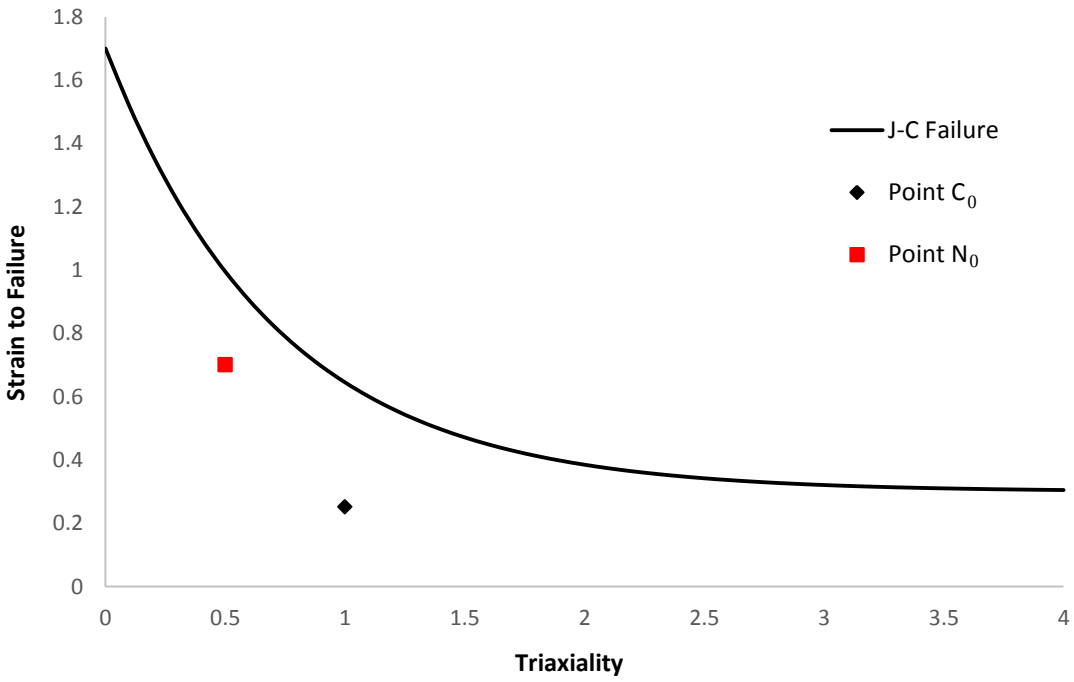

Figure 3.18: J-C Failure Curves with Zero Pre-strain Specimen Failure Strains

.Material approaching failure may strain substantially during this interval. Second, the reference J-C curve was calibrated over a grain scale gage length. The present strain calculations are accomplished at a higher gage scale, which effectively diminishes the highly localized nature of the failure strain pattern at grain or sub-grain scale. For this reason alone, the calculated values are expected to fall short of the model curve, which was generated by means of grain-scale metallographic post-mortem inspection. In addition these factors, we cannot conclusively determine the point of failure (point C or point N), so whichever point did not in reality initiate failure will display a lower than actual measured value. The measured values can therefore be considered a lower bound for the material failure curve.

The absence of material degradation requires the absence of significant damage mechanisms such as void growth under conditions of low triaxiality. Gross and Ravi-Chandar (2015) performed experiments in which a polished 6061-T6 aluminum specimen was observed in real-time via SEM under shear dominant loading. Void growth was notably absent in even highly strained areas of matrix material (see Fig. 3.19). In addition, they observed that while damage in the form of void generation and cracking did occur at sites of inclusions, the deformation and flow of the matrix material tended to inhibit the growth or even close any generated or pre-existing void spaces, preventing wide scale development of damage (see Fig. 3.20).

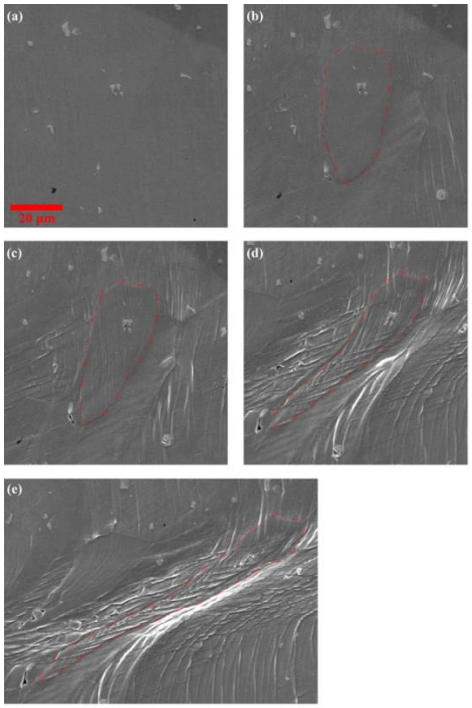

Figure 3.19: SEM Images of 6061-T6 Specimens under Shear. A Single Grain is Outlined For Reference. Even at Estimated Strains of 1.2 (d) and 2.2 (e), no void growth or damage is visible (Gross and Ravi-Chandar, 2015)

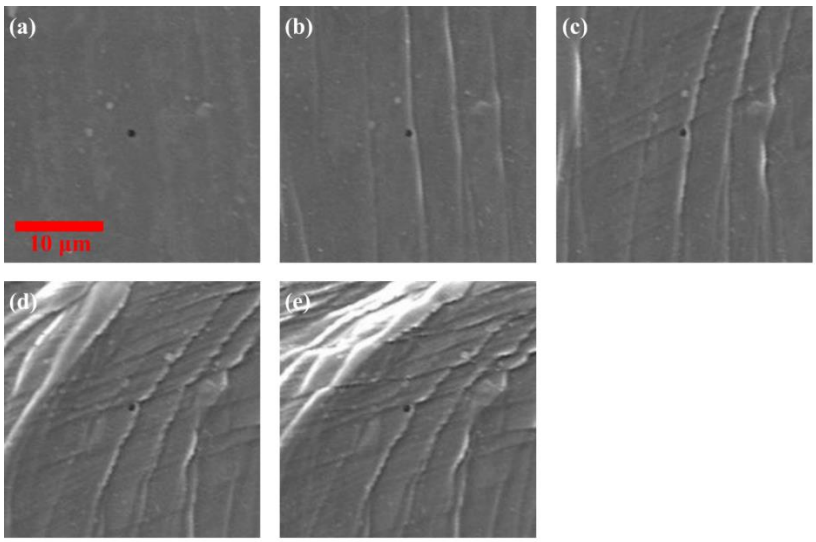

Figure 3.20: SEM Images of Pre-existing Void under Shear. Up to plastic strains of 0.87(e), the void experiences no change in size (Gross and Ravi-Chandar, 2015).

These observations yield evidence to support the notched tension results, suggesting that negligible damage evolution occurs for most of the strain lifetime of the material at low triaxiality.

In the case of the experiments performed in this work, the uncertainty associated with the conditions under which the specimen strain to failure was measured requires and justifies the retention of the grain-based J-C failure locus as the material failure model of choice for this work. However, this is no way impacts the previous conclusion as to the insensitivity of material failure strain to the pre-strain field, and associated damage criterion. The insensitivity of the failure strain to previous straining at low triaxiality suggests the absence of material degradation by means of damage accumulation at these loading conditions. The absence of cumulative material damage can effectively be modeled using an uncoupled failure model in which material performance remains unaffected until failure strain is reached, upon which time the material is degraded totally and instantaneously. The remainder of this work will employ an uncoupled strain-to-failure model, utilizing the grain based Johnson-Cook failure locus previously discussed.

Chapter 4: Ballistic Impact on Thin Plates

In order to evaluate the potential of a material to perform a protective role as armor or a component of an armor system, the response of the material and structure to ballistic impact must be evaluated. The study of projectile impact, penetration and perforation (complete penetration of a target and passage of the projectile through the target) has been a subject of intense interest for more than a century. For most of its history, studies of impact and penetration have been largely empirical in nature, observing general trends and correlations between projectile and target initial conditions and response. While certain empirical relations may still be used today, the large number of constraints necessary to maintain accuracy limits their usefulness and predictive capability, especially under conditions which see transitions between regimes of response in the target and mechanisms of deformation and failure in the material (Corbett, 1995). The quantitative engineering analysis of penetration and perforation, however, really began in earnest during WWII. From an analytical standpoint, projectile penetration and perforation was still almost entirely unexplored and unattempted due to the mechanical complexity of the problem. Therefore, the defense industry had little ability for predictive design and analysis of protective systems and munitions for armor penetration. The challenges associated with this problem drew some prominent names in the scientific community. Later in the war, Clarence Zener (of the eponymous Zener diode) would work on the projectile impact for the army (Watertown Arsenal), but the first serious analysis of penetration and perforation was attempted in 1941 by physicist Hans Bethe

(who would soon after become the director of the famous T division at Los Alamos during the Manhattan Project), statically analyzing the penetration of metallic plate by a cylindrical projectile (Bethe, 1941). The potential value of a model of projectile perforation was not lost on the military, and his completed work was immediately classified, making it unavailable to Bethe who was not yet an American citizen. Taylor (1948) expanded upon this work, improving Bethe's analysis of hole expansion to account for incremental variation. This work, along with the earlier work of Bishop, Hill and Mott (1945) on quasi-static indentation in metals by cylindrical punches established the basis for the analysis of hole expansion as the fundamental process in projectile perforation problems.

During this period of time the study of ballistic impact was concerned almost entirely on munition/armor design, and so focused upon the velocity ranges experienced by military ordnance, approximately 500-1300 m/s, and the mechanisms dominating this regime. However, as the space race intensified, focus generally shifted from ordnance and sub-ordnance velocities to hypervelocity impact regimes seen during meteorite or meteoroid impact. The Hypervelocity Impact Symposia of 1955-1969 spurred significant study in the area, seeing the development of cavity expansion theories (CET) and the application of those theories to penetration problems. Hopkins (1960) developed a dynamic theory of cavity expansion in metals and Goodier (1965) applied dynamic cavity expansion to the problem of projectile penetration. Cavity expansion theory would go on to form the basis of many analysis methods concerned with the penetration of tapered projectiles, and would eventually be modified by Forrestal et al. (1987) in the late 1980's

for use in subsequent analyses in materials from ductile metals to soil and concrete. However, CET is inherently limited to cases where the primary mechanism of failure during perforation is the projectile induced growth of an initial impact indentation (or hole) to a size allowing passage of the projectile. Experimental studies have shown that this single mechanism only dominates impact events at velocities high above the minimum perforation velocity, or ballistic limit, with very tapered or sharp projectiles impacting intermediate thickness plates. CET was not the only analytical method developed during this period. Recht and Ipson (1963) developed an analytical model for the perforation of thin plates by blunt projectiles, in which case shear dominated plugging failure was the primary failure mechanism. Recht and Ipson utilized energy and momentum balance to develop an expression for the residual velocity of a perforating projectile assuming plugging failure. However, the expression depended upon an empirically determined ballistic limit and neglected all other mechanisms of deformation but the plugging behavior. The result of these constraints is that like CET, the model is accurate only at velocities significantly higher than the ballistic limit (in thin plates). Of course, where armor is concerned the ballistic limit is the quantity of primary interest. A model capable of predictive armor design must be capable of representing the full behavior of the target projectile system in this regime.

Beginning in the 1970's, focus began to shift again to capturing the multiple mechanisms of deformation and failure seen around the ballistic limit of the system (see Fig. 4.0).

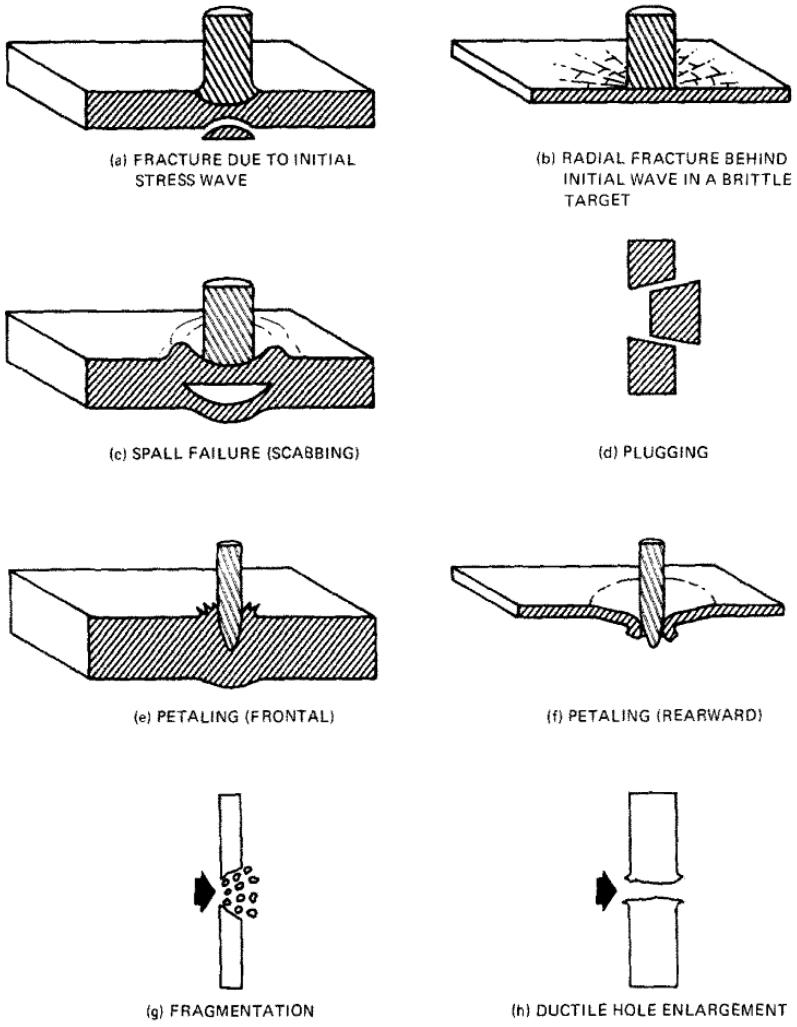

Figure 4.0: Common Perforation Mechanisms (Backman and Goldsmith, 1978)

Goldsmith and Finnegan (1971) and Calder and Goldsmith (1971) conducted experiments in thin plates at velocities around the ballistic limit, revealing several interesting results. They found that the maximum amount of global plastic deformation of the plate (dishing) occurred at the ballistic limit while the maximum velocity drop over the course of a

successful perforation occurred at a velocity slightly higher than the limit. In addition, for a round-nose projectile they found an inverse relationship between plug size and impact velocity.

Experimental studies such as these found that around the ballistic limit, not only did significant plastic structural deformation occur, but multiple mechanisms of strain localization and failure occurred in combination such that a single mechanism analysis could not capture the perforation of a projectile near the limit. At sufficiently high velocity, only the presence of negligible deformation outside a primary perforation mechanism allowed presupposed models such as CET and Recht and Ipson (1963) to function well. Levy and Goldsmith (1984) conducted experiments in which a multiple mechanism perforation process was captured using high speed photography. They also formulated an analytical model of the penetration processes utilizing a presupposed shape of plate deformation (as measured by experiment) and projectile velocity function. While capable of accurately predicting central plate deflection for impacts below the ballistic limit, the model failed to predict the residual projectile velocity after a successful perforation, indicating the fundamental limitation of analytical methods with respect to the perforation problem. Near the ballistic limit, the additive behavior of global deformation and localized failure by multiple competing mechanisms cannot be captured by an analytical model which must place too many constraints on the problem.

In order to capture the full behavior of this complicated problem, a method capable of modeling all the above phenomena utilizing a more complicated material model must be implemented. While early suspicion of such techniques may have slowed adoption, it was

eventually recognized that numerical methods capable of approximating full continuum mechanics offered the best chance of success. Wilkins (1978) conducted early numerical simulations of projectile impact utilizing a 2D finite difference method. While simple by modern computational standards, Wilkins successfully observed multiple mechanisms of failure and deformation including dishing, plugging and hole enlargement over a range of target thicknesses, material models and projectile geometries; and identified several fundamental factors affecting the ability of a deformable projectile to perforate a target or a target to defeat a projectile. The ability of numerical methods such as finite difference or finite element to handle complicated material models and loadings have made them the method of choice for modeling many ballistic impact problems.

Borvik et al. (2001), building upon previous numerical work, successfully demonstrated the ability of finite element simulation to capture experimental behavior when utilizing a properly calibrated material. Utilizing both a modified Johnson-Cook plasticity and failure model calibrated from experiments on Weldox 460 E steel, they demonstrated the ability of a standard plasticity model in conjunction with a triaxiality based failure model to generate an accurate plugging and deformation response upon impact by a blunt projectile.

Expanding upon this work, Borvik et. al. (2004, 2009) compared this finite element model to results predicted by CET for AA5083-H116, the candidate aluminum alloy. Specifically, they compared predicted results for impact by a 20 mm diameter conical projectile upon aluminum plates 15-30 mm thick at 200-400 m/s. Under such conditions, the target primarily experienced perforation by ductile hole enlargement,

allowing the CET based perforation model of Forrestal to be used for analysis and comparison. Borvik et al. (2004) conducted finite element simulations of the experiment utilizing a previously calibrated Johnson-Cook plasticity model. While their 2001 work utilized Johsnon-Cook failure in addition to plasticity, these simulations utilized no failure or fracture condition. Rather, a pinhole was introduced in the target mesh simulating an initial cavity or indentation; allowing full perforation to occur only by plastic enlargement and flow. The use of this configuration allowed close simulation of the ductile hole enlargement mechanism without requiring material or element failure. While successful in closely modeling the experimental result and demonstrating the capability of finite element simulation to match the accuracy of tested analytical methods, the absence of an incorporated material failure model renders this simulation scheme incomplete and once again applicable to only a very specific set of impact conditions.

In contrast the above work, Lee and Wierzbicki (2005) investigated the failure of impulsively loaded thin plates. Lee and Wierzbicki utilized a shell-element based finite element model to investigate the failure of very thin plates loaded impulsively. A Bao-Wierzbicki fracture model (2004) was implemented in order to allow failure by multiple mechanisms. Discing, and petalling were observed as a result, rendering the perforation of the plate dependent upon multiple failure mechanisms in addition to target deformation itself. However, the treatment of the plate as a single uniform element through the thickness demands that failure occurs through the thickness of the plate simultaneously, eliminating the possibility of shear plugging failure to occur as has been documented above. The following experimental and modeling work expands the previous studies to

plates of finite thickness under ballistic impact conditions which demand the multiple mechanisms of deformation and failure including both radial petalling fracture and shear plugging through the thickness of the plate.

4.1 Experimental Setup

The target specimens were machined from the same 0.063” thick AA5083-H116 aluminum plate utilized in the tests described in the previous chapters (Fig 4.1).

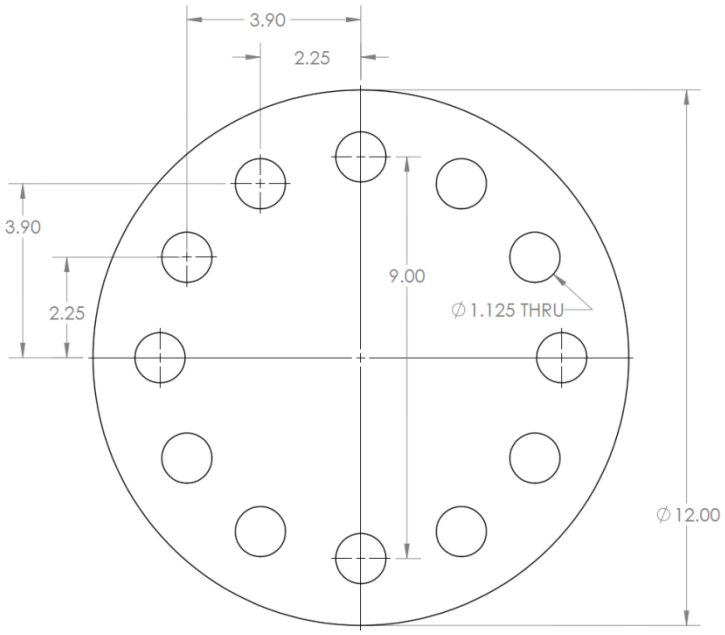

Figure 4.1: Impact Target Specimen—Dimensions in Inches

The target plates were clamped and bolted around the outer edge by a heavy steel fixture, leaving a 6 inch central circular region of the plate (with a clamped boundary) free to deform under impact. The fixture itself was clamped to an I-beam, serving as a mount rail for the apparatus seen in Fig. 4.2. A compressed air gun was used to deliver the impacting projectile to the back of the target plate. The radial center of the target fixture was aligned with the bore axis of the gun to ensure a symmetric impact location with respect to the plate boundary.

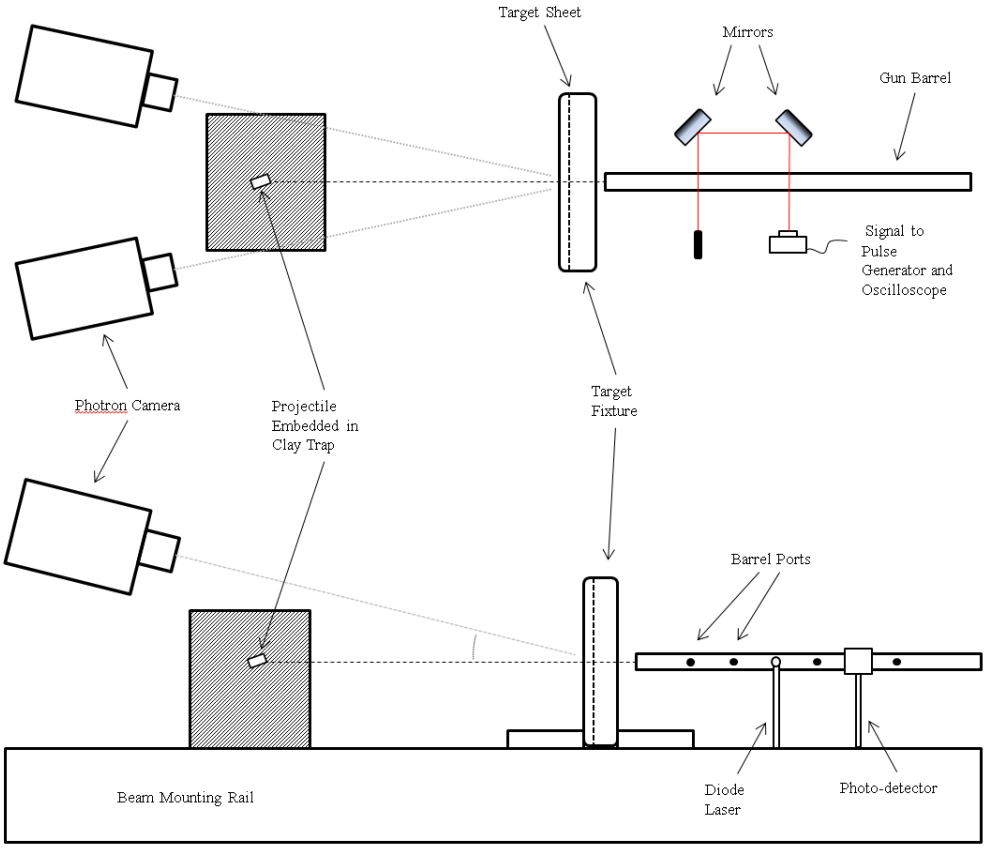

Figure 4.2: Experimental Impact Apparatus—Top and Side View

A clay trap was placed on the opposite (front) side of the target fixture to catch the perforating projectile. The last 12 inches of the 8 foot, 0.5 inch diameter gun barrel was ported, permitting the installation of a break-beam style chronograph for the measurement of the incident projectile velocity prior to impact. A diode laser beam was directed through a barrel port and reflected, via two optical mirrors, back through the adjacent port into a photo-detector. The signal from the laser photo-detector was connected to the trigger channel of a Berkeley Nucleonics pulse generator, sending a TTL pulse to a digital phosphor oscilloscope each time the beam was broken, allowing the calculation of the velocity of a projectile traveling down the barrel. Note, the pulse generator was used in this instant to provide a clean TTL pulse at a preset trigger level of photo-detector signal decay. In this way, the oscilloscope impedance did not negatively affect the system response (and time constant) of the photo-detector.

The pulse generator was also used to trigger (upon passage of the projectile through the beam) two synchronized Photron SA1.1 high speed cameras viewing the front surface of the target plate. These cameras were placed approximately 10° to the left and right of the bore axis and 14° above the bore axis, viewing the target plate over the front edge of the projectile trap. Nikon 24-85 mm lenses were used in conjunction with the detector settings of cameras to view a section of the target plate ranging from a central 1 inch square to the full unclamped plate surface. The stereoscopic configuration of the synchronized cameras allowed the use of 3D digital image correlation (provided by ARAMIS) on the collected surface images of the plate during the process of penetration and perforation. To utilize the DIC capability of this apparatus, the aluminum target

plates were painted with an appropriate black and white speckle pattern. Illumination for the tests was provided by four high intensity halogen lamps arranged around the target fixture. The frame rate dictates the maximum resolution achievable by the camera system so that tests utilizing the higher frame rates were limited in view to the very central region of the plate around the perforation created by the projectile.

4.2 Experimental Results

A series of impact tests (shown in Table 4.1) were conducted at low velocities near the ballistic limit of the target plates, ranging from approximately 73-156 m/s.

Table 4.1: Impact Tests on AA5083-H116 Aluminum Target Plates

Plate #	Incident Velocity (m/s)	Residual Velocity (m/s)	Kinetic Energy Retention	# of Petals	Plug Diameter (mm)	Frame Rate (kps)	Notes
1	73	NA	NA	6	4.7	30	No perforation
2	96	54	32 %	8	--	50	
3	104	65	39 %	10	--	50	
4	100	85	72 %	NA	12.5	100	Blunt-nose projectile
5	156	147	89 %	11	5.1	100	

For the tests analyzed here, a hardened O1 tool steel projectile was used. The 24.7 g projectile was ~0.5” in at the base, tapering to approximately 0.25” diameter round nose with a taper angle of 12° (see Fig. 4.3).

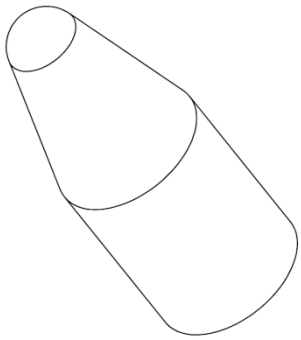

Figure 4.3: Tapered Round Nose Projectile

Synchronized images of the test were collected using by high speed camera at the frame rates given above. A selection of experimental high speed images for Plate 1 and Plate 5 are shown in Fig. 4.4 and Fig. 4.5 respectively.

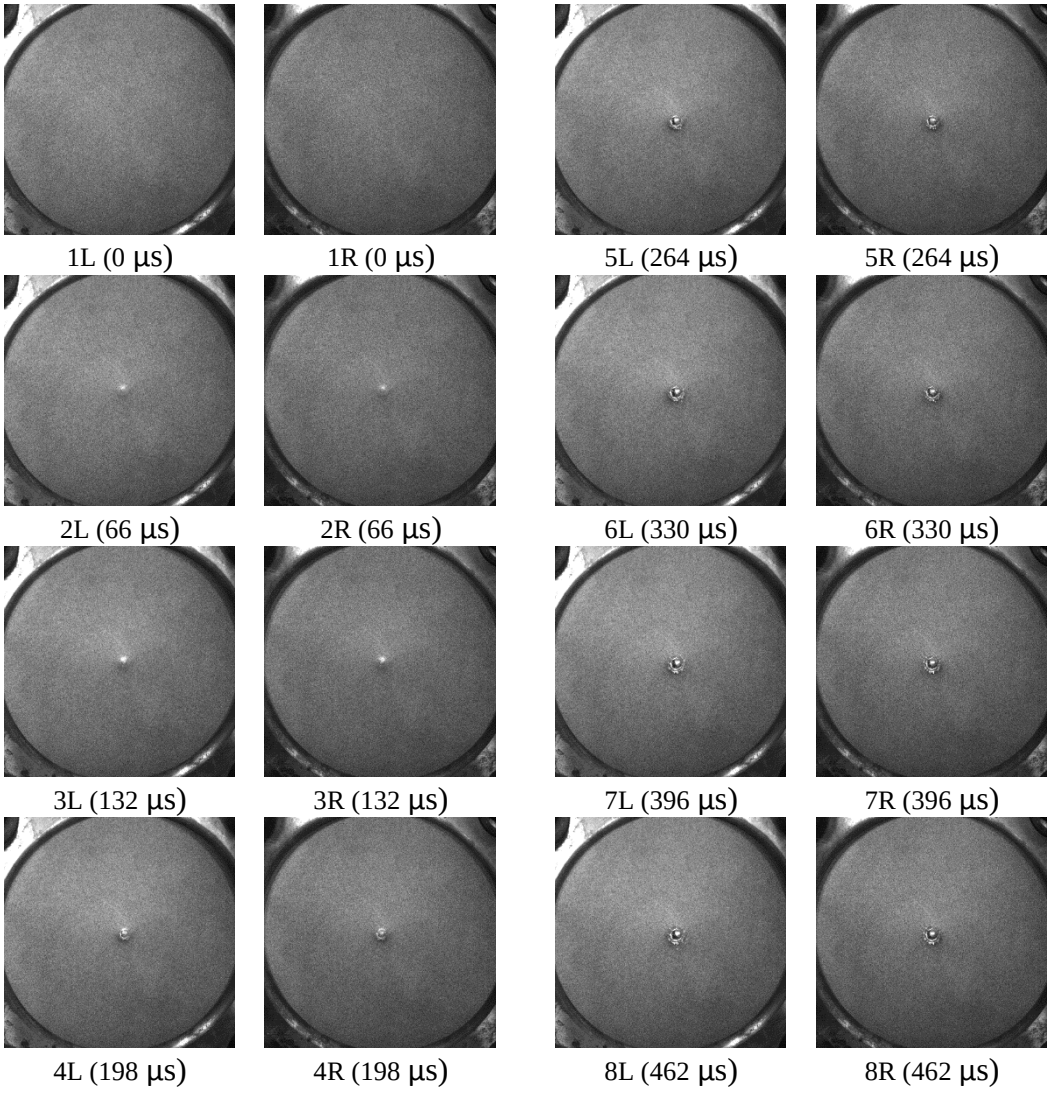

Figure 4.4: Plate 1 – 73 m/s

As noted above, Plate 1 was not successfully perforated but experienced partial plug formation and radial cracking necessary for the full scale development of petalling. For a better view of these phenomena see the post-mortem photos of Plate 1 given in Fig. 4.7.

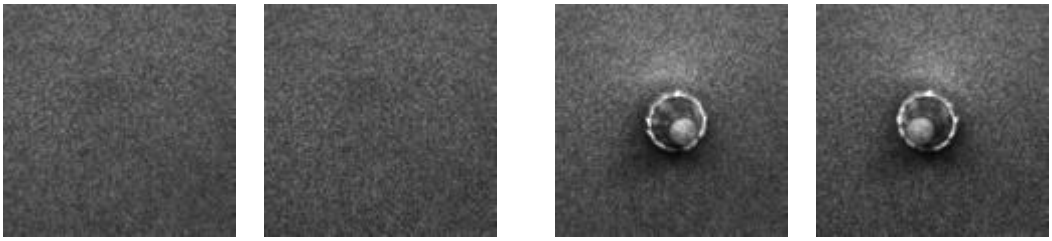

1L (0 μs) 1R (0 μs) 7L (120 μs) 7R (120 μs)

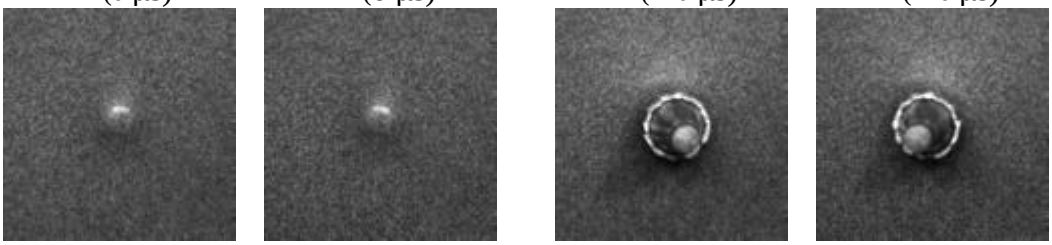

2L (20 μs) 2R (20 μs) 8L (140 μs) 8R (140 μs)

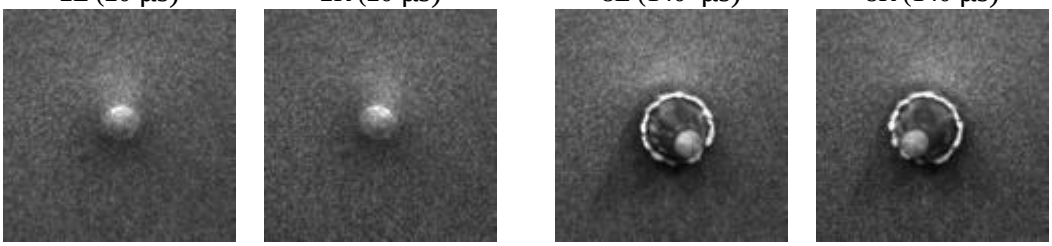

3L (40 μs) 3R (40 μs) 9L (160 μs) 9R (160 μs)

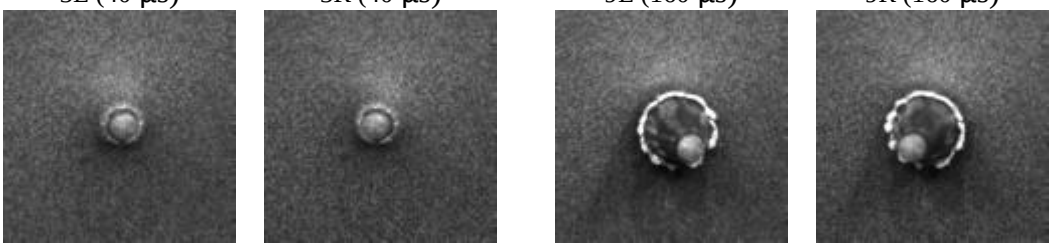

4L (60 μs) 4R (60 μs) 10L (180 μs) 10R (180 μs)

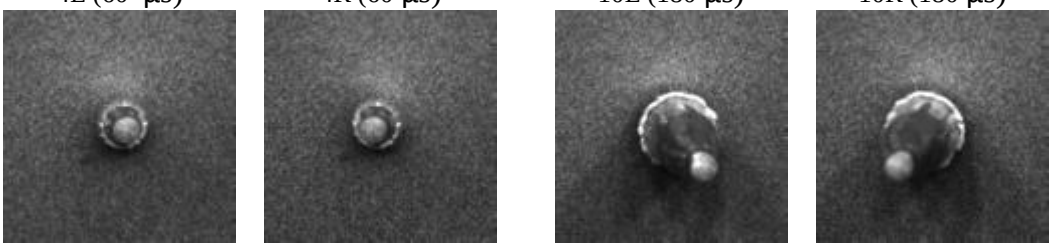

5L (80 μs) 5R (80 μs) 11L (280 μs) 11R (280 μs)

(Figure 4.5: Continued next page)

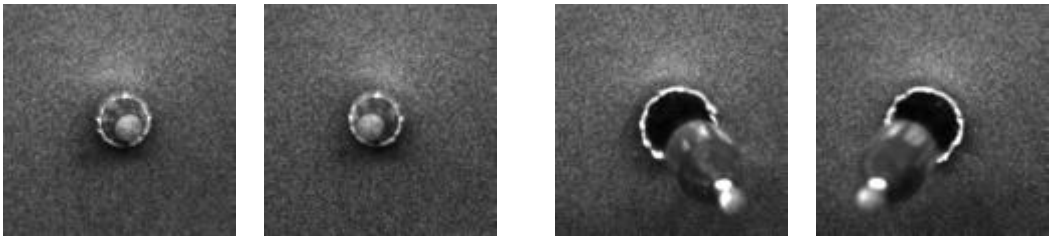

6L (100 μs) 6R (100 μs) 12L (480 μs) 12R (480 μs)

Figure 4.5: Plate 5 – 156 m/s

The highest velocity test (Plate 5), however, shows full perforation and petal development by the tapered projectile. To take advantage of a higher frame rate (100,000 fps), only a limited central region of the camera detector was utilized, providing a reduced resolution image

In Fig. 4.5, the basic mechanisms of plate failure considered in this work can be observed. Plug development can be observed in images 3L and 3R. By 4L, 4R full separation of the plug has occurred and the nucleation of petals by means of localization and radial fracture around the circumference of the new plug fracture surface has begun. As the projectile continues to penetrate, the passage of the tapered section drives the propagation of the radial petal cracks, growing the petals until the shoulder of the projectile is reached at approximately image 10L and 10R. At this point, there is only minor frictional resistance applied to the projectile. Note that in image 12L and 12R, the detached plug has visibly separated from the nose of the projectile as the petalling process decelerates the projectile.

In contrast to the combined plugging and petalling process shown above, Fig. 4.6 shows the results of an impact by a blunt cylindrical projectile (the impactor shown is simply the previously described projectile fired backwards).

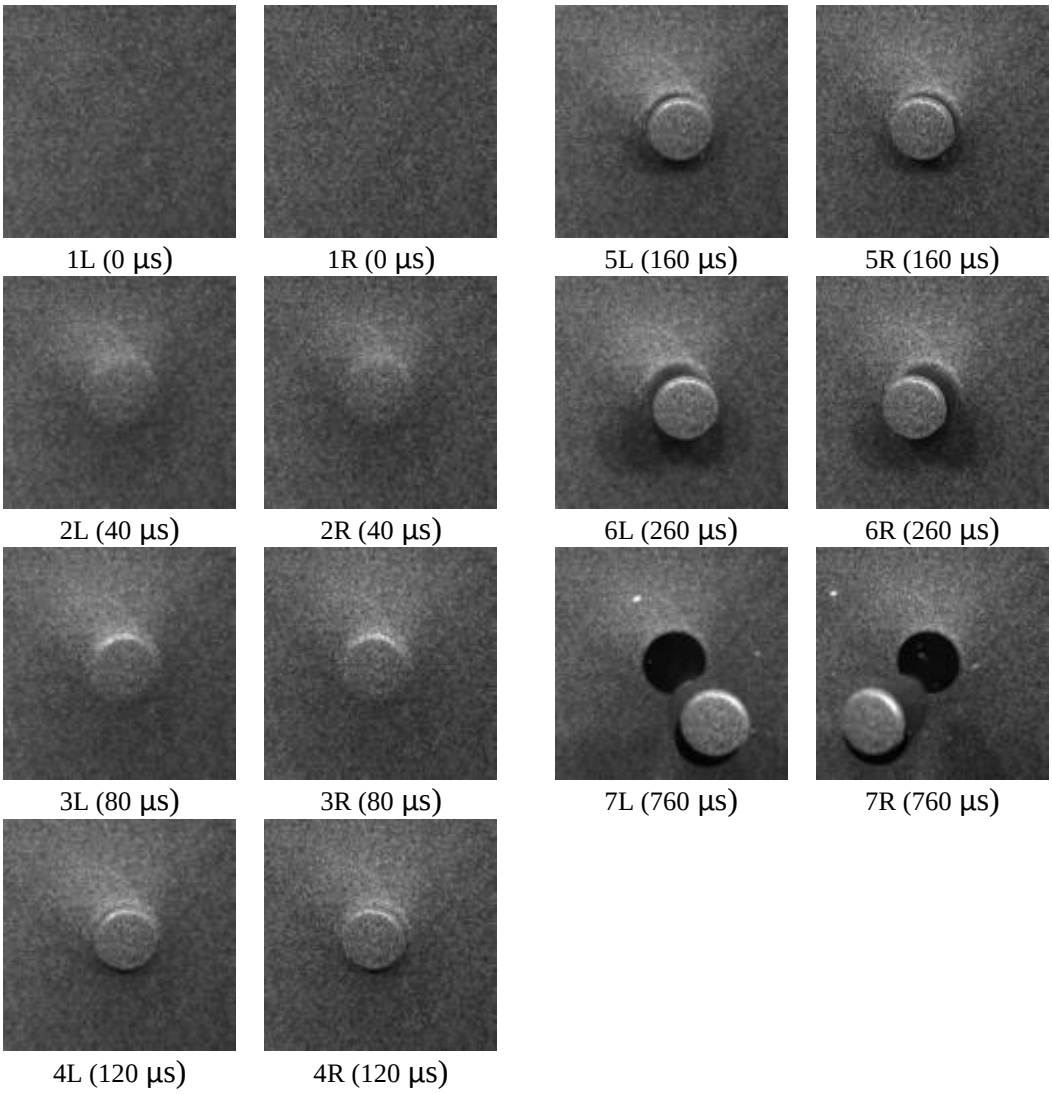

Figure 4.6: Plate 4 – 100 m/s with Blunt Projectile

The blunt nose projectile very cleanly shears a plug from the target plate approximately the size of the projectile face itself. There is relatively little permanent plate deformation outside of the sheared region, which ultimately allows easier perforation of the target plate by the blunt projectile than the tapered projectile. As shown in Table 4.1, the residual velocity (at an incident velocity around 100 m/s) is much higher for the blunt projectile than the tapered round nose projectile. The blunt impactor retains much more kinetic energy post-perforation, indicating that the energy consumed by the combined effect of deformation and fracture is less under the conditions created by the blunt projectile. This result matches previous experimental studies on thin plates impacted by both conical/ogive and blunt nose projectiles. Note, that the residual velocity was estimated by measuring the time required for the projectile to exit the frame and consequently travel the fixed axial distance from the target plane to the edge of the camera frame.

The camera orientation seen in the above images was implemented in order to perform 3D digital image correlation (DIC) on the collected high speed images. DIC was performed on test specimens using ARAMIS and the cameras were externally calibrated accordingly prior to each set of test conditions. Target specimens were painted with an appropriate black and white speckle pattern in order to facilitate the DIC analysis. This technique was successfully used to measure the initial deformation of several thin sheets impacted by hemispherical round-nose projectile during shakedown tests. The combination of very thin target material and the larger constant radius spherical nose projectile provided a condition where the target could experience significant distributed

strain across the nose of the projectile during conformal out-of-plane deformation of the target. The spherical projectile nose offers the gentlest geometrical transition from projectile nose to shoulder, helping to avoid early localizations and minimize sharp surface rotation during the deformation process. Under these conditions, DIC was able to very successfully capture the deformed profile of the sheet up to the point of discing failure—a failure mechanism commonly seen in very thin targets generating a plug-like circumferential crack by means of thinning and tensile tearing. However, the usefulness of this technique was found to be severely limited by both practical aspects of the experimental setup and the fundamental behavior of the specimen under the actual test conditions required. Figure 4.7 shows an example of the analyzed results of the Plate 2 test. In this test, a rectangular region across the width of the specimen was captured and analyzed. The results shown are raw in the sense that no interpolation or data fill has been performed; only the immediate results of the best achieved correlation are shown.

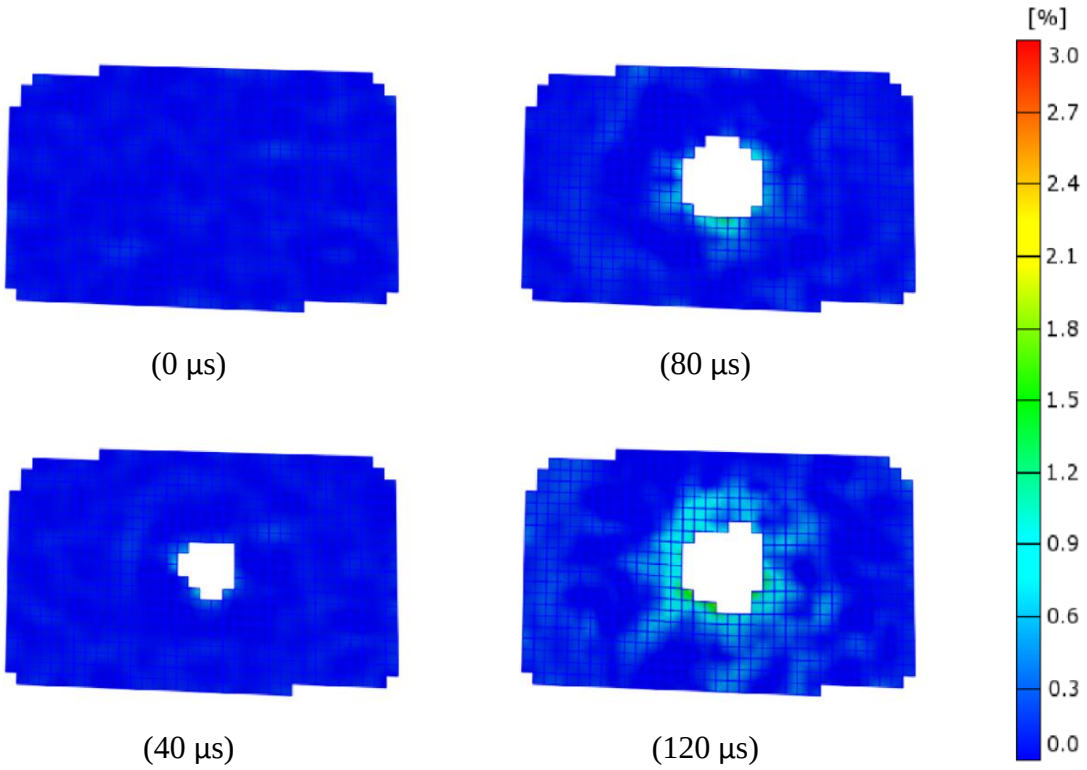

Figure 4.7: DIC Results of Plate 2 Images. The center white area indicates the region where DIC has failed.

While correlation throughout the process of perforation can be maintained in the far field of the plate where dishing and plastic bending occur, the regions of interest for this project lose correlation as the projectile penetrates. The significant local out of plane displacement combined with the surface rotations seen around the sharper nose of the projectile contribute to the loss of correlation and certainly accuracy in most cases before the full perforation of the projectile nose. In the circumferential region around the projectile nose--the transition region that will eventually fail, generating the plug—significant localized surface strains are seen, distorting and destroying the speckle pattern locally. Additionally, the varying curvature generated by the projectile nose in this region

causes annular surface reflections that throw off the correlation. While the surface of the painted target is generally non-reflective, the strain in the aforementioned region along with the surface rotation of material in that region combine to redirect the high intensity concentrated-source lighting necessary for high speed photography into the cameras at certain points during the test, creating hot-spots in the associated images.

Outside of the plug, the region that experiences petalling displays similar issues. As the ultimate failure of the plate occurs within these rotated regions, the primary quantities of interest are somewhat out of reach of this method as implemented. What can be measured—the regions of plate away from the location of perforation—experiences only dishing and relatively minor plastic deformation. The deformation of plates prior to perforation has been studied extensively and can be modeled accurately using both numerical and analytical approaches, and is not the primary concern of this work.

Apart from these fundamental issues, the practical limitations of the apparatus and the utilized equipment present additional complications affecting the DIC analysis. Photron SA1.1 high-speed cameras were used for the experiment. While capable of capturing full 1024x1024 pixel images, the resolution available for capture at 100,000 fps is limited to 192x192 pixel images. Therefore, one must consider the tradeoff between spatial resolution and temporal resolution during the test. In order to capture higher speed impact events with sufficient time resolution, substantial sacrifice in image resolution may be required, which may compromise the ability to resolve and capture localized deformations. A narrow depth of field may be generated by the use of necessarily large aperture settings while using high speed photography. Considering the significant out of

plane displacements associated with plate impact, a narrow depth of field may further compromise the analysis. In this case, enough light intensity was achieved to afford an f-stop setting high enough to give sufficient depth of field. However, the lighting available operated on AC power, displaying some amount of observable flicker, which may negatively impact the intensity measurement performed by the correlation process. All of these factors limited the usefulness of high-speed DIC as a mechanism of analysis and measurement for the experiment given. The problems associated with the DIC analysis data at the boundary of the perforating region renders the available information to noisy and incomplete to yield useful information to this project. For these reasons, DIC analysis of the captured high-speed images will not be considered further and the remaining experimental and simulation analysis given in this chapter will be largely limited to post-mortem analysis and data.

Post-mortem images of the plate specimens are given in Fig. 4.8. Petalling or incipient petal fractures can be seen in all impacts by tapered projectiles (see Table 4.1). In the case of the lower velocity specimens, the plug is still attached to a petal indicating the incomplete circumferential failure of the shear zone prior to radial localization and petalling fracture. The stresses at the plug are relieved as petals form, converting the connected material to what is essentially a plastic beam with a hinge point at the base of the petal. Continuing perforation by the projectile drives the propagation of radial cracks by applying bending forces to the petal itself. This mechanism increases the compliance of the petal with increasing projectile perforation until the hole is large enough to allow the unencumbered passage of the cylindrical part of the projectile.

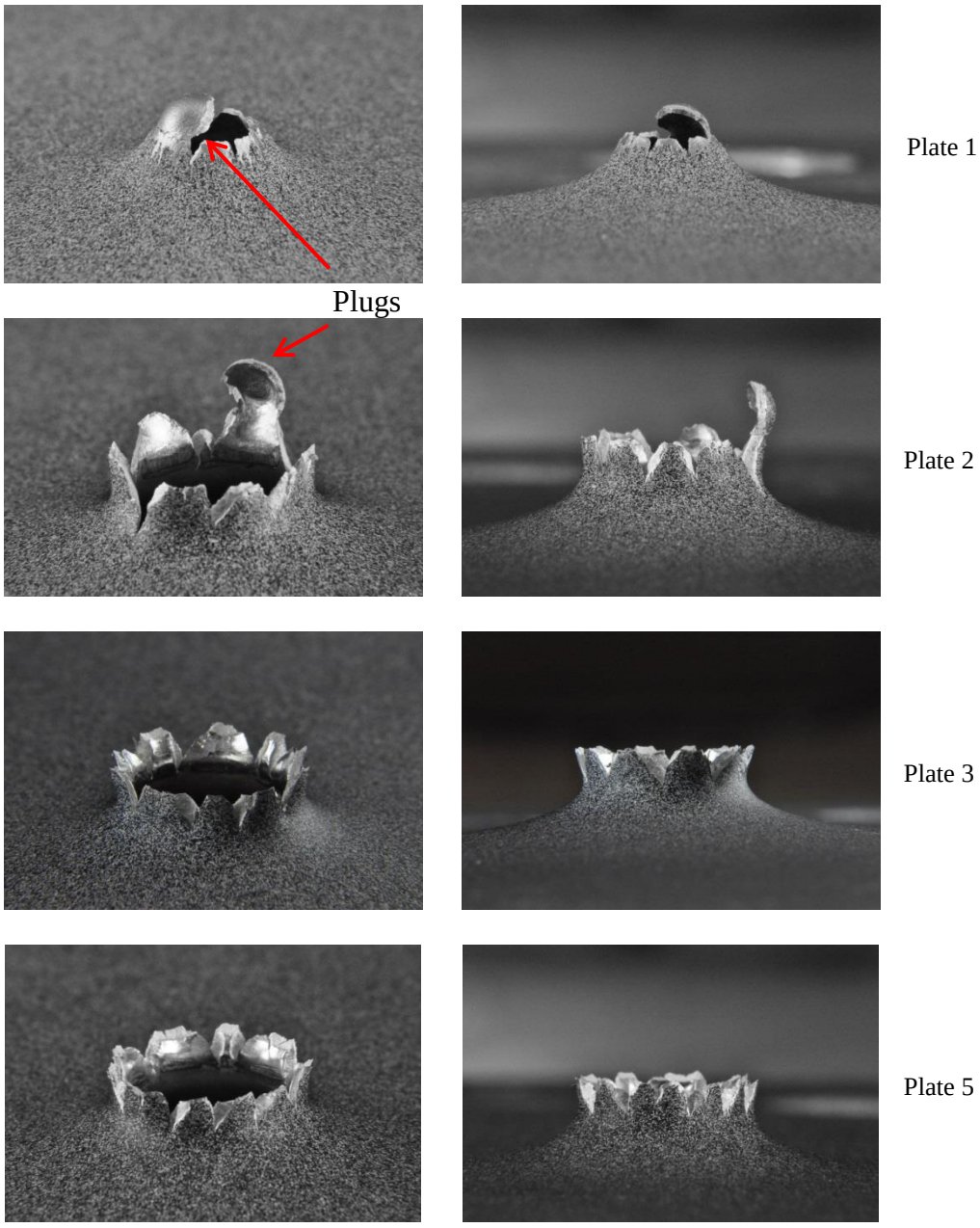

Figure 4.8: Post-Mortem Images of Plate Impacts

Figure 4.8 also shows a distinctive bend-back of the petals as the curve beyond perpendicular to the plane of the plate. This curvature is due to the initial dishing of the plate prior to petalling. As radial cracking begins and petals form, the contact point between the projectile and the petal moves toward the base of the petal and the preexisting out-of-plane curvature of the petal beyond this point of contact bends the petal slightly away from the projectile surface.

By the time this contact point reaches the shoulder of the projectile, the full petal is bent back beyond the surface of the projectile, creating the post-mortem geometry seen here. While some fractures may be difficult to see in the images above, the number of radial fractures (and therefore incipient or developed petals) can be seen to increase from Plate 1 to Plate 5 (see Table 4.1). The petalling fractures themselves show distinct slant character, suggesting the dominance of a sheet or through-thickness localization mode at the site of radial crack development. No clear pattern between the relative directions of adjacent slant fractures was observed—adjacent fractures may be oriented parallel or opposite to each other without any discernible pattern. Additionally, more extensive dishing at increased radial distance from the axis can be observed in the lower velocity tests. This is expected as previous experimental studies in thin plates have shown maximum center-point out of plane displacement to occur around the ballistic limit; increased perforation velocity reduces the radius of material that experiences the propagating dishing stresses generated by the impact prior to full perforation of the target.

The central region of the target initially impacted by the projectile (in the case of Plates 3,4,5) becomes the plug and is removed from the target completely given sufficient

impact velocity. The plugs for the analyzed test were recovered for post-mortem analysis. Plug 5 was sectioned along a meridional plane along the r-axis of the target plate for analysis by optical microscope and SEM (see Fig. 4.9). The plug in Fig. 4.9 is oriented so that the labeled z-axis is in the direction of projectile motion (along the axis of the target plate).

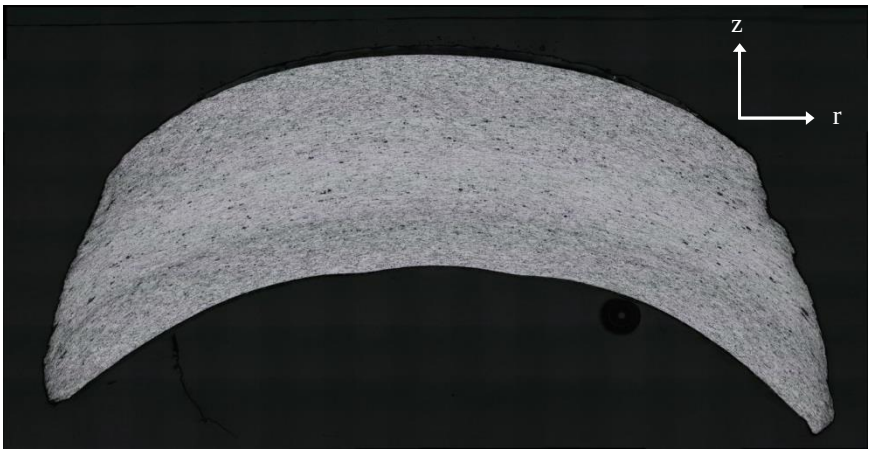

(a) Optical Micrograph of Plug 5 Cross-section

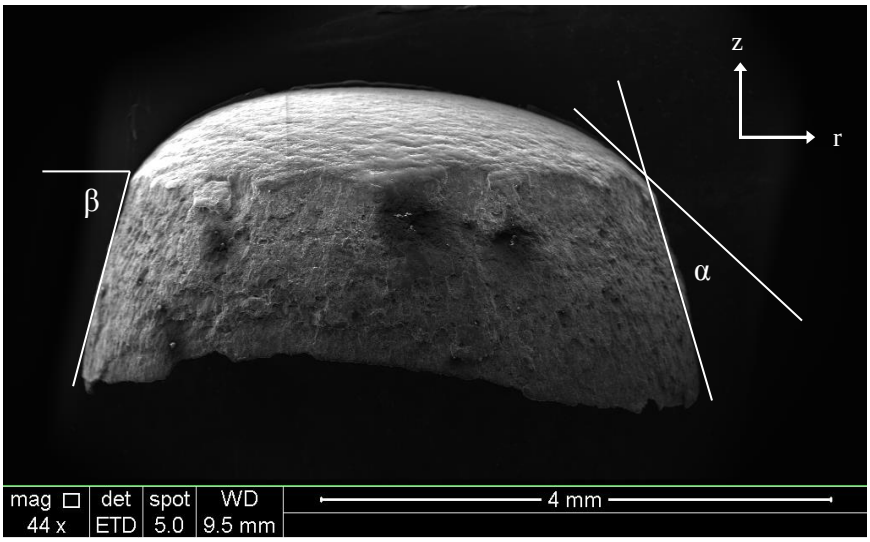

(b) SEM Image of Plug 5 Surface

Figure 4.9: Microscope Images of Plug 5

The cross-section of the plug showed center-point thickness of 1.35 mm (compared to an initial plate thickness of 1.6 mm) and a maximum width of 5.05 mm. The fracture surface of the plug occurs at an average angle $\alpha = 34°$ and an angle β relative to the r-axis of

approximately 70°. The indentations on the bottom side of the plug show the real shape of the projectile nose, caused by the machining process. The outer fracture surface of the plug was inspected via SEM to look for signs of void growth, localized melting or recrystallization (in order to assess the possibility of thermal softening). The surface showed no signs of either, indicating normal plug development by the growth of a crack through the thickness of the target plate. The absence of any sign of excessive heating at this surface supports the conjecture by Gupta et al. (2006) that thin plates of this material—having high conductance and minimal thickness—show little temperature sensitivity and negligible thermal softening at low impact velocities.

The impact experiments performed, in summary, show several phenomena which must be adequately captured in any attempt to fully model a projectile/target interaction under the conditions given.

i. *Plugging*: Circumferential localization and fracture centered on the projectile tip leads to the separation of the target plate and the center plug, which is carried on by the projectile. The geometry of the plug depends strongly upon the shape of the projectile and the stress field induced by the interaction of the projectile with the target. A blunt projectile with sharp edges will induced very localized shear and associated plug failure, whereas a rounded projectile may produce more tearing and failure by tension at a higher triaxiality, similar to discing. Target thickness also strongly affects the development of the plug, with thicker plates favoring dominant shear plugging, especially for impact by blunt projectiles. Further discussion and analysis will be

limited to thin plates, as tested experimentally, capable of significant out of plane plastic deformation.

ii. *Plug/Projectile Separation*: At the completion of the plugging process, the plug is fully separated from the target plate and in contact with the front surface of the projectile. As the projectile slows due to continued interaction with the target, the free plug separates and advances ahead of the projectile tip under its own inertia. The rate of separation varies according to the deceleration of the projectile post plug formation. At one extreme, only minimal frictional forces may be acting upon the projectile generating a minimal change in momentum between plug and projectile. Under combined mechanisms of failure, a highly tapered projectile may experience significant deceleration after plug formation, even failing to perforate the target completely. Separation of the plug from the projectile in a model response reflects the true detachment of the plug from the plate and its continued movement under only inertia. Post-mortem analysis of a recovered plug offers several geometrical metrics that are easy to quantify with which to compare a model result, capturing elements of both the plastic behavior and failure behavior of the specimen.

iii. *Petalling*: The development of the plug leaves a free surface under hoop tension on the target plate. Localization under this hoop tension leads to the development of radial cracks in the target plate. Propagation of these radial cracks, driven by continued penetration of the projectile, leads to petals which are bent out of plane by

the projectile, allowing perforation of the target plate. Upon full perforation by a projectile, developed petals (limited to thin plates as discussed) curve beyond perpendicular to the target plane, appearing to bend back over the base of the petal. Experimental results show that the number of petals developed varies with the velocity of the projectile at impact. The number of petals, in this way, depends upon the strain rate experienced by the target during the process of perforation. It is believed that the mechanism of this strain-rate "dependence" is much the same as that described in Chapter 2, for the case of uniaxial tension in expanding rings. While the stress state is more complicated at the newly created plugging surface, the same Mott-like mechanism of localization and propagation of the associated stress-release wave are fully capable of generating the observed dependence of petal number on impact velocity. At the plugging surface prior to radial crack formation, the dominant hoop stress in the plate gives a close qualitative analog to the expanding ring test in which the mechanism of inertia-driven, dynamic multiple localization and failure, independent of any material strain-rate dependence, was evidently supported.

iv. *Slant Fracture*: In the targets used, the fracture surfaces generated by the radial cracks forming petals display clear slant fracture character from plugging surface to petal base. In order to generate this behavior, through-the-thickness necking and localization behavior must occur. It was anticipated that this behavior may be very difficult to model under impact conditions using the methods available.

4.3 Simulations and Numerical Results

A fully successful attempt to model ballistic impact with respect to the target-projectile system and conditions described previously must generate the full complement of deformation and failure mechanisms observed experimentally. In addition to this, a fully accurate model must closely approximate the quantitative results of the experiment such as final target geometry and projectile velocity change. Historically, model accuracy has frequently been ensured by the tailoring of possibly several unconstrained model parameters (by means of a best fit procedure) to experiment results directly. While potential model capability can be demonstrated by means of this procedure, the predictive capability of any model is immediately compromised when formulated in this manner. The intention of this modeling effort is to assess the capability of a fundamentally simple material and failure model to capture the behavior of a projectile-target system under ballistic impact. Both the material and failure models utilized can be calibrated using reasonably simple laboratory tests, preserving an element of practical use-ability with respect to engineering analysis and design. It is recognized that the simple models utilized may not represent the material response accurately over all domains and material conditions experienced during ballistic impacts. The nature of the problem is such that extreme regimes of material response are interrogated. Large plastic strains, high strain rates, extreme localized deformation and the possibility of complicated temperature effects potentially create a large amount of uncertainty and inaccuracy in the modeling

process. The complicated nature of ballistic impact and perforation in particular provides a powerful crucible with which to evaluate these material models.

In order to model the experiments detailed in the previous section, a series of dynamic finite element simulations were performed using ABAQUS Explicit. The experimental conditions were simulated initially using an axisymmetric model to evaluate the axisymmetric deformation (e.g. dishing) and plugging mechanisms observed in experimental results. Further evolution of the perforation process, with the exception of the blunt nose projectile (which is not analyzed further due to the large volume of work regarding this projectile-target configuration), becomes non-axisymmetric due to circumferential localization at the plug surface and subsequent radial cracking. Quarter-plate symmetric models were then evaluated to observe the aforementioned localization and petalling mechanisms. Both of these attempts were successful in capturing the fundamental behavior being investigated, but the implementation of symmetry in the models represented a fundamental disconnect from the real configuration and observed behavior. For these reasons only the results of complete geometry, full plate simulation are discussed from here on out, recognizing that the full plate model fundamentally contains all of the elements investigated in prior attempts.

The full target plate was modeled using a 6” diameter circular model plate with a rigidly clamped boundary condition along the outer circumferential surface, representing the interior deformable region of the target plate clamped on the outer boundary by the target fixture (see Fig. 4.1). The model plate (see Fig.4.10) was meshed using 3,377,022 3D linear tetrahedral elements (C3D4) with a minimum element size of 50 μm at the

center of the plate and a maximum size of 5mm at the periphery. While the tetrahedral element allows the number of elements used through the thickness to be varied by radial location, at the center the minimum element size gives 32 elements through the plate thickness.

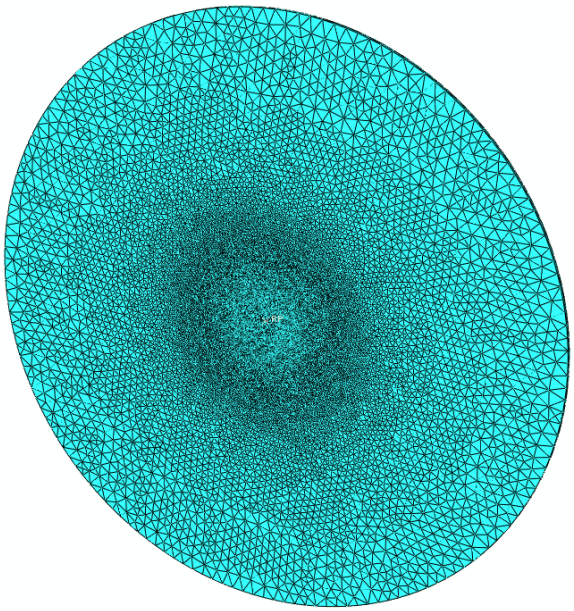

Figure 4.10: Target Plate Mesh

The partitioning and seeding of the mesh was controlled such as to generated maximally fine mesh only in the very central region in which the primary structural failure mechanisms are observed. The grain scale mesh size in the regions of failure is chosen to reflect the gage lengths over which the failure model developed in Chapter 3 was measured. While material failure as implemented in dynamic finite element simulations is often based upon global measurements of specimen strain at failure, such

models are appropriate to larger size elements representing the larger gage lengths over which failure strain is measured. As discussed previously, the substantial increase seen in material strain to failure when measured at gage lengths approaching the grain size dictates the use of more realistic gage lengths over which failure occurs in the model. While ductile material failure occurs on even smaller length scales, the use of continuum mechanics is limited by the size of some representative volume over which continuum isotropy can be considered valid. When implementing both continuum level deformation mechanics and material failure by means of element deletion, some amount of compromise must be made. The implementation of elements on the order of grain scale offers a potentially desirable compromise between the justifiable use of continuum mechanics and the implementation of continuum strain-to-failure models over a more realistic local gage length. While meshing at this scale pushes the justifiable limits of continuum mechanical formulations, it does afford mesh resolution sufficient to capture more intricate failure patterns than possible (while using element deletion) at coarser mesh scale. For these reasons, element size in the region of interest was chosen as to approach the grain scale in the candidate material. Tetrahedral elements were chosen in order to better control the number of elements through the thickness at different locations in the model plate and to ensure a more realistic, unstructured mesh in the region of interest. The projectile (see Fig. 4.3) was modeled as a discrete rigid body using approximately 14,800 total rigid 3D quadrilateral and triangular elements (R3D4, R3D3). A summary of mesh and elastic material properties is given in Table 4.2.

Table 4.2: Model and Mesh Properties and Parameters

	SI (mm/MPa)	Reference Unit
t	1.6 mm	.063”
D	152.4 mm	6”
ρ	2.66E-9 tonne/mm^3	2.66 g/cm^3
E	69,900 MPa	10,130 ksi
ν	0.33	

Target Mesh	
3,377,022 linear tetrahedrons	C3D4, free meshing
Min. element size	50 µm
Max. element size	5 mm
Max # elements through thickness	32

Standard isotropic J_2 plasticity was implemented in the model using the determined Ramberg-Osgood material fit (see Fig. 1.7) extrapolated to a strain level of 3. Johnson-Cook damage initiation was also incorporated in the model using the failure curve given in Fig. 3.15. Note that the Johnson-Cook damage as implemented in ABAQUS initiates material damage according to Eq. 3.1. Specification of a means of damage evolution beyond initiation is required to generate material damage in the traditional sense, where material performance is degraded with increasing damage accumulation. In this case, instantaneous damage was implemented such that an element would reach maximum degradation and be removed from the mesh upon reaching strain-

to-failure as indicated by the Johnson-Cook damage initiation criterion. As implemented in ABAQUS in this manner, material damage itself is non-cumulative but damage initiation is cumulative such that loading path influences the point of initiation of damage but material performance is not affected until the point of failure and element removal. While the results of Chapter 3 indicate that damage initiation should not be modeled cumulatively either, there is not a readily available way to model non-linear or non-cumulative damage initiation in ABAQUS. Table 4.3 gives both the R-O fit parameters utilized in the modeling of the material plastic response and the damage initiation parameters as seen in Eq. 3.1 and implemented in the ABAQUS Johnson-Cook damage model. For reference, the effective material response and strain-to-failure behavior given by these parameters and implemented in the model are shown in Fig. 4.11.

Table 4.3 – Material Model ABAQUS Parameters

R-O parameters	
α	0.912
n	6.49
σ0	203 Mpa
J-C Failure Criterion	
D1	0.3
D2	1.4
D3	-1.4
D4	0
D5	0

As described and developed in previous chapters, both the plasticity model and damage model utilized specify no strain rate or temperature dependence, rendering the

plastic response effectively identical to power-law hardening and strain-to-failure curve dependent only upon triaxiality.

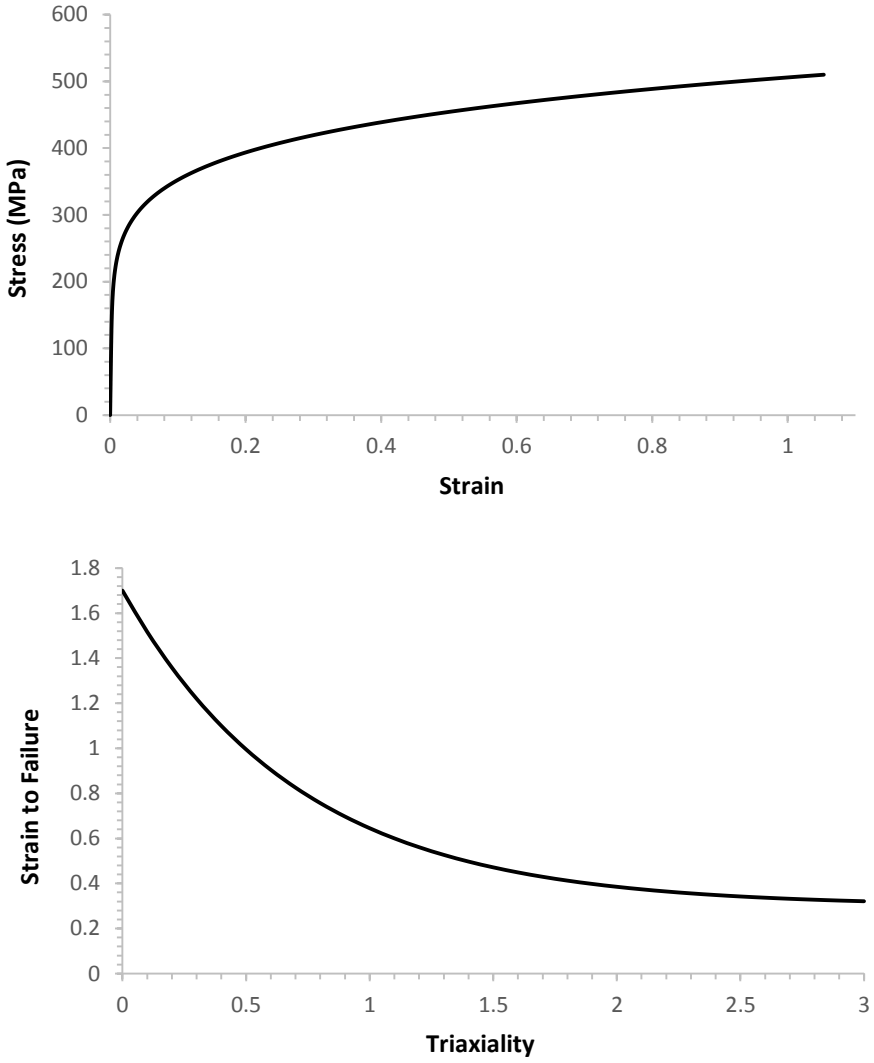

Figure 4.11: Computational Material and Failure Model

The material strain-rate dependence was directly evaluated in Chapter 2, but material temperature dependence was not experimentally assessed in this work. While

thermal softening is indeed present in materials of this type at sufficiently high temperatures, the low-velocity impacts evaluated in this work are unable to generate sufficient heating by means of plastic work to induce appreciable softening or temperature dependence. As investigated by Gupta et al. (2006), the relatively low speed, of the impact, relatively large distribution of plastic deformation (again limited to low speed impact events in thin targets), and high thermal conductivity of the material prevents significant temperature change during the perforation. The long time scale over which penetration and perforation occur (with respect to ballistic regimes) and the high thermal conductance of the aluminum alloy prevent significant localized heating as is observed in the extreme case of catastrophic adiabatic thermoplastic shear (Recht 1964) seen in some materials during high velocity blunt impact. For these reasons, temperature dependence is ignored for this analysis. However, under more violent loading temperature effects may become significant and for the purposes of fully general analysis, would need to be evaluated and incorporated appropriately.

The rigid projectile was assigned a lumped inertia and given initial impact velocity by means of a predefined velocity field applied to the body. In order to most closely interrogate the violation of axisymmetry by means of only material localization and not geometrical asymmetry, the motion of the projectile was constrained to translation along the axis of the target/plate system (z-axis). In addition, rough contact was defined at the nose of the projectile, preventing slippage between the target and projectile nose surfaces during penetration. Due to the small minimum element size, the stable explicit time step increment as estimated by ABAQUS is very small—on the order

of nanoseconds. The large overall size of the model combined with this small time increment make for a very long and intensive simulation. Simulation were performed on a Xeon processor with 8 cores and took over 3 weeks (wall-clock time) to complete. For this reason, only simulations at impact velocities of 150 m/s and 75m/s were attempted. Technical issues were encountered over the course of multiple attempts of the 75 m/s simulation, preventing its completion within the available time frame. Completed simulation results for the 75 m/s second model are presented, but the remaining analysis will focus primarily upon the 150 m/s case.

Figure 4.12 shows a large field view of the 150 m/s impact simulation at the point of effective perforation. In this case, effective perforation is considered achieved when the contact patch between the target plate and projectile reaches beyond the shoulder of the tapered projectile, at which point only incidental frictional contact acts upon the projectile and no further radial expansion of the perforation hole is necessary to permit full passage of the projectile.

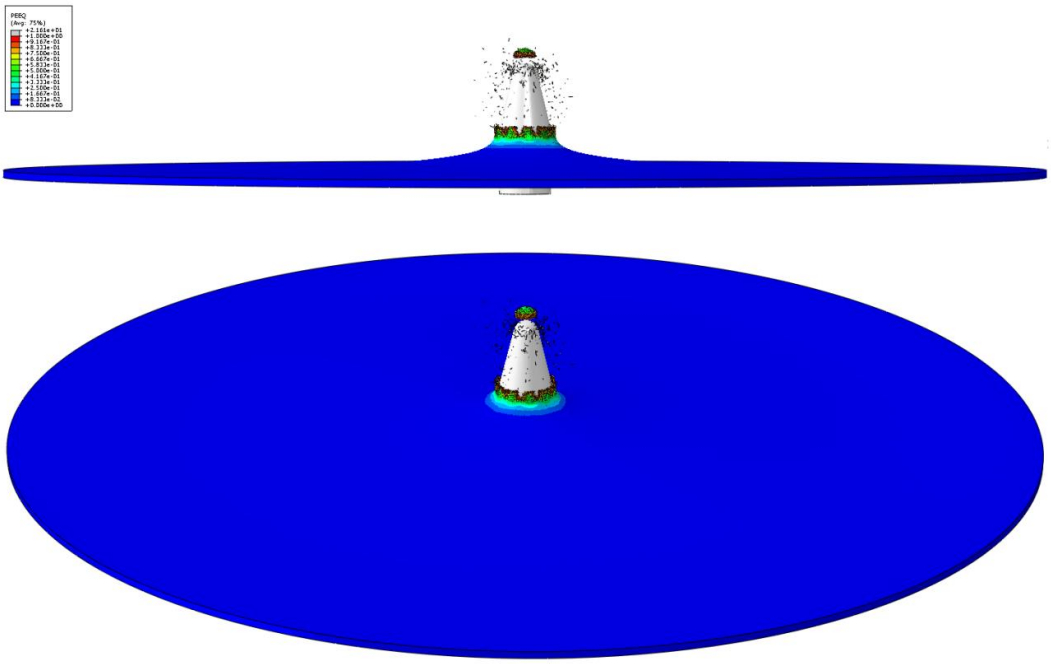

Figure 4.12: Full-field Simulation Result – 150 m/s Initial Velocity

Very little significant deformation occurs outside of the very center of the plate. Around the area of perforation, however, significant out of plane deformation by means of dishing can be observed. Focusing upon this central area, several mechanisms are apparent. Figure 4.13 shows the simulated perforation process in the center region. Note, two series of images are presented at corresponding simulation times. The A series of images gives a section view at the center plane of the target/projectile system, while the B series presents the full view of the outer surface of the plate viewed side-on.

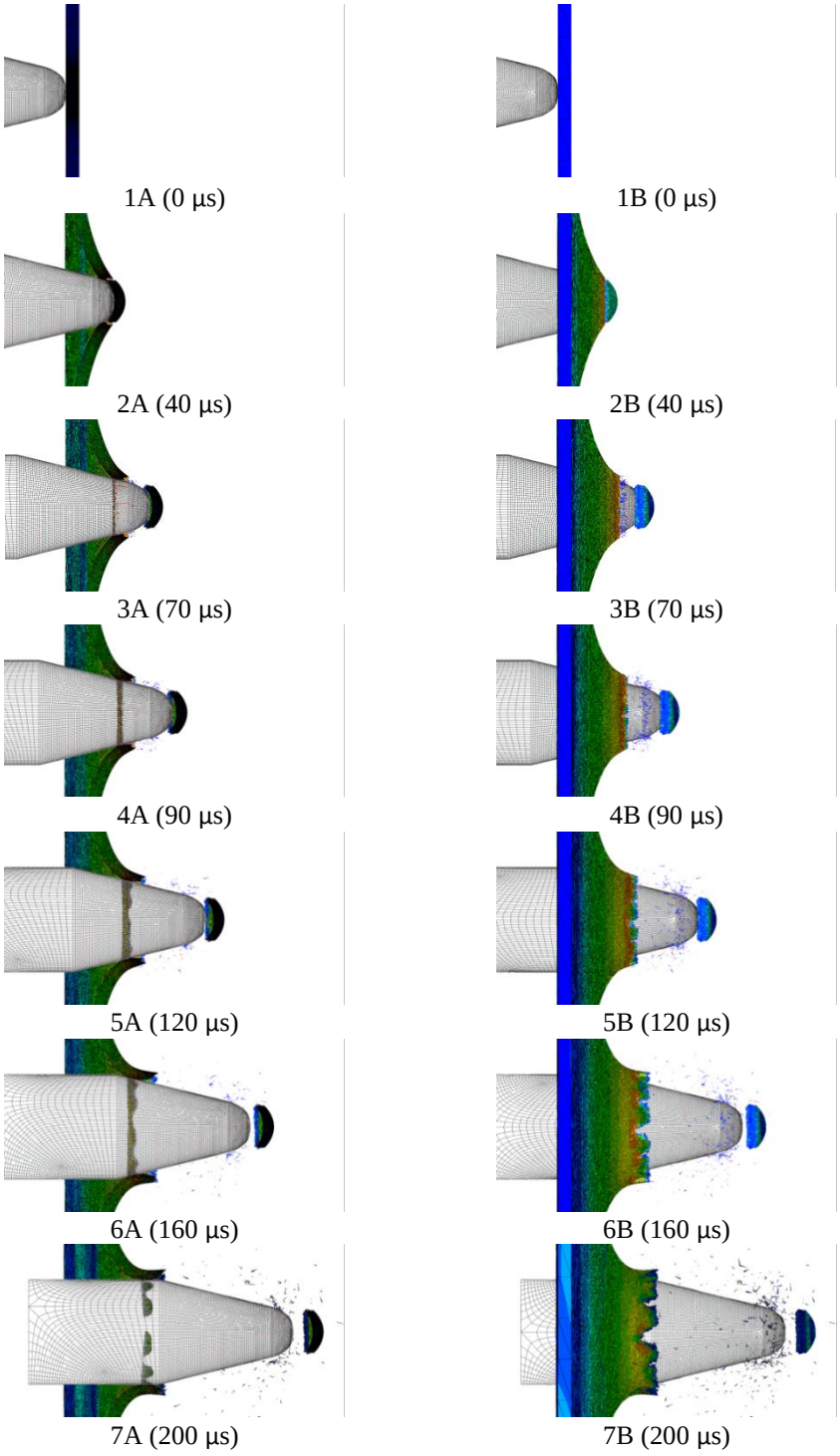

Figure 4.13: Simulation Results – 150 m/s Initial Velocity

After initial plastic deformation of the target plate, plugging occurs at approximately 40 μs in 2A/2B. The continuing perforation of the plate sees the expansion of the hole axisymmetrically for a short time until the nucleation of radial cracks occurs around 70 μs. The beginnings of radial cracks are seen in 3A/3B. Further progress by the tapered projectile drives the propagation of radial cracks, generating the fully formed petals observed upon the completion of effective perforation in 6A/6B. The A series of images (Fig. 4.13) also allows the observation of the contact patch between the projectile and target. The shape of the contact patch reveals the radial localization that breaks the axisymmetry of the event and the growth of petals as a function of perforation. Interestingly, 6A shows the remaining contact surface to be discontinuous, requiring the growth of petal cracks beyond the point of structural contact at the completion of effective perforation. Notably, plug separation is visible throughout the simulation, and while erosion at the tips of the simulated petals seems to remove some material and length from the petals themselves, back-bending of the final petal structure is visible in the model result.

A closer examination of the plugging process in the 75 m/s simulation is shown in Fig. 4.14. These images show a meridional slice near the region of impact. The nucleation of the plugging crack on the back surface of the target plate at an equivalent strain level of approximately 0.7 can be seen at 80 μs. The circumferential plug crack propagates towards the projectile, fully separating the plug from the target plate by 118 μs. The stress field generated by the projectile nose shape in conjunction with the target

deformation determines the angle of the plug surface with respect to the initial target plane.

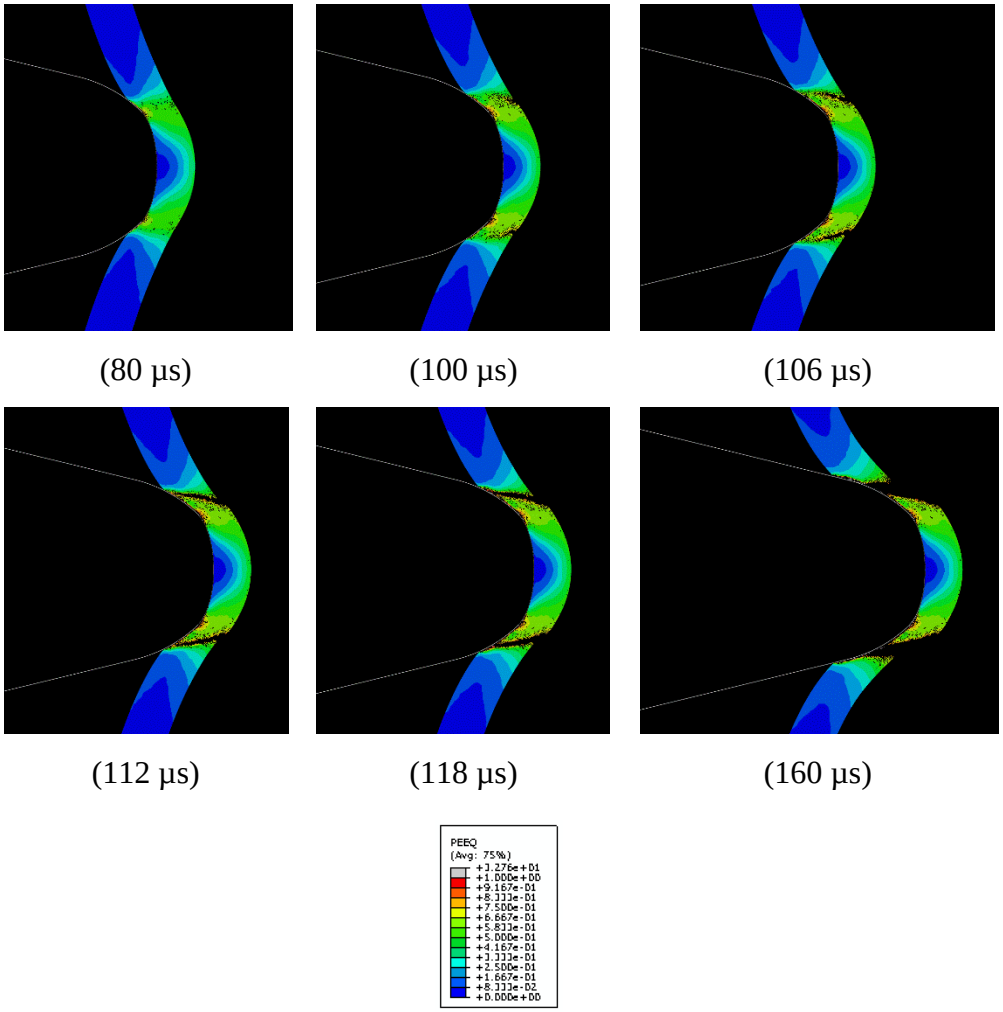

Figure 4.14: Plugging Process – 75 m/s Initial Velocity

Thin sections such as these will experience sufficient dishing, even with blunt nose projectiles, to generate a non-orthogonal plug surface angle. In contrast, a thick target may generate a truly cylindrical plug when impacted by a blunt nose projectile. Whereas the plug generated by the 75 m/s impact shows a distinct surface angle across the entire fracture surface, the 150 m/s plug shows tearing at the inner surface of the plug fracture surface (see Fig. 4.15).

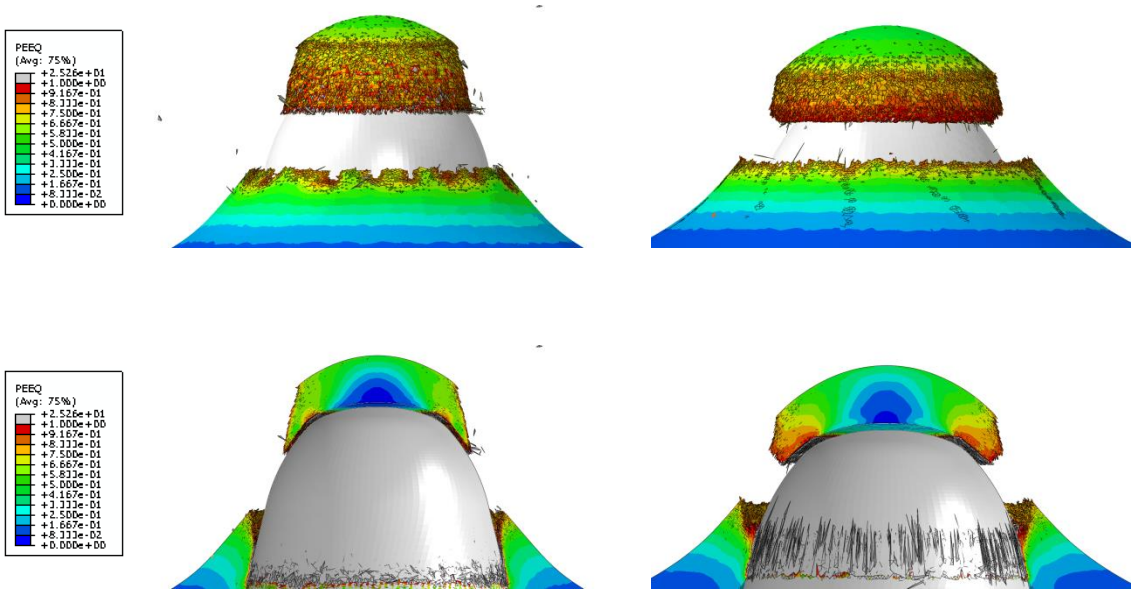

75 m/s 150 m/s

Figure 4.15: Plugs at 150 m/s and 75 m/s

As the plugging crack extends, the effective thickness of the plug with respect to the inner surface of the target plate decreases significantly, tapering to a point as seen in the 75 m/s plug (Fig. 4.15). However, at 150 m/s the plugging crack “turns a corner” and

completes the plug separation by means of a mode more indicative of tensile tearing. This behavior was not observed in the experimental results; however, it is possible that its presence in the model result is due to inaccuracies in the material model or local projectile geometry. Further experimentation in this study should attempt higher velocity experiments to evaluate whether this effect is real or a consequence of the finite element model. On a side note, the very beginnings of radial cracking can be seen on the surface of the plate for the 150 m/s result (Fig. 4.15). The maximum diameter and thickness of the plug are compared to experimental values in Table 4.4.

Table 4.4: Plug Geometry Measurements

Central Plug Thickness (mm)	Experimental	Simulation
75 m/s	NA	1.28
150 m/s	1.35	1.33
Plug Diameter (mm)		
75 m/s	4.7	5.0
150 m/s	5.1	5.4

While the model predicts an absolute plug diameter slightly larger than seen experimentally, both experiment and simulation shows a very comparable change in plug diameter across the range of velocity. Likewise, simulation predicts an increase in center plug thickness with increasing velocity, a trend observed by previous works (Goldsmith and Finnegan, 1971). Note, the increase in plug thickness is expected as maximum plate deformation and dishing is expected near the ballistic limit, thinning the central region of the plate prior to plugging.

The next phase of perforation is dominated by the pettaling process. Figure 4.16 shows the development of petals in the 75 m/s simulation.

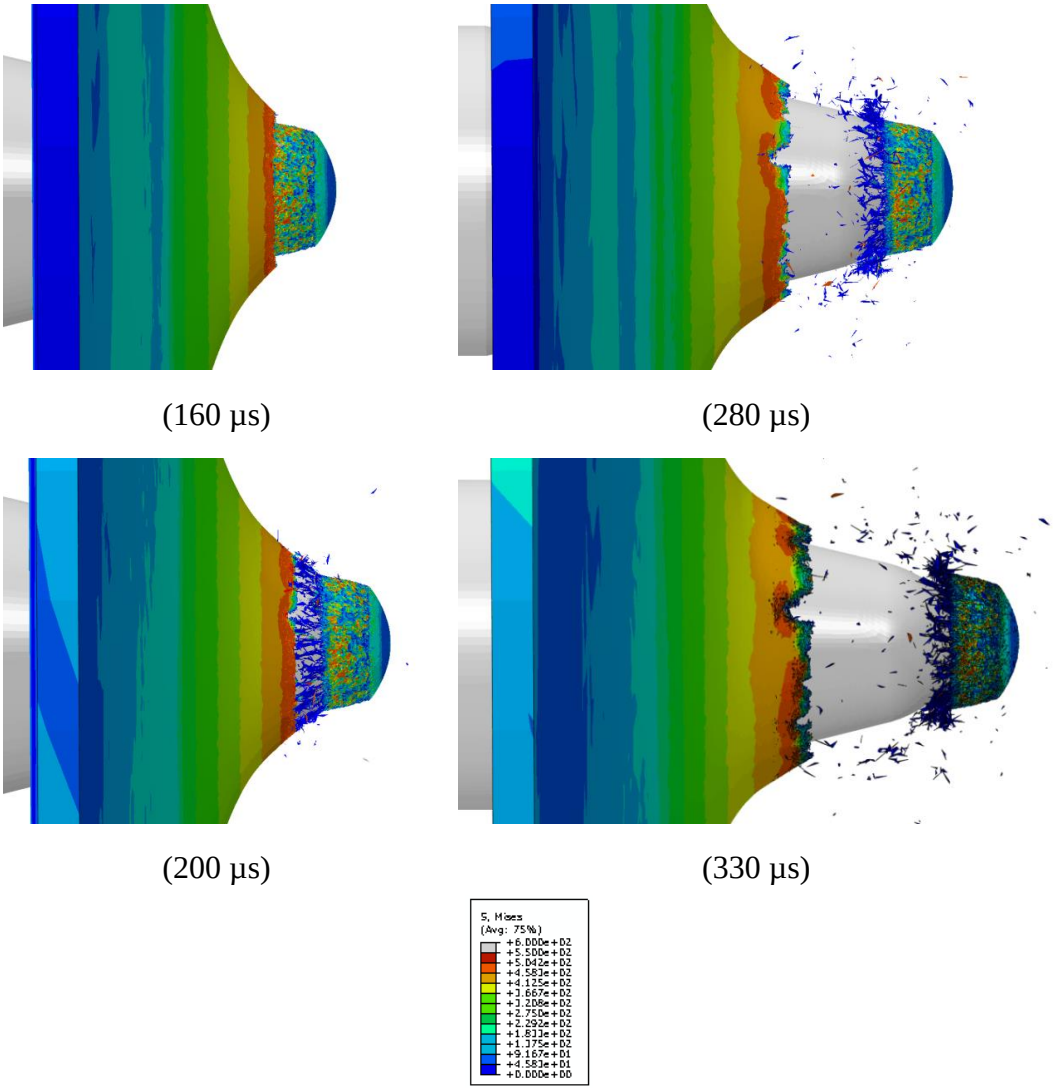

Figure 4.16: Development of Petals in 75 m/s Simulation

After the separation of the plug, the effective stress is more or less axisymmetric around the newly created fracture surface (160 μs). The highest hoop tension is seen at the edge of the hole, eventually localizing in the hoop direction and nucleating radial cracks at the outer plate surface of the hole edge. As these radial cracks grow, the petal material in between radial cracks is unloaded in the hoop direction (280 μs). The highest stress is concentrated at the tip of the radial cracks and the associated base of the bending petal. As the contact patch between the projectile and petal begins to move backwards, the petal tip is fully unloaded (330 μs).

Both the experimental results and our expectations of dynamic petalling as an analogous process to the Mott style fragmentation (developed in Chapter 2) predict the number of radial localizations and cracks to be dependent upon the strain rate--and ultimately the impact velocity--experienced by the material under dominant hoop tension at the edge of the plug hole. In order to observe the resulting petals clearly, Fig. 4.17 shows a section view parallel to the target plane, cutting through the developed petals. Note, the direction of view is in the direction of projectile motion, but both the projectile and the majority of the target plate have been removed from view in order to clearly observe a plane where well developed petals are easily discerned. The back (concave) side of the plug is visible in the center of the images.

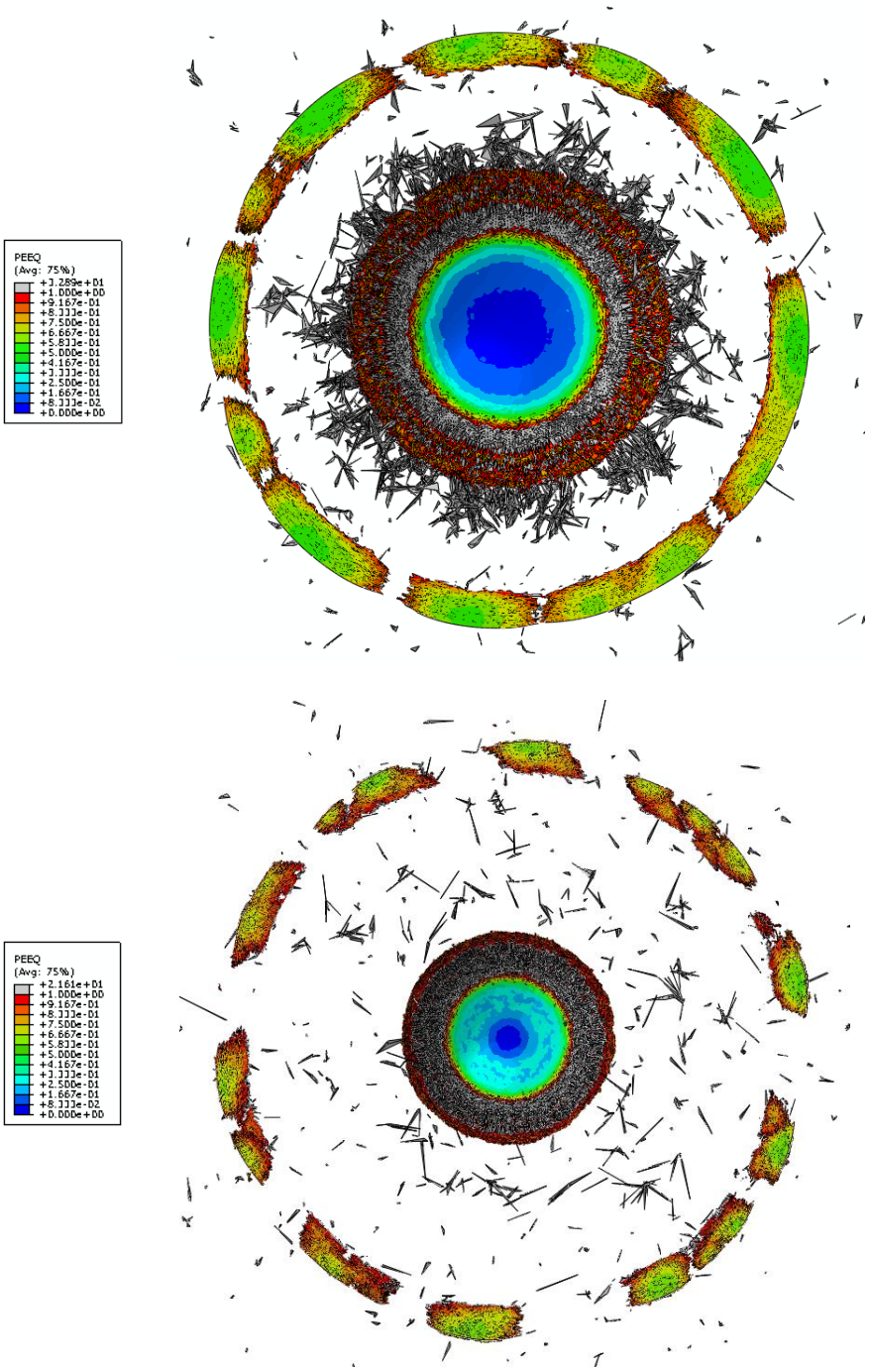

Figure 4.17: View Cut of Petal Structure at 330 μs (75 m/s) and 200 μs (150 m/s)

While the model result generally over-predicts the number petals, a measurable increase in the number of developed petals is seen across the velocity range, as observed in experiment. Some deviation from experiment is expected in this case as the mechanism of element deletion provides a very coarse approximation of failure. However, the successfully modeled proportional variation of petals with impact velocity gives strong support to the assertion that the localization and fracture leading to the development of petals is fundamentally dynamic, and is governed by the same inertial principles present in Mott fragmentation (see Chapter 2). The combined effect of structural processes as these and material response ultimately determine the resistance of the target plate to perforation by a kinetic impactor.

The velocity of the projectiles as a function of time is given in Fig. 4.18. The 150 m/s and 75 m/s curves display a kink at approximately 40 μs and 100 μs respectively, corresponding to the plugging process seen in Fig. 4.13. At 190 μs the 150 m/s projectile completes perforation. Note, the 75 m/s simulation was terminated at 330 μs prior to full perforation.

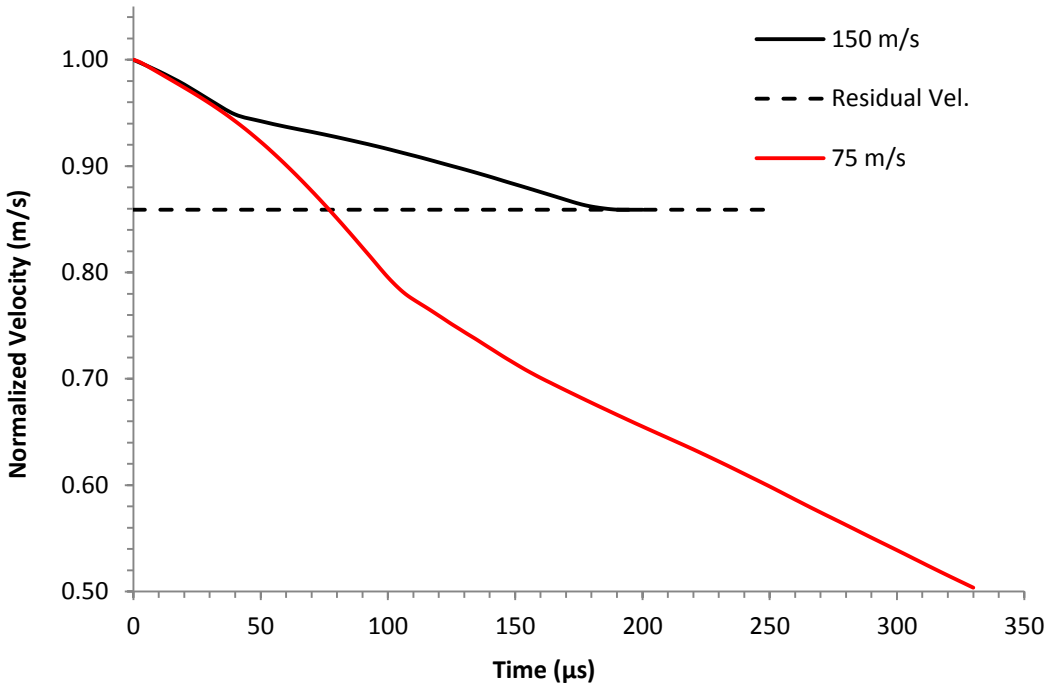

Figure 4.18: Normalized Projectile Velocity

Prior to plugging, plastic plate deformation is responsible for the deceleration of the projectile. After plugging, failure processes dominate the resistance of the plate to perforation. Occurring over smaller volumes of material, localized failure processes such as plugging will likely absorb less energy than global deformation mechanisms in total, leading to an overall decrease in the resistance of a target to penetration or perforation. An extreme case is the blunt nose impact experienced by Plate 4 (see Fig. 4.6), where the residual velocity indicates much reduced energy expenditure by the perforation process. Specifically, because plugging in the blunt case opens a hole the same size as the projectile diameter, no significant resistance is experienced subsequent to plug removal limiting target energy absorption to that achieved by relatively limited plastic

deformation and extremely localized shear failure. Upon completion of effective perforation, the projectile velocity plateaus, giving the residual velocity of the projectile as predicted by the simulation. Here, the model falls significantly short, predicting a residual velocity of 129 m/s for the 150 m/s impact, well below the nearest comparable experimental value. The significantly elevated change in velocity seen in the simulation indicates excessive energy consumption by the perforation process. There are several possible sources for this discrepancy which may be effectively working in conjunction. Likely candidates are inaccuracies in the material plastic response and strain-to-failure model. Excessive hardening at large strains may contribute to the increased model stiffness. Additionally, the increased strain-to-failure measured at the length scales described may demand excessive plastic work for failure when implemented by means of element deletion across element sized volumes. Further evaluation of the total material model and its effects upon the numerical model when implemented as described must be undertaken in order to answer this discrepancy and generate a fully successful model. However, at this stage the primary goal of the simulation is to generate the entire host of deformation and failure mechanisms observed experimentally, rather than necessarily reproducing a quantitative value. Unknowns in the material model may generate the significant discrepancy seen in residual velocity, but in order to potentially solve this problem by means of more accurate material representation, the fundamental physics of the experiment must be present in the model. Successful simulation and presence of multiple mechanisms such as plugging and petalling indicate that the model is capable of achieving fundamental accuracy.

For more general comparison to experimental result, the final deformed model is given along with experimental post-mortem images of the relevant target plate in Fig. 4.19. The sectioned and imaged plug (150 m/s) is also compared with the simulation in Fig. 4.20.

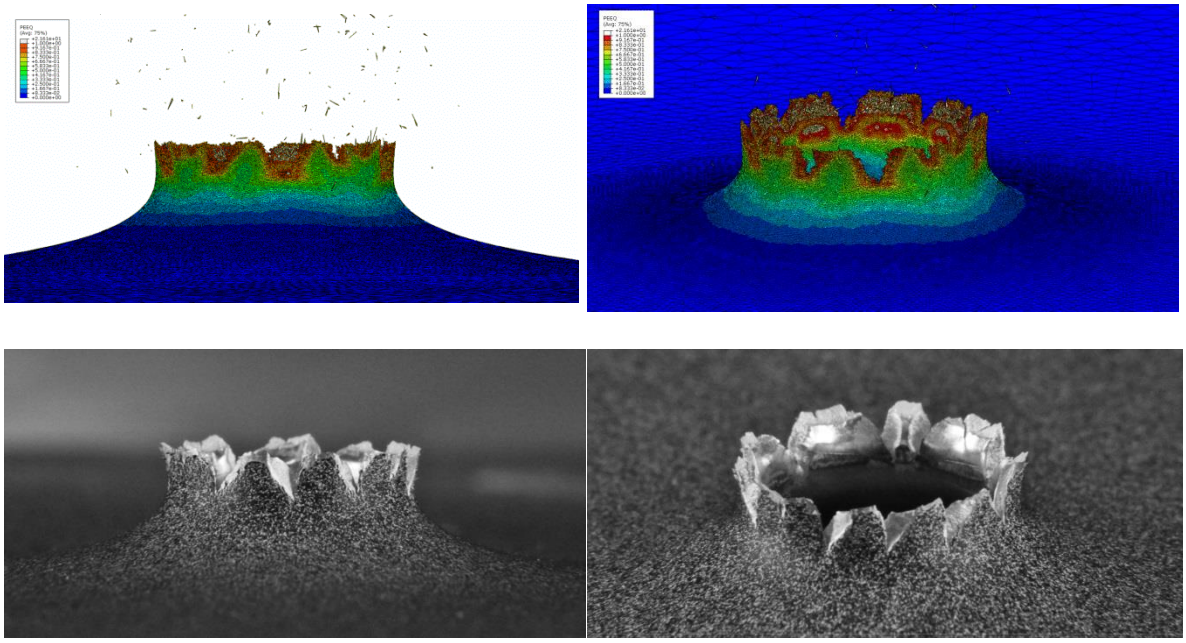

Figure 4.20: Post-Mortem Comparison of Perforations (150 m/s)

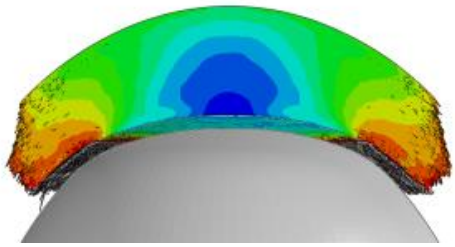

150 m/s Section

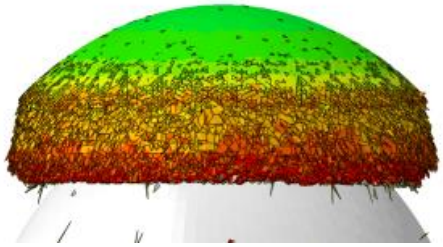

150 m/s Surface

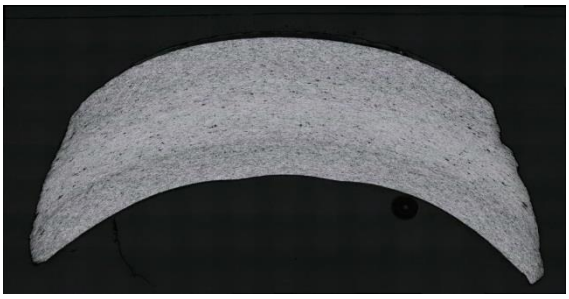

Plug 5 Section

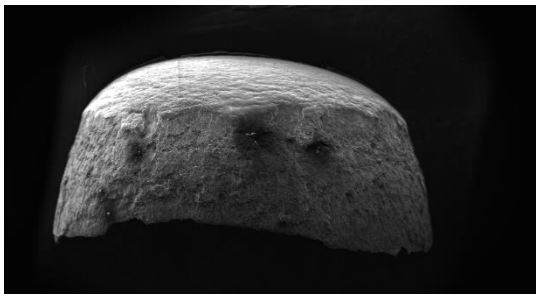

Plug 5 Surface

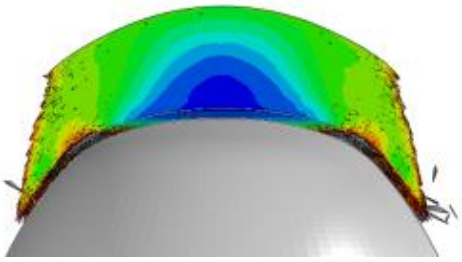

75 m/s Section

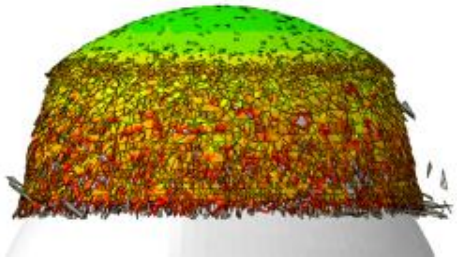

75 m/s Surface

Figure 4.20: Post-Mortem of Simulation Plugs with Plug 5

Notably absent from the simulated result is the slant fracture observed in the petal fracture surfaces. While distinct slant fracture character can be seen in the post-mortem images from point of initiation (petal tip) to termination (petal base), definitive slant fracture was not observed in the simulation result, where the petal fracture surfaces

indicated normal tensile tearing. While slant localization and fracture has been successfully modeled using similar material models previously in uniaxial tensile simulations, it is believed that in this case that the mesh and model scale utilized was simply incapable of capturing the proper strain localization necessary to display this behavior. It is believed that even finer scale is likely necessary to generate sufficient mesh resolution through the thickness of the plate to observe slant behavior in the stock material and geometry considered here. The inability to capture this behavior is a significant failure of the given modeling attempt as slant fracture falls into the category of fundamental physical phenomena necessary to fully capture the behavior of the target/projectile system in full.

While not all the relevant behavior was captured in the attempted model, a number of fundamental phenomena were successfully generated to a level comparable to that of the experimental result. The primary failure mechanisms of plugging and petalling were captured and the important velocity dependent trends relating to these mechanisms were observed. Inaccuracy in the material model could relatively easily influence the absolute discrepancies seen in plug geometry and petal number. Physical phenomena such as plug-projectile separation were observed, ensuring proper interaction between contact surfaces and successful failure based modeling of the complete removal of the plug from the target plate. While the overall kinetic energy retention of the projectile saw significant discrepancy with experiment, a realistic and logical variation in velocity as perforation occurs was observed via simulation. Again, inaccuracy in the material or failure model may be responsible for the excessive resistance of the model target. Lastly,

the model was incapable of capturing the slant fracture characteristic observed in experiment. Modification of the model to capture this behavior may very well be necessary to accurately predict residual velocity and ballistic limit of this projectile/target system without unjustifiable “a posteriori” modification of the material model in order to fit experimental results. Such tailored manipulation would of course compromise the usefulness of the modeling approach in general. Despite these failures, the successful modeling of these fundamental mechanisms of ballistic perforation utilizing only a very simple material representation and more realistically calibrated empirical failure model represents a valuable step in achieving comprehensive modeling success and potential predictive capability with respect to ballistic impacts of this type in general.

Chapter 5: Conclusions and Recommendations

This intent and objective of this work were to evaluate the capability of simple material and failure models, when implemented in numerical finite element simulation, to capture the potentially complex deformation and failure behavior involved in the ballistic perforation of metallic targets. While perforation under the conditions investigated is inherently complicated, potentially involving the competition and cooperation of several mechanisms of material and structural failure, several phenomena fundamental to this process were successfully simulated using only standard Mises plasticity and a Johnson-Cook style strain-to-failure model. The strain-to-failure model implemented was previously calibrated using grain-scale inspection of failure strains, much more closely approximating the length scales over which material failure actually takes place. In accordance with these measurements, a very fine simulation mesh was utilized, providing near grain-sized elements in the regions in which perforation failure mechanisms occur. This grain based implementation of Johnson-Cook strain-to-failure by means of element deletion attempted to tie this common method of ductile failure modeling to a physical material scale and to push the limits of conventional continuum-based finite element modeling as applied to ductile failure.

In order to calibrate the necessary Ramberg-Osgood material curve and Johnson-Cook style triaxiality based strain-to-failure locus a series of experiments were performed investigating multiple aspects of the candidate material's (AA5083-H116) material and failure behavior. Quasi-static tensile test were performed in order to calibrate the material elastic and plastic response as well as investigate the Portevin-Le Chatelier effect common to this series of alloys. The strain rate dependence of the material was charaterized using a series of electromagnetically driven expanding ring tests, probing the

material strain sensitivity at strain rates exceeding 10^4 s^{-1}. Additionally, the failure and damage behavior of the material of investigated using a series of shear and notched tension test. The accumulation of damage in the material was investigated by means of multiple load path tests. The strain-to-failure of the material (as measured in notched tension tests) was shown to be insensitive to prior strain history generated under shear loading, indicating the absence of damage accumulation at low triaxiality and justifying the neglect of material degradation prior to failure and element deletion in simulation.

Simulation of ballistic impact and perforation utilizing the developed material and failure properties successfully captured several fundamental phenomena observed in the experimental ballistic tests—such as plugging and petalling failure—but failed to capture the slant fracture character associated with the radial petal cracks and the substantially over-estimated the ballistic resistance (and therefore the ballistic velocity limit) of the target/projectile system. Further experimental and modeling efforts should attempt to address these failures by several means. At the low velocities tested, an appreciably volume of material undergoes substantial plastic strain; inaccuracies in the material plastic behavior at large strains may contributed substantially to the excessive stiffness of the model. A deeper investigation of the material response and hardening characteristics at high levels of strain should be performed to investigate this potential error, keeping in mind that a primary goal of this work is to utilize the simplest material model and testing regime necessary. Additionally, the inability of the model to capture the slant fracture behavior observed in experiment is a potentially major failure of this technique. While finite element simulation at this scale may be largely unable to practically capture this phenomena, further modeling investigation is necessary to evaluate the overall model error generated by the absence of slant fracture from the simulation. The absence of slant fracture in favor of the tensile tearing failure observed in the model may explain a

significant fraction of the excessive ballistic energy consumed. Extra plastic deformation associated with the model petalling fracture over the actual slant fracture may account for the elevated model ballistic resistance during perforation. Successful capture of this behavior within the simulation of ballistic perforation would render the model fundamentally complete, leaving any existing errors attributable to material calibration or the nature of the finite element model itself.

Bibliography

Alcoa Defense (2010). Advantages of Aluminum in Marine Applications. https://www.alcoa.com/global/en/news/webinar/al_shipbuilding/Alcoa_defense_and_abs_webinar.pdf

ASTM B209 (2014). Standard Specification for Aluminum and Aluminum-Alloy Sheet and Plate.

ASTM B928 (2014). Standard Specification for High Magnesium Aluminum-Alloy Sheet and Plate for Marine Service and Similar Environments.

Backman, M. and Goldsmith, W. (1978). The Mechanics of Penetration of Projectiles and Targets, *Int. J. Engr. Sci*. (16): 1-99.

Bao Y., Wierzbicki T. (2004). On fracture locus in the equivalent strain and stress triaxiality space, *Int. J. Mech. Sci*.(46): 81–98.

Bethe, H.A. (1941). Attempt of a Theory of Armor Penetration. *Ordnance Laboratory, Frankford Arsenal.*

Børvik, T., Forrestal, M.J. , Hopperstad, O.S., Warren, T.L. and Langseth, M. (2009). Perforation of AA5083-H116 aluminum plates with conical-nose steel projectiles—calculations, *Int. J. Impact. Engng.* (36): 367-384.

Børvik, T., Hopperstad, O.S., Berstad, T., and Langseth, M.(2001). A computational model of viscoplasticity and ductile damage for impact and penetration, *Eur. J. Mech. Solids*. (20): 685-712.

Børvik, T., Hopperstad, O.S., Berstad, T., and Langseth, M. (2004). Perforation of AA5083-H116 aluminum plates with conical-nose steel projectiles—experimental study. Int. J. Impact. Engng. (30):367-384

Bishop, R. F., Hill R. and Mott, N. F. (1945). The theory of indentation and hardness, *Proc. Roy. Soc.*, (57): 147-159.

Cassarotto, L., Dierke, H., Tutsch, R. and Neuhauser, N. (2009). On nucleation and propagation of PLC bands in an Al-3Mg alloy. *Material Science and Engineering A*, (527):132-140

Calder, C. A. and Goldsmith,W.(1971). Plastic Deformation and Perforation of Thin Plates Resulting from Projectile Impact, *Int. J. Solids Struct*.(7): 863-881.

Corbett, G.G., Reid, S.R., and Johnson, W.(1995). Impact Loading of Plates and Shells by Free-flying Projectiles: A Review, *Int. J. Impact Engr*. (18): 141-230.

Forrestal, M. J. and Luk, V. K. (1987). Penetration into semi-infinite reinforced concrete targets withspherical and ogival nose projectiles, *Int. J. Impact. Engng* .(6): 291-301.

Forrestal, M.J., Rosenberg, Z., Luk ,V.K. and Bless, S.J. (1987). Perforation of aluminium plates with conical-nosed rods, J. Appl. Mech. (54) :230–232.

GlobalSecurity.org (2012). M-113 Armored Personnel Carrier. http://www.globalsecurity.org/military/systems/ground/m113.htm

Goldsmith, W. and Finnegan, S.A. (1971). Penetration and Perforation Processes in Metal Targets at and Above Ballistic Limits, *Int. J. Mech. Sci.* (13): 843-866.

Goodier, J.N. (1965). On the mechanics of indentation and cratering in solid targets of strain hardening metals of hard and soft spheres, *Proceedings of the 7th Symposium on Hypervelocity Impact*.(3): 215–259.

Gourdin, W. (1989). Analysis and assessment of electromagnetic ring expansion as a high strain-rate test, *Journal of Applied Physics*.(65): 411-422.

Grady, D. and Benson, D. (1983). Fragmentation of metal rings by electromagnetic loading, *Experimental Mechanics*, (23): 393-400.

Gross, A. Ravi-Chandar, K. (2015). Toward the Predictive Modeling of Ductile Failure. *The University of Texas at Austin.*

Gupta, N.K., Iqbal, M.A. and Sekhon, G.S. (2006). Experimental and numerical studies on the behavior of thin aluminum plates subjected to impact by blunt and hemispherical-nosed projectiles, *Int. J. Impact. Engng*. (32): 1921-1944.

Gurson, A. (1977). Continuum theory of ductile rupture by void nucleation and growth: part I.—yield criteria and flow rules for porous ductile media. *J. Eng. Mater. Tech*.,(99): 2–15.

Hopkins, H. G.(1960). Dynamic expansion of spherical cavities in metals, *Progress in Solid Mechanics*, (1): 83-164.

Hopkinson, B. (1914). A method of measuring the pressure produced in the detonation of high explosives or by the impact of bullets, *Proceedings of the Royal Society of London, Series A.*

Johnson, G.R. and Cook, W.H.(1983). A constitutive model and data for metals subjected to large strains, high strain rates and high temperatures, *Proc. 7th Int. Symp. On Ballistics*: 541–547.

Johnson GR, Cook WH (1985) Fracture characteristics of three metals subject to various strains, strain rates, temperatures and pressures. *Int. J. Eng. Fract. Mech*., (21): 31–48.

Kolsky, H. (1949). An investigation on the mechanical properties of materials at very high rates of loading, *Proceedings of the Physical Society of London, Series B.*

Lee, Y. W. and Wierzbicki, T. (2005). Fracture prediction of thin plates under localized impulsive loading, *Int. J. Impact Engng*. (31): 1253-1308.

LeMaitre, J.(1996). A Course on Damage Mechanics, *Springer Berlin Heidelberg.*

Levy, N. and Goldsmith, W. (1984). Normal Impact and Perforation of Thin Plates by Hemispherically-tipped Projectiles, *Int. J. Impact Engng*.(2): 209-324.

McClintock, F.A. (1968) .A criterion for ductile fracture by the growth of holes. *J. Appl. Mech.* (35) :363–371.

Mott, N. (1947). Fragmentation of shell cases. *Proceedings of the Royal Society of London, Series A.*

Niordson, F. (1965). A unit for testing materials at high strain rates. *Experimental Mechanics*, 5(1):29-32.

Recht, R.F. and Ipson, T.W. (1963). Ballistic Perforation Dynamics, *J. Appl. Mech.* (30): 385-391.

Taylor, G.I. (1948). The formation and enlargement of a circular hole in a thin plastic sheet, *Quart. J. Mech. Appl. Math*. (1): 103-124.

Wilkins, M. L. (1978). Mechanics of Penetration and Perforation, *Int. J. Engng. Sci*. (16): 793-807.

Zhang, H., Liechti, K. M. and Ravi-Chandar, K. (2009). On the dynamics of necking and framentation-III. Effect of cladding with a polymer. *Int. J. of Fract*., (150): 3-36.

Zhang, H. and Ravi-Chandar, K. (2006). On the dynamics of necking and framentation-I. real-time and post-mortem observations in al 6061-O. *Int. J. of Fract*., (142): 183-217.

Zhang, H. and Ravi-Chandar, K. (2008). On the dynamics of necking and framentation-II. Effect of material properties, geometrical constraints and absolute size. *Int. J. of Fract*., (150): 3-36.